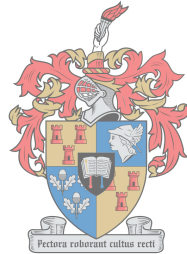


Design and Optimisation of Gap Waveguide Components through Space Mapping

by

Clifford Sibanda



UNIVERSITEIT
iYUNIVESITHI
STELLENBOSCH
UNIVERSITY

100
1918 - 2018

*Thesis presented in partial fulfilment of the requirements for
the degree of Master of Engineering (Electronic) in the
Faculty of Engineering at Stellenbosch University*

Supervisor: Prof. D. I. L. De Villiers

March 2018

Declaration

By submitting this thesis electronically, I declare that the entirety of the work contained therein is my own, original work, that I am the sole author thereof (save to the extent explicitly otherwise stated), that reproduction and publication thereof by Stellenbosch University will not infringe any third party rights and that I have not previously in its entirety or in part submitted it for obtaining any qualification.

Date: March 2018

Copyright © 2018 Stellenbosch University
All rights reserved.

Abstract

Design and Optimisation of Gap Waveguide Components through Space Mapping

C. Sibanda

*Department of Electrical and Electronic Engineering,
University of Stellenbosch,
Private Bag X1, Matieland 7602, South Africa.*

Thesis: MEng (Elec)

January 2018

This thesis presents a detailed approach and method to design and optimise ridge and groove gap waveguide components using input space mapping. Gap waveguides are expected to contribute significantly towards the implementation of microwave components especially for the millimetre and sub-millimetre wavelengths. This is due to their manufacturing flexibility, low loss and good power handling capabilities when compared to conventional rectangular waveguides and transmission lines.

The application of the space mapping technique to speed up the design and optimisation of gap waveguide components, which traditionally rely heavily on slower full wave simulations of the structures, is demonstrated through the use of simple circuit models. The application of a stripline model to design and optimise ridge gap waveguide components through space mapping is presented. Input space mapping, which is the most basic and original version of space mapping, is successfully applied in the optimisation of a 3-dB ridge gap waveguide power divider and hybrid coupler using a computationally cheap but faster stripline model.

A transmission line model is also used in the design and optimisation of third and fifth order narrow band ridge and groove gap waveguide coupled resonator Chebychev bandpass filters using an in-house input space mapping code. The bandpass filters are successfully designed and optimised in a relatively short time through the use of input space mapping with convergent results after only a few computational electromagnetic (CEM) simulations.

The results show that using the calculated design parameter values in filters, and generally in gap waveguide component designs, in most cases does not give an optimum design. The design parameters need to be tuned or optimised to meet the design specifications. The transmission line model is shown to give accurate results for the narrow band Chebychev bandpass filters.

The filter examples are directly optimised using a built-in computer simulation technology (CST) optimiser and the results are compared with those of input space mapping. The input space mapping technique is shown to give convergent results which meet the design specifications and is significantly faster than the conventional full-wave optimisation approach.

Opsomming

Ontwerp en Optimering van Gaping-Golfleier Komponente deur Ruimtekartering

(“Design and Optimisation of Gap Waveguide Components through Space Mapping”)

C. Sibanda

*Departement Elektriese en Elektroniese Ingenieurswese,
Universiteit van Stellenbosch,
Privaatsak X1, Matieland 7602, Suid Afrika.*

Tesis: MIng (Elec)

Januarie 2018

Hierdie tesis bied ’n gedetailleerde benadering en metode aan vir die ontwerp en optimering van rif en gleuf gaping-golfleier komponente deur intree ruimtekartering. Daar word verwag dat gaping-golfleiers ’n beduidende bydra sal maak in die implementering van mikrogolf komponente - veral in die millimeter en sub-millimeter golflengte bande. Dit is te danke aan die vervaardigings tegniek buigbaarheid, lae verliese en goeie drywing hanterings vermoë in vergelyking met konvensionele reghoekige golfleiers en transmissielyne.

Die toepassing van die ruimtekarteringstegniek op die versnelde ontwerp en optimering van gaping-golfleier komponente, wat tradisioneel swaar steun op volgolf numeriese elektromagnetiese simulاسies in hulle ontwerp, word deur die gebruik van eenvoudige stroombaan modelle geïllustreer. Die toepassing van ’n strooklyn model om rif gaping golfleier komponente te ontwerp en optimeer word voorgelê. Intree ruimte kartering, wat die eenvoudigste en oorspronklike weergawe van ruimtekartering is, word suksesvol toegepas in die optimering van ’n 3-dB rif gaping-golfleier drywingsverdeler en hibriede koppelaar deur van ’n numeriese goedkoop en vinniger strooklyn model gebruik te maak.

’n Transmissielyn model word ook gebruik in die ontwerp en optimering van derde en vyfde orde nouband rif en gleuf gaping-golfleier gekoppelde resoneerder Chebyshev banddeurlaatfilters deur van ’n in-huis ruimtekartering kode gebruik te maak. Die banddeurlaatfilters word in ’n relatiewe kort

tydperk ontwerp en geoptimeer deur van intree ruimtekartering gebruik te maak, en gekonvergeerde resultate word na slegs 'n paar numeriese elektromagnetiese simulاسie lopies verkry. Die resultate toon dat om die oorspronklike ontwerpparameters te gebruik in filters, en in die algemeen in gaping-golfleier komponente, in meeste gevalle nie die optimum resultate tot gevolg het nie. Die ontwerpparameters moet ingestem en geoptimeer word om die ontwerpspesifikاسies te haal. Daar word getoon dat die transmissielyn modelle redelike akkurate resultate vir die nouband Chebychev filters lewer.

Die filter voorbeelde word ook direk geoptimeer deur van die ingeboude optimeerder in CST gebruik te maak, en die resultate word vergelyk met die van die intree ruimtekartering. Daar word sodoende getoon dat die intree ruimtekarterings tegniek konvergente resultate lewer, wat die ontwerp spesifikاسie haal, en dat dit beduidend vinniger is as die konvensionele volgolf optimerings tegniek.

Contents

| | |
|--|-------------|
| Declaration | i |
| Abstract | ii |
| Opsomming | iv |
| Contents | vi |
| List of Figures | viii |
| List of Tables | xi |
| Nomenclature | xii |
| 1 Introduction | 1 |
| 1.1 Introduction | 1 |
| 2 Gap Waveguide Technology | 5 |
| 2.1 Introduction | 5 |
| 3 Space Mapping | 11 |
| 3.1 Introduction | 11 |
| 3.2 Input Space Mapping | 14 |
| 3.3 Design of Microstrip Bandstop Stub Filter Using Space Mapping | 15 |
| 4 Optimisation of Gap Waveguide Components through Space Mapping | 20 |
| 4.1 Introduction | 20 |
| 4.2 T-Junction Power Divider | 28 |
| 4.3 Optimisation of 3-dB Ridge Gap Waveguide T-Junction Power Divider Using Input Space Mapping | 29 |
| 4.4 Design and Optimisation of a 3-dB Ridge Gap Waveguide Hybrid Coupler Using Input Space Mapping | 34 |
| 5 Optimisation of Microwave Gap Waveguide Bandpass Filters Using Space Mapping | 41 |

CONTENTS

vii

| | | |
|----------|--|-----------|
| 5.1 | Bandpass Filter Basics | 41 |
| 5.2 | Narrow Band Microwave Groove Gap Waveguide Coupled Resonator Bandpass Filters | 48 |
| 5.3 | Third Order Narrow Band Microwave Ridge Gap Waveguide Coupled Resonators Bandpass Filter | 66 |
| 6 | Conclusion | 75 |
| | List of References | 78 |

List of Figures

| | | |
|------|---|----|
| 2.1 | Ridge gap waveguide dimensions and propagation regions | 6 |
| 2.2 | Groove gap waveguide propagation regions | 6 |
| 2.3 | Unit cell | 7 |
| 2.4 | Dispersion graph for a double transition unit cell | 8 |
| 2.5 | Double transition ridge gap waveguide | 8 |
| 2.6 | S-parameter results for double transition ridge gap waveguide | 9 |
| 2.7 | E-field total amplitudes for double transition for 9 - 16 GHz | 10 |
| 2.8 | E-field amplitudes for double transition for 17 - 22 GHz | 10 |
| 3.1 | MWO stopband filter coarse model 3-D diagram | 16 |
| 3.2 | MWO $ S_{21} $ coarse model response curve | 16 |
| 3.3 | CST 3-D diagram of the microstrip filter | 17 |
| 3.4 | CST $ S_{21} $ fine model response curve | 17 |
| 3.5 | Coarse, fine and aligned surrogate models | 18 |
| 3.6 | CST $ S_{21} $ fine model response curve | 19 |
| 4.1 | Ideal stripline and TEM propagation mode | 21 |
| 4.2 | Half stripline | 21 |
| 4.3 | Gap waveguides and their equivalent rectangular waveguides | 24 |
| 4.4 | Ridge gap/ridged rectangular waveguides dispersion graphs for h = 0.5 | 25 |
| 4.5 | Ridge gap/ridged rectangular waveguides dispersion graphs for h = 1 | 25 |
| 4.6 | Ridge gap/ridged rectangular waveguides dispersion graphs for h = 2 | 26 |
| 4.7 | Ridge gap/ridged rectangular waveguides dispersion graphs for h = 3 | 26 |
| 4.8 | Groove/hollow waveguide dispersion graphs | 27 |
| 4.9 | (a) Groove waveguide port arrangement and (b)ridge waveguide port arrangement | 27 |
| 4.10 | Best waveguide port configuration and dimensions | 28 |
| 4.11 | Transmission line model of a power divider | 29 |
| 4.12 | MWO stripline coarse model schematic | 31 |
| 4.13 | MWO stripline coarse model response | 31 |

| | | |
|------|--|----|
| 4.14 | CST 3-D fine model diagram | 32 |
| 4.15 | Cross sectional dimensions of double and single ridged waveguides . | 33 |
| 4.16 | CST fine model first iteration | 34 |
| 4.17 | CST fine model second iteration | 35 |
| 4.18 | Hybrid coupler schematic diagram | 36 |
| 4.19 | MWO coupler coarse model schematic diagram | 37 |
| 4.20 | MWO coupler coarse model S-parameters | 38 |
| 4.21 | CST coupler 3-D fine model | 38 |
| 4.22 | CST coupler fine model initial S-parameters | 39 |
| 4.23 | Alignment step and the aligned models | 39 |
| 4.24 | Second iteration and the fine model S-parameters response | 40 |
| | | |
| 5.1 | Chebyshev transmission function response | 42 |
| 5.2 | Lumped element lowpass filter circuit | 44 |
| 5.3 | Impedance Inverter model for Chebyshev bandpass filter | 45 |
| 5.4 | K-Inverter equivalent lumped elements circuit | 45 |
| 5.5 | Electric wall and magnetic wall symmetry method | 46 |
| 5.6 | Two resonator arrangement for the S-parameter method | 49 |
| 5.7 | Main-line coupling S-parameters | 49 |
| 5.8 | Approximated graph of K and inter-resonator distance s (mm) . . | 50 |
| 5.9 | Eiegemmode solver method | 51 |
| 5.10 | Mode 1 | 52 |
| 5.11 | Mode 2 | 52 |
| 5.12 | Eigenmode solver method for K and s | 53 |
| 5.13 | Group delay method with resonator and SMA port distance x . . . | 54 |
| 5.14 | Typical circuit model of source and first resonator | 54 |
| 5.15 | Group delay of the S_{11} Phase | 56 |
| 5.16 | Group delay values and distance x | 57 |
| 5.17 | Group delay frequency and distance x | 57 |
| 5.18 | External quality factor Q_{ex} and SMA port position x | 58 |
| 5.19 | Third order bandpass filter coarse model | 59 |
| 5.20 | Third order bandpass filter coarse model S-parameters | 59 |
| 5.21 | Fine model and design parameters | 60 |
| 5.22 | Third order first iteration | 61 |
| 5.23 | Third order last iteration | 61 |
| 5.24 | Space mapping and Direct optimisation Fine model S-parameters . | 62 |
| 5.25 | Fifth order coarse model schematic | 63 |
| 5.26 | Fifth order coarse model S-parameters | 63 |
| 5.27 | Fifth order fine model | 64 |
| 5.28 | First iteration evaluation response of the fine model | 64 |
| 5.29 | Last iteration response of the fine model | 65 |
| 5.30 | Space mapping and Direct optimisation fine model S-parameters . . | 65 |
| 5.31 | Ridge gap waveguide view and dimensions | 67 |
| 5.32 | Ridge gap waveguide resonators for main-line coupling | 68 |

| | |
|--|----|
| 5.33 Eigenmode solver method for K and s | 68 |
| 5.34 Group delay method for Q_{ex} and distance x | 69 |
| 5.35 External quality factor Q_{ex} and distance x | 70 |
| 5.36 Coarse model schematic diagram | 71 |
| 5.37 Coarse model S-parameters | 71 |
| 5.38 Fine model and design parameters | 72 |
| 5.39 S-parameters for the first iteration | 73 |
| 5.40 S-parameters for the last iteration | 73 |
| 5.41 Space mapping and Direct optimisation fine model S-parameters . . | 74 |

List of Tables

| | | |
|-----|--|----|
| 3.1 | Alignment between coarse and fine models using $R_s = R_c + c$ | 18 |
| 3.2 | New stub length design value | 18 |
| 4.1 | Alignment step | 37 |
| 4.2 | New coarse model design values | 39 |
| 5.1 | Coupling K and corresponding inter-resonator distance s | 50 |
| 5.2 | Filter initial and optimum design parameter values | 62 |
| 5.3 | Filter initial and final design parameter values | 66 |
| 5.4 | Filter initial and optimum design parameter values | 72 |

Nomenclature

Abbreviations

| | |
|-----|--------------------------------|
| CEM | Computational Electromagnetic |
| CST | Computer Simulation Technology |
| E | Electric |
| EM | Electromagnetic |
| MWO | Microwave Office |
| PEC | Perfect Electric Conductor |
| PMC | Perfect Magnetic Conductor |
| TE | Transverse Electric |
| TEM | Transverse Electromagnetic |

Chapter 1

Introduction

1.1 Introduction

The main objective of this thesis, is the application of space mapping in the design and optimisation of microwave gap waveguide components. Most microwave components and circuits are mainly based on conventional waveguides and transmission lines. However, for the millimetre and sub-millimetre wavelengths, the above-mentioned technologies have high losses, are difficult to fabricate and their production cost can be high. For example, microstrip transmission line based microwave components and devices for the millimetre and sub-millimetre wavelengths have high losses due to the presence of dielectric in microstrip.

1.1.1 Hollow Rectangular Waveguides

At millimetre and sub-millimetre waves range, the fabrication of hollow rectangular waveguides can be very difficult. Often joint imperfections may result from joining of plates in the fabrication process. These mechanical joint imperfections can result in field leaks, poor electrical contact and can also compromise the waterproofing, leading to oxidation of the waveguide component which may degrade its performance. Poor electrical contact between the plates in rectangular waveguide is one of the common sources of passive intermodulation [1]. Hence high precision machining techniques and good alignment of metal plates are required for fabrication and mechanical assemble of conventional hollow waveguides for millimetre and sub-millimetre wavelength microwave applications. This often leads to high production cost and delays if large volumes are to be produced. Therefore, the use of conventional waveguides may not be a good economic option for the millimetre and sub-millimetre microwave frequency range.

1.1.2 Gap Waveguide Technology

This thesis will look at application of space mapping for the design and optimisation of new gap waveguide microwave components. Gap waveguide is a new technology that is mainly used to make low-loss components and circuits at millimetre and sub-millimetre waves. There are three main major gap waveguides types. These are the ridge, groove and microstrip waveguides [2]. This thesis will only cover the ridge and groove gap waveguides.

The gap waveguides are expected to contribute significantly towards the microwave system components especially for the millimetre and sub-millimetre wavelengths. This is due to their manufacturing flexibility, low loss and good power handling capabilities. There are gap waveguide components that have already been designed, measured and verified. These include the ridge gap waveguide power divider [3, 4] and the groove gap waveguide coupled resonator filters with high Q resonators [5]. Other designed components include a V-band groove gap waveguide diplexer [6], wide band slot antenna array with single layer corporate feed network with ridge gap waveguide technology [7] and a 76 GHz multi-layered phased array antenna using a non-metal contact metamaterial waveguide [8]. The gap waveguide technology can also be used for packaging of the microstrip line circuits for suppressing the unwanted radiations with no cavity resonance over a wide bandwidth [9]. Active components like amplifiers and microwave monolithic integrated circuits (MMICs) can be included within the gap waveguide packaging with self-cooling and shielding instead of using the normal metal for shielding [10].

The design and optimisation of microwave gap waveguide components is mainly dependant on full wave microwave solvers. Most available commercial full wave electromagnetic (EM) microwave solvers like Computer Simulation Technology (CST) have a built-in optimiser which can also be used for optimisation of gap waveguide components. However these direct optimisers usually take a long time due to the large number of function evaluations (full wave simulations) required.

1.1.3 Space Mapping

As already stated in the gap waveguide section the design and optimisation of microwave gap waveguide components is mainly dependant on full wave microwave solvers. The full wave solution is the most accurate we can find, and thus optimisation of the full wave solution provides the most accurate design (if the optimisation converges). However, to optimise these gap waveguide components using full wave microwave solvers takes a long time. Alternatively, we can find and use a simple circuit model approximations

of the structure to do the optimisation much quicker. These simple circuit models are fast and computationally cheap, but unfortunately they are not always accurate and it is often very difficult to model all the relations between physical dimensions and circuit model electrical properties.

The properties and attributes of the two can be combined to speed up the design and optimisation process. Space Mapping bridges the gap between the two by shifting the optimisation burden onto the circuit model of the device under design, while the full wave solvers are used to augment the circuit model somehow to make it more accurate.

Space mapping is a universal and a faster computer aided design and optimisation method which can be used for faster design and optimisation in many engineering disciplines. This optimisation technique can be applied in the design and optimisation of simple to complex microwave electromagnetic circuits. The application and advantages of space mapping in a number of engineering disciplines have been widely demonstrated like in aero-engine design and optimisation [11], vehicle structural optimisation of crashworthiness problems [12] and design and optimisation of electromagnetic systems [13].

In space mapping, the actual component to be optimised is referred to as the fine model. The equivalent circuit model is referred to as the coarse model. The transformed or mapped coarse model to align it with fine model is referred to as the surrogate model.

There are many different types of space mapping optimisation techniques. A brief description of some of them will be given. Input space mapping is the most basic and original version of space mapping. In input space mapping, the design parameters are used for the alignment of the coarse and fine models and for optimisation of the resultant surrogate to get new design parameters [14]. Implicit Space Mapping (ISM) is one of the most common. It uses the pre-assigned parameters for matching of the fine and coarse models instead of the design parameters [15]. The pre-assigned parameters are the non-design parameters which include physical-based parameters like relative dielectric constant and substrate height. In Output Space Mapping (OSM) the surrogate model is updated according to the difference between the coarse and fine model responses at each iteration [16] where the responses are the output functions of the two models. In Frequency Space Mapping, the frequency axis of the coarse model is shifted and stretched (in a linear fashion) to find a surrogate model that best fits the fine model [16]. Input space mapping will be used for design and optimisation of all the microwave gap waveguide components in this thesis.

1.1.4 Thesis Outline

This thesis will start by explaining the general gap waveguide theory. This will be followed by the definition of the space mapping optimisation technique. The coarse and fine models and their roles in space mapping will be explained. Input space mapping will be manually applied in the optimisation of a basic bandstop filter example which has one design parameter to demonstrate the concept. Space mapping will then be extended to optimisation of a 3-dB ridge gap waveguide power divider and a hybrid coupler with many design parameters.

The use of a stripline to model ridge gap waveguide components will be analysed and discussed. The equivalence between ridge/groove gap waveguides and ridged/rectangular waveguides in the operating band (normally called stopband in gap waveguides) will be analysed through plots of dispersion diagrams. The stripline model will be used in the design and optimisation of a 3-dB ridge gap waveguide power divider and a 3-dB ridge gap waveguide hybrid coupler using an in-house input space mapping code.

A Chebyshev bandpass filter will be defined in terms of its transfer function response in the passband and stopband regions. This will be followed by a general description of a narrow band coupled resonator bandpass filter and its implementation. The impedance inverter K model of a Chebyshev bandpass filter will be discussed. The coupling factor K between two adjacent resonators and the external quality factor Q_{ex} of the first and last resonators and the need to translate these two electrical parameters into some physical dimensions for realisation of actual bandpass filters will be explored. The methods to analyse, calculate and translate the two electrical parameters into physical dimensions for realisation of a third order and fifth order narrow band microwave groove gap waveguide coupled resonator Chebyshev bandpass filters will be analysed. The same methods will be applied for realisation of a third order narrow band microwave ridge gap waveguide coupled resonator bandpass filter.

The use of half wavelength transmission lines to model both groove and ridge gap waveguide resonators will be explored. The transmission line model will be applied in the design and optimisation of the three above mentioned gap waveguide Chebyshev bandpass filters through an in-house input space mapping code. The results of space mapping optimisation will be analysed and for comparison all the three filter examples will be directly optimised using CST optimiser. The results of the two methods will be analysed and discussed.

Chapter 2

Gap Waveguide Technology

2.1 Introduction

Gap waveguide is a new technology that is mainly used to make low-loss components and circuits at millimetre and sub-millimetre wavelengths. This new non-planar microwave circuit technology was first proposed by P.-S. Kildal and others [17, 2, 18, 19]. Two parallel plates with no physical contacts are used to realise a gap waveguide. The lower plate has some periodic metal pins machined onto it, with a central continuous ridge or a groove in between the pins. The guide can be completely open on the sides. There are three gap waveguide types. This thesis will mainly focus on ridge and groove waveguides.

The region between the ridge's upper surface and the smooth electric perfect conductor (PEC) plate above it, normally referred to as gap, is vacuum and should be smaller than a quarter wavelength ($< \frac{\lambda}{4}$) of the propagating mode. The height of the pins should be about a quarter wavelength. At this height the pins act like an artificial perfect magnetic conductor (PMC) material. Above the pins there is a smooth PEC plate, with the two separated by vacuum gap. In the PMC-PEC (pin-plate) region, all the global parallel plate waveguide propagating modes will be stopped in all directions. However a transverse electromagnetic (TEM)-like mode will propagate along the central ridge in the ridge gap waveguide. This mode propagates in the vacuum gap between the ridge upper surface and PEC plate above it. A transverse electric (TE) mode will propagate in the groove gap waveguide along the groove [20]. The groove gap waveguide will be discussed later. However all the conditions and dimensions discussed above also apply to the groove gap waveguide. The schematic diagram of propagation and non-propagation regions of a ridge and groove gap waveguides are shown in Figs. 2.1 and 2.2. The following section will discuss the stopband of the gap waveguide.

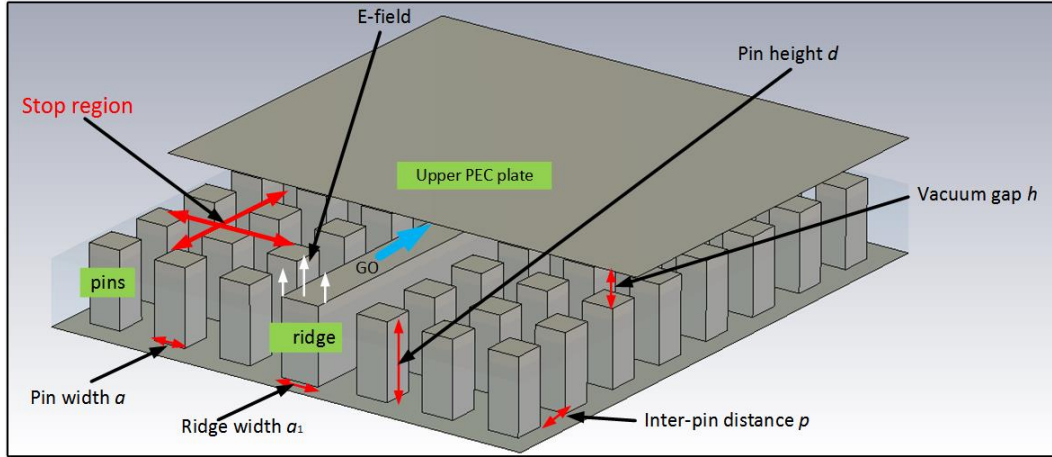


Figure 2.1: Ridge gap waveguide dimensions and propagation regions

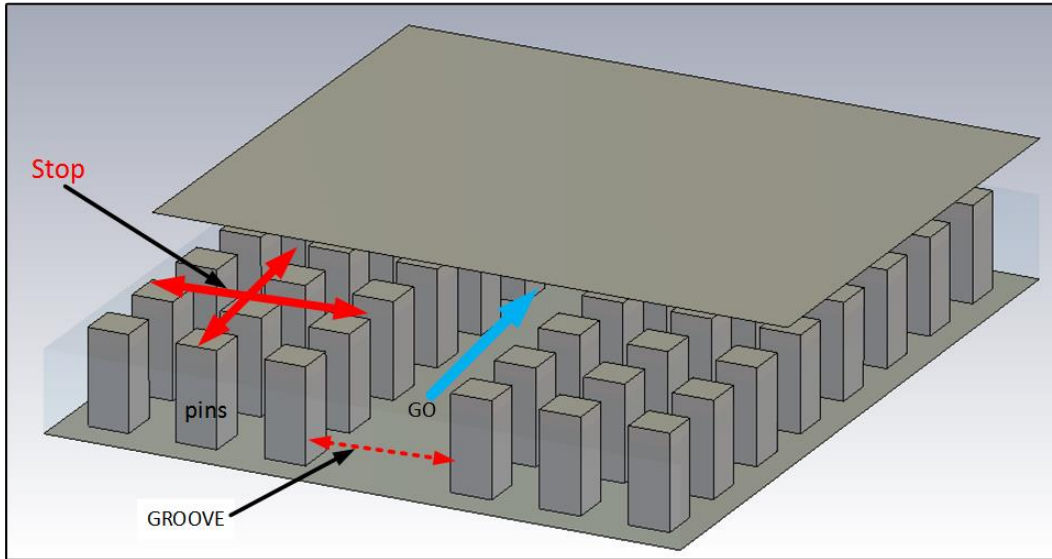


Figure 2.2: Groove gap waveguide propagation regions

2.1.1 Gap Waveguide Stopband

The propagation bandwidth in the gap waveguides is called the stopband. The stopband stops all the parallel plate waveguide modes in the pin regions, and only allow a single mode in the ridge/groove region. The stopband is a very important parameter in the operation of the gap waveguide. It is realised when the above stated waveguide dimensions are implemented.

The main parameters that determine the stopband of the gap waveguide are pin height d which should be about a quarter wavelength, pin width a , distance between the pins p and vacuum gap height h . The gap height should

be less than a quarter wavelength. The sum of pin height d and gap height h should be less than half wavelength of the propagating mode frequency and this determines the upper frequency bound. The lower frequency bound is determined by pin height d which should be a quarter wavelength high.

A dispersion diagram was plotted using the eigenmode solver in CST for a unit cell of the double transition demonstrator which will be discussed later. The unit cell 3-D diagram is shown in Fig. 2.3 and all the dimensions are in mm. The dispersion plot results are shown in Fig. 2.4. The stopband is shown in Fig. 2.4 and is between 10.5 - 21.5 GHz. The propagating mode in the stopband is also shown. The other parallel waveguide global modes are also shown in Fig. 2.4 in relation to the stopband as discussed above.

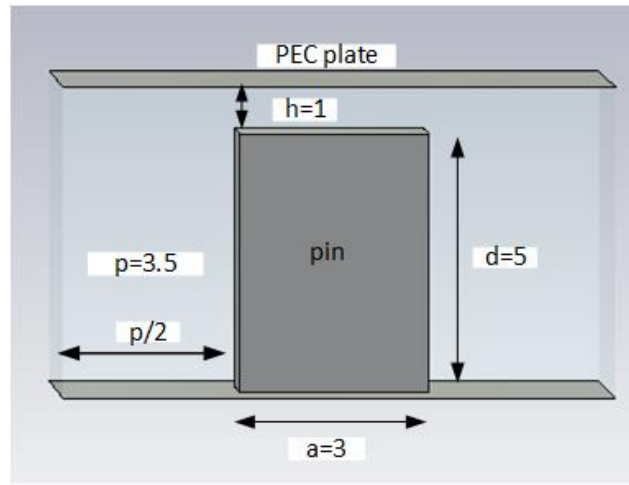


Figure 2.3: Unit cell

Some of the gap waveguide design examples discussed in this thesis will be based on a 10 - 20 GHz stopband realised from square metal pins. The typical pin and structure dimensions for this stopband are as shown in the unit cell of Fig. 2.3 [9].

2.1.2 Demonstrator With Two 90° Bends and Coaxial Transitions

The confinement of propagation along the ridge and the distribution of the electric (E)-field in and outside the stopband in a ridge gap waveguide was investigated. A demonstrator with two 90° bends and two SMA port transitions [18] was used and simulated in CST for the reflection coefficient S_{11} and transmission coefficient S_{21} . The dimensions are similar to those of the unit in Fig. 2.3. The demonstrator is shown in Fig. 2.5. Open boundaries

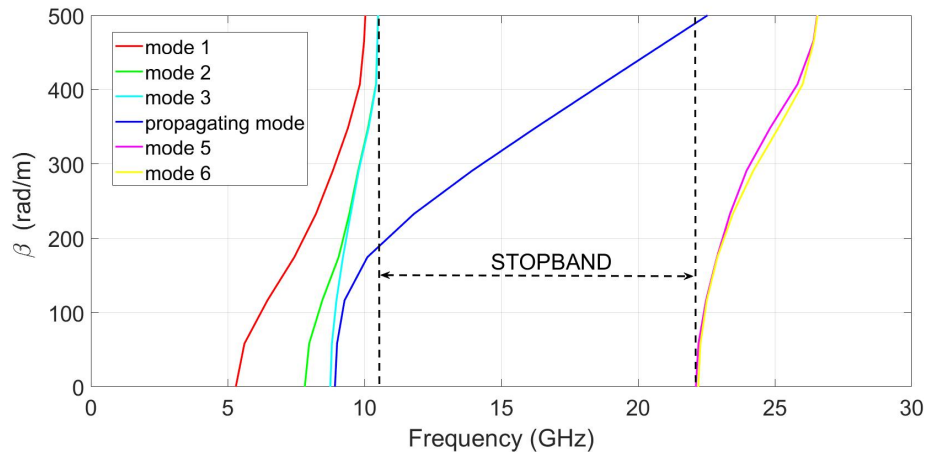


Figure 2.4: Dispersion graph for a double transition unit cell

were used in this simulation. The demonstrator was fed through SMA ports which were capacitively coupled through holes in the ridge. Waveguide ports could have been used in the feed line of the demonstrator. The use of SMA ports and waveguide ports in the feed lines of both ridge and groove waveguides will be discussed in Chapter 5.

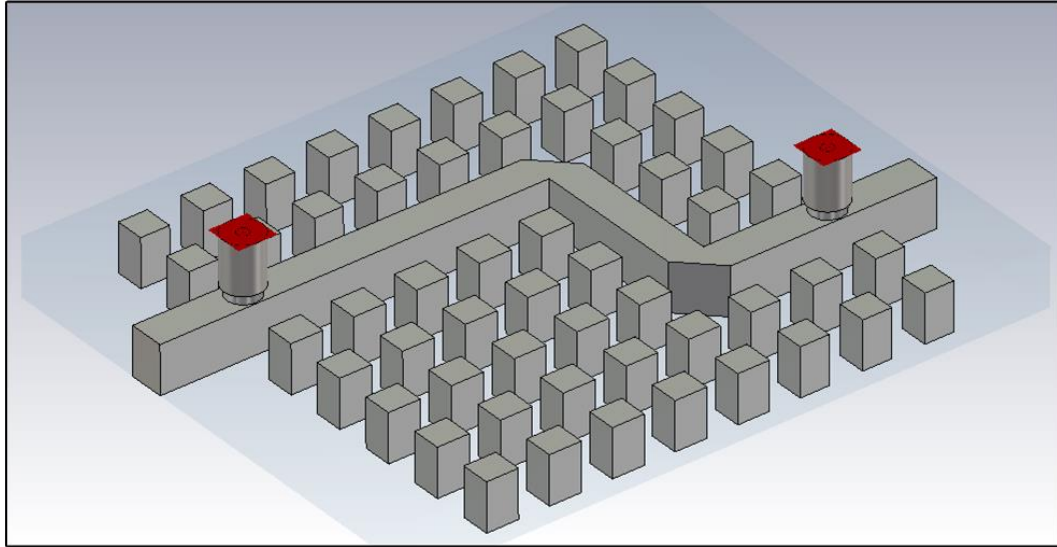


Figure 2.5: Double transition ridge gap waveguide

The S-parameter results of the demonstrator are shown in Fig. 2.6. The total E-field plots for the demonstrator were also done for the 9 - 22 GHz frequency range and the results are shown in Figs. 2.7 and 2.8 with the field magnitude scale also shown. The total E-field distribution in the

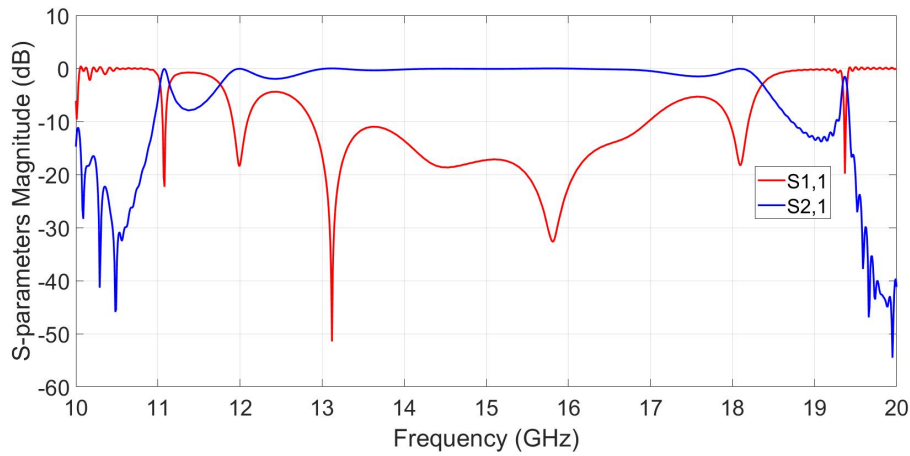


Figure 2.6: S-parameter results for double transition ridge gap waveguide

whole component was analysed. Within the stopband the E-field is large and confined along the ridge and also follow the ridge. The E- field confinement is clearly defined along the ridge for 12 - 18 GHz frequency bandwidth. This is in agreement with S-parameter results of Fig. 2.6. For frequencies below 10 GHz the fields are all over the structure as there are now multiple propagating modes in the pins region (from the dispersion diagram), so the field is no longer confined to a single propagating mode along the ridge. For 19 - 21 GHz frequencies, the field amplitude becomes smaller and very weak as the 20 GHz upper bound frequency mark is approached. Higher order modes start propagating here, changing the apparent characteristic impedance of the ridge gap waveguide. The E-field magnitude and distribution plots show the effect of the stopband, the confinement of propagation along the ridge and this tallies with the results of Fig. 2.6 and the dispersion diagram.

2.1.3 Groove Gap Waveguide

The groove gap waveguides have two parallel plates with no physical contacts just like the ridge gap waveguide. All the structure dimensions of the ridge gap waveguide discussed above also apply to the groove waveguide. However, for the groove gap waveguide the propagation is along the groove which is in between the pins rows. Also the propagating mode in the groove gap waveguide is a TE mode. The schematic diagram of the propagation and non-propagation regions of a groove gap waveguide is shown in Fig. 2.2.

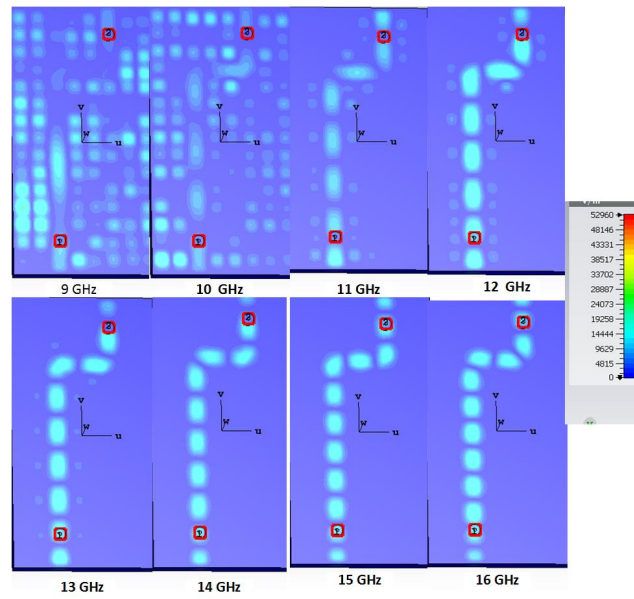


Figure 2.7: E-field total amplitudes for double transition for 9 - 16 GHz

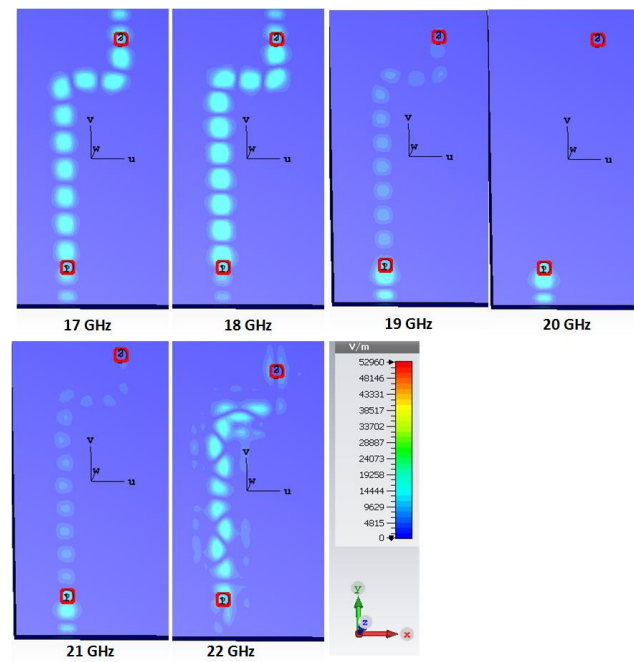


Figure 2.8: E-field amplitudes for double transition for 17 - 22 GHz

Chapter 3

Space Mapping

3.1 Introduction

Direct optimisation of microwave components using EM microwave simulators is usually a time-consuming procedure. Although direct optimisation of microwave fine model components is very accurate, it is computationally expensive. It usually takes many design iterations to determine the optimal design parameters. As the design parameters increase and for complex microwave circuits, full wave EM microwave simulators intensely increase usage of the computer's CPU.

Instead of direct optimisation of slower, computationally expensive but accurate fine model, space mapping is based on the use of a faster, computationally cheap but less accurate coarse model. The coarse model is typically an equivalent circuit model of the actual component structure - the fine model. The coarse model should have same physical attributes and properties as the fine model. There are several efficient space mapping optimisation techniques for electromagnetic circuits [21, 22, 15, 16]. Space mapping techniques make use of the knowledge and properties of the inaccurate but less expensive and simple coarse model for optimisation. The fine model is only evaluated at the position in the parameter space where the coarse model is at an optimum and the data of the fine model is used to align the coarse model to the fine model and thus get an improved surrogate model at the current point in the design space. The surrogate model is the transformed or mapped coarse model to align it with fine model.

3.1.1 Basic Space Mapping Procedure

In space mapping, the coarse model is optimised first to obtain the design parameters that satisfy the design specifications. The resultant optimal coarse model design parameters are then used to evaluate the fine model. The first evaluation iteration of the fine model will typically give a response that does

not satisfy the design specifications. The two responses of the coarse and fine models are then matched through a parameter extraction. Parameter extraction is the mapping or transformation of the coarse model to match it with the fine model. The initial difference or misalignment between the two model responses should be reasonably small for application of space mapping.

The coarse model which has been transformed or mapped to match the fine model response is called the surrogate model. The surrogate model is then optimised to obtain new design parameters values. The new design parameters values are used to evaluate the fine model, usually resulting in an improved response in terms of design specifications. The fine model is thus only used to evaluate and validate whether specification goal has been met and to provide data for the next iteration as explained above. The above-mentioned cycle is repeated and only stopped when the fine model response meets the design specifications, or the shift in the design space becomes smaller than a specified tolerance.

3.1.2 Space Mapping Algorithm

The design objective is to calculate an optimal solution for the fine model as follows :

$$x_f^* = \arg \min_x U(R_f(x)) \quad (3.1)$$

where U is some suitable objective function, x_f^* is the desired optimal design goal, x denotes the fine model design parameters and R_f is the fine model response vector. In microwave circuits, U is usually a min-max function with lower and upper specifications [23]. The fine model response vector, R_f , could be for example be reflection coefficient $|S_{11}|$ at selected frequency points. An iterative procedure is used by general space mapping to solve equation (3.1) through:

$$x^{(k+1)} = \arg \min_x U(R_s(x, p^k)) \quad (3.2)$$

where $R_s(x, p)$ refers to the surrogate model's space mapping response vector with x representing design parameters and p is the coarse model extracted parameters. The parameter extraction procedure for calculating the value of p^k at the k -th iteration in which we try to match the coarse and the fine models is:

$$p^k = \arg \min_x \sum_{j=0}^k w_j ||R_f(x^k) - R_s(x^k, p)|| \quad (3.3)$$

where w_j are the scaling factors which determine the contribution of the previous iteration points to the parameter extraction procedure. The term

$$||R_f(x^k) - R_s(x^k, p)||$$

indicates a norm, and we use the complex functions R_f and R_s in the alignment. The alignments thus involves minimising the distance between the fine and the surrogate model responses in the complex plane. Composing the coarse model, R_c with suitable transformations to match it with fine model gives rise to a surrogate model, R_s .

3.1.3 Space Mapping Steps

There are several efficient space mapping optimisation techniques for electromagnetic microwave circuits. All the space mapping optimisation techniques broadly follow the listed steps:

Step (1): Select a mapping function (Linear, Non-linear)

Step (2): Select an approach (for example - explicit, implicit)

Step (3): Optimise the coarse/surrogate model with respect to design parameters

Step (4): Simulate the fine model using coarse/surrogate model's optimum values

Step (5): End if design specification (e.g. transmission coefficient $|S_{21}|$ response specifications) is satisfied, if not go to step (6)

Step (6): Depending on approach type used in step (2), the coarse model is mapped or matched to the fine model. For example, in implicit space mapping, the non-design and fixed coarse model parameters normally referred to as preassigned parameters are used to align the fine and coarse models instead of the design parameters. The coarse model plus the mapping function to match it with fine model will result in a surrogate model.

Step (7): Repeat steps (3), (4) and (5)

3.1.4 Implicit Space Mapping

Implicit space mapping (ISM) use preassigned and non-design parameters for matching of the fine and the coarse/surrogate models. These non design

parameters are called preassigned parameters. The preassigned parameters are tuned to match the coarse and fine model responses instead of the design parameters as already stated above. The non-design parameters may include physical-based parameters like relative dielectric constant and substrate height. Implicit spacing mapping steps are as same as those discussed in section 3.2.

3.2 Input Space Mapping

Input space mapping use the design parameters for matching between fine and coarse models and optimisation of the coarse/surrogate model. In input space mapping, the surrogate model is defined as a linear transformation of the coarse model [14]. Using scalar quantities for simplicity the surrogate model can be expressed as:

$$R_s(x, p) = R_s(x, B, c) = R_c(Bx + c). \quad (3.4)$$

The simplified form of (3.4) with a B scaling factor of 1, can be written as:

$$R_s = R_c + c \quad (3.5)$$

where

R_s is the surrogate model,

R_c is the coarse model and

c is the extracted parameter.

Equation (3.5) is used for alignment of the coarse and fine models in the parameter extraction step. The resultant surrogate is optimised to get new design variable values. If by design an optimum coarse model is used, the optimisation step becomes redundant and this is the case with some design examples in this thesis. To get new coarse model design parameters, (3.5) is re-arranged as follows:

$$R_c = R_s - c. \quad (3.6)$$

The new coarse model design parameter values are used to evaluate the fine model for validation of design specification. If fine model evaluation does

not meet the design specification, the alignment step is repeated and only terminated after the design specification is met or when the change in the design variables in successive iterations becomes smaller than a specified tolerance. Input space mapping will be used in this thesis for the design and optimisation of the microstrip stopband filter in the following section. The optimisation step was redundant in this example because an optimum coarse model by design was used.

3.3 Design of Microstrip Bandstop Stub Filter Using Space Mapping

This section will highlight the application of the input space mapping method for design and optimisation of a basic microstrip bandstop filter. The design and optimisation of the bandstop filter with one design parameter will be used to illustrate the space mapping concept. Input space mapping will then be used for the optimisation of a 3-dB T-junction ridge gap waveguide power divider and hybrid coupler with multiple design parameters in Chapter 4. The application of space mapping for design and optimisation of groove and ridge gap waveguide filters with multiple design parameters will be done in Chapter 5 using an in-house input space mapping code.

The microstrip bandstop filter [14] was used in this example. The goal was to find the optimum stub line length L_2 of the microstrip bandstop filter for a centre frequency of 5 GHz. The design line length L_2 is the middle section line in Fig. 3.1. The microstrip had a substrate of relative permittivity $\epsilon_r = 2.2$, substrate height $H = 0.5$ mm and strip thickness $T = 0.0035$ mm. A line width of 1.6 mm was set and fixed for all the three lines.

Microstrip transmission line was used for coarse modelling the bandstop filter. The schematic diagram of the microstrip filter and the design parameter line length L_2 is shown in Fig. 3.1. NI AWR microwave office (MWO) was used for microstrip coarse model simulation. The initial design line length of L_2 is 10.679 mm. The coarse model transmission coefficient S_{21} was chosen as the design goal type. The coarse model response is shown in Fig. 3.2.

The initial optimum design line length value of the coarse model was used to evaluate the fine model. The microstrip bandstop filter fine model was simulated using computer simulation technology (CST) microwave studio. The CST fine model 3-D diagram and the design length is shown in Fig. 3.3 and its initial response is shown in Fig. 3.4.

From Fig. 3.4, the CST fine model transmission coefficient S_{21} evaluated

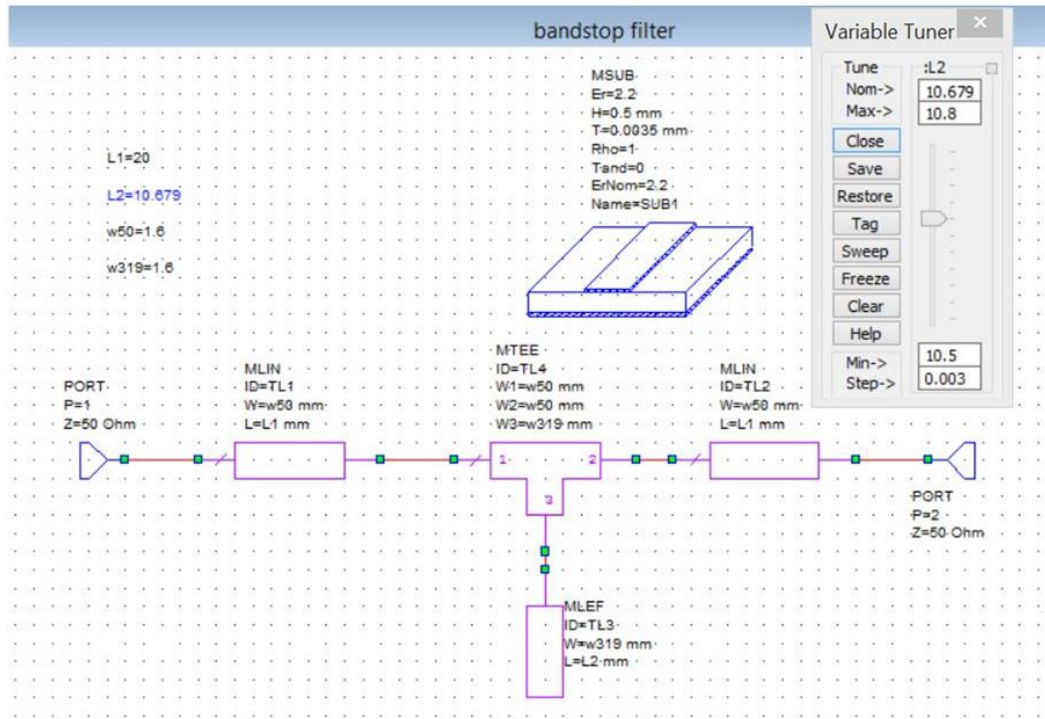


Figure 3.1: MWO stopband filter coarse model 3-D diagram

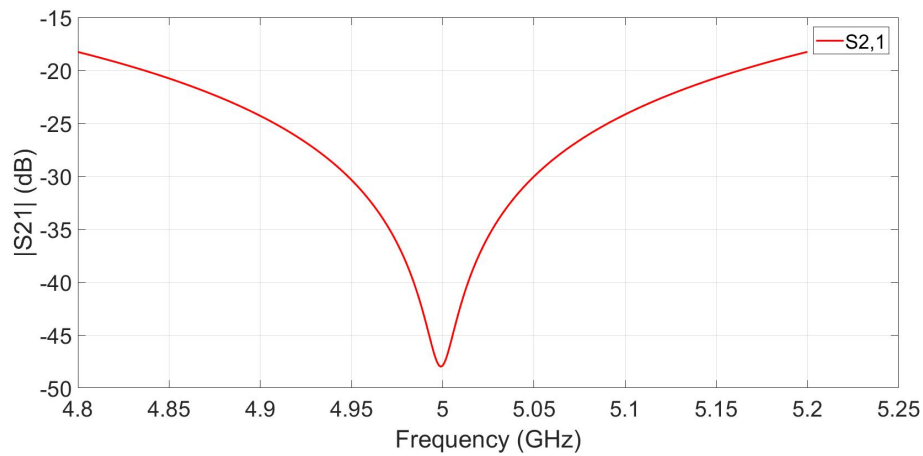


Figure 3.2: MWO $|S_{21}|$ coarse model response curve

using the initial design stub length value has a centre frequency of 4.953 GHz. This is off the 5 GHz design specification centre frequency.

The next step was to align the coarse model and the the fine models. The alignment of coarse and fine models step was done manually using the embedded tuner in MWO. This alignment step, though was manually done, is

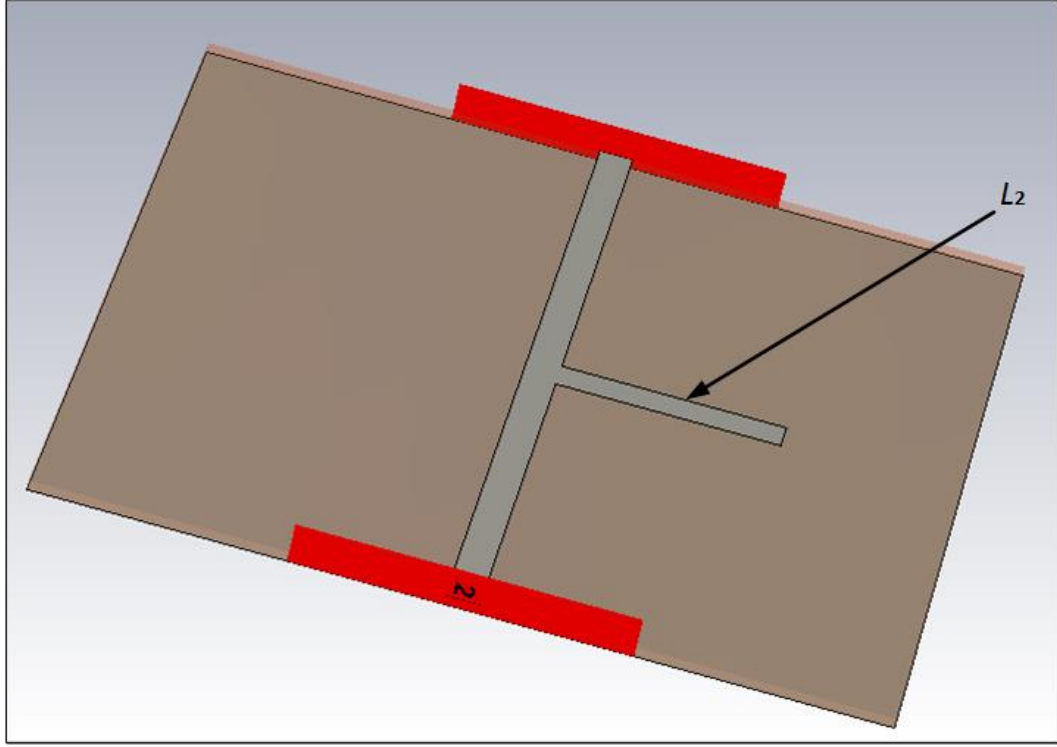


Figure 3.3: CST 3-D diagram of the microstrip filter

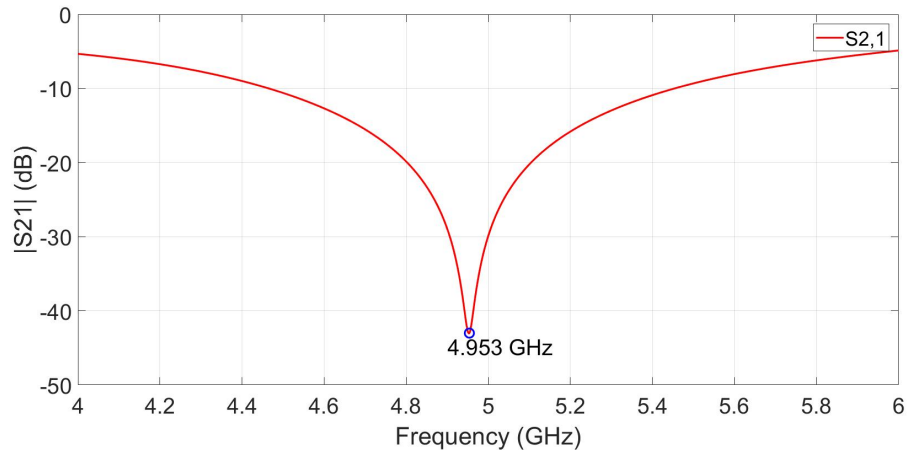


Figure 3.4: CST $|S_{21}|$ fine model response curve

normally implemented through application of (3.5) in input space mapping.

The transformation of the coarse model for alignment with the fine model resulted in a surrogate model. The aligned surrogate model had a line length L_2 value of 10.777 mm and hence the extracted parameter c value was $(10.777 - 10.679) = 0.098$ mm. The values of the surrogate model, coarse model

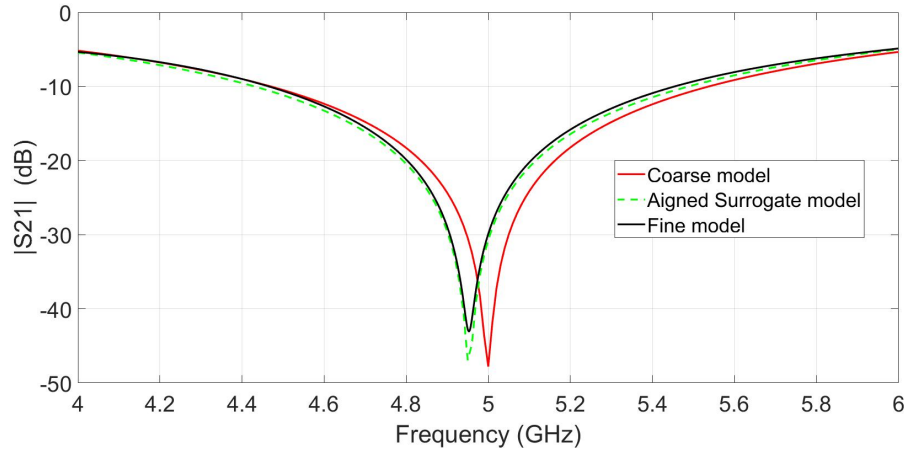
| Design Variable | Surrogate (R_s) | Coarse (R_c) | Parameter c |
|-----------------|---------------------|------------------|---------------|
| L_2 | 10.777 | 10.679 | 0.098 |

Table 3.1: Alignment between coarse and fine models using $R_s = R_c + c$

| Design Variable | Surrogate (R_s) | New value (R_c) | Parameter c |
|-----------------|---------------------|---------------------|---------------|
| L_2 | 10.679 | $10.679 - 0.098$ | 0.098 |

Table 3.2: New stub length design value

and extracted parameter for the alignment step are summarised in Table 3.1. The three S_{21} responses for the coarse model, fine model and the aligned surrogate model are shown in Fig. 3.5.

**Figure 3.5:** Coarse, fine and aligned surrogate models

The surrogate model was optimised to get the new design value of line length L_2 . This optimisation step was redundant in this example because an optimum coarse model by design was used as already stated. The new line length design value was calculated using (3.6). The surrogate model value, new coarse model design value and the unchanged extracted parameter value are summarised in Table 3.2. The new design stub length L_2 value of $(10.679 - 0.098)$ mm was used to evaluate the CST fine model. The S_{21} simulation response with this new stub length value is shown in Fig. 3.6

From Fig. 3.6, a nearly accurate and optimised microstrip bandstop filter design with a centre frequency of 4.996 GHz was realised in one space mapping iteration step. Therefore, it took only one iteration step involving evaluation

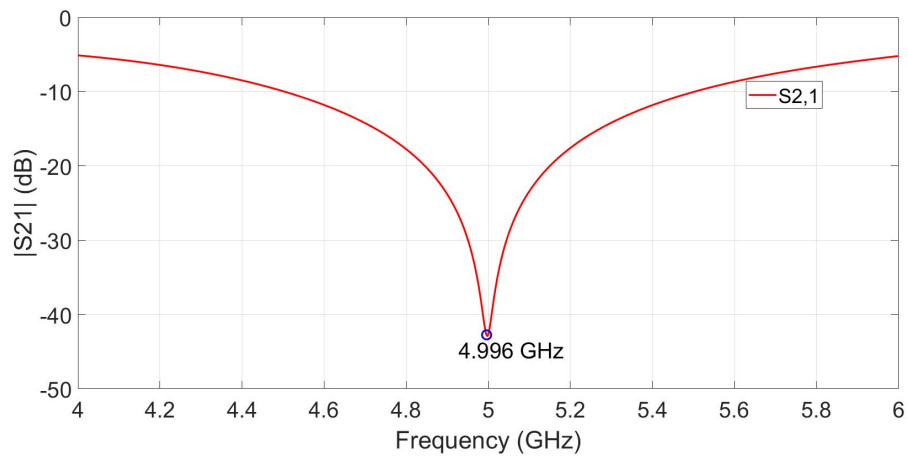


Figure 3.6: CST $|S_{21}|$ fine model response curve

of the fine model twice, to get an almost optimum microstrip bandstop filter for the stated design specification.

Chapter 4

Optimisation of Gap Waveguide Components through Space Mapping

4.1 Introduction

As already explained in Chapter 3, direct optimisation of microwave components using full wave EM microwave simulators is usually a time-consuming procedure. This procedure can be simplified by use of space mapping. Space mapping use the knowledge and properties of the simple, computationally cheap but less accurate coarse model for the bulk of the optimisation process. The computationally expensive fine model is only used to supply data for the alignment of the coarse model response to get a surrogate model which is a better representation of the actual fine model. For application of space mapping to optimise gap waveguide fine models, one should find coarse models which have similar physical attributes and properties as the gap waveguide fine model structures.

This chapter will analyse the approximate coarse models for both ridge and groove gap waveguides. Using the identified suitable ridge gap waveguide coarse models, space mapping will then be used for optimisation of the 3-dB ridge gap waveguide power divider and hybrid coupler. Coarse models should be simple and easy to analyse in a circuit environment and as such the use of a transmission line for modelling narrow band ridge and groove gap waveguide coupled resonator bandpass filters will be explored in Chapter 5.

4.1.1 Resemblance Between Stripline and Ridge Gap Waveguide

A stripline consists of an upper plate and a bottom ground plate. The space between the two plates is filled with either vacuum or dielectric material. In between the plates there is a central embedded strip conductor. The main propagating mode in a stripline is TEM. This mode propagates along the strip in the dielectric or vacuum gap between the strip and PEC plates. The diagram of ideal stripline and the wave propagation is shown in Fig. 4.1.

The propagating mode in the ridge gap waveguide stopband is TEM-like mode. As already discussed in Chapter 2, this mode propagates along the ridge in vacuum gap between the ridge and upper PEC plate. There is also no propagation in the dielectric region on either side of the middle embedded strip in the stripline. This resembles a perfect magnetic conductor (PMC) with a perfect electric conductor (PEC) plate above in a ridge gap waveguide. From the physical resemblance and similar propagation characteristics, a stripline will be used to model a ridge gap waveguide. However, there are limitations in using the stripline model and these will be discussed later.

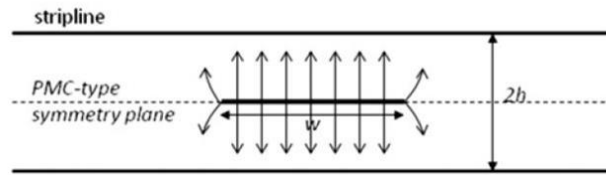


Figure 4.1: Ideal stripline and TEM propagation mode
[18]

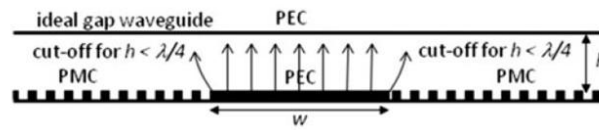


Figure 4.2: Half stripline
[18]

Stripline has a symmetry plane about the PMC plane as shown in Fig. 4.1. When compared to ridge gap waveguide, the stripline looks like two ridge gap waveguides back to back mirrored in the PMC symmetry plane. From the image theory, half of a stripline is needed to fully characterize a ridge gap waveguide. Figure 4.2 represents a half stripline which is a complete model of a ridge gap waveguide [18]. Therefore half the stripline will be used to coarse

model the ridge gap waveguide.

The characteristic impedance is an important parameter in the design of ridge gap waveguide components. Using the stripline model, the stripline characteristic impedance formula can be used for approximating the otherwise difficult to evaluate characteristic impedance of the ridge gap waveguide. As already stated one upper half of the stripline will be used to model the ridge gap waveguide. Generally the resistance or impedance of an electrical component is inversely proportional to surface area. Also in the telegrapher equations, the surface area is proportional to capacitance which is inversely proportional to line impedance. Therefore half the stripline area implies that the impedance of the ridge gap waveguide will be double that of the stripline. The relationship between two characteristic impedances can be mathematically stated as:

$$Z_{\text{gap waveguide}} \approx 2Z_{\text{stripline}}. \quad (4.1)$$

The characteristic impedance of a stripline is [24]:

$$Z_{\text{stripline}} = \frac{30\pi}{\sqrt{\epsilon_r}} * \frac{b}{w_e + 0.441b} \quad (4.2)$$

where w_e is the effective width of the centre strip. A strip thickness of zero is assumed in this stripline formula which is quoted as being accurate to about 1 % of the exact results [24]. The effective width of the stripline is given:

$$\frac{w_e}{b} = \frac{w}{b} - \begin{cases} 0 & \text{for } \frac{w}{b} > 0.35 \\ (0.35 - \frac{w}{b}) & \text{for } \frac{w}{b} < 0.35 \end{cases} \quad (4.3)$$

where w is the actual conductor width. When the characteristic impedance Z_o is given, the width of the strip w or substrate height b can be calculated using:

$$\frac{w}{b} = \begin{cases} x & \text{for } \sqrt{\epsilon_r} Z_o < 120 \\ (0.85 - \sqrt{0.6 - x}) & \text{for } \sqrt{\epsilon_r} Z_o > 120 \end{cases} \quad (4.4)$$

where

$$x = \frac{30\pi}{\sqrt{\epsilon_r} Z_o} - 0.441. \quad (4.5)$$

Using a stripline to model a ridge gap waveguide only holds for small vacuum gap height to ridge width ratio in the ridge gap waveguide. As will be

discussed in the next section, when the vacuum gap height h between ridge and upper plate is increased the propagating TEM-like mode moves away from the free space propagation constant line in the stopband region. This results in the increase of the wavelength of the propagating mode in the ridge gap waveguide. For large vacuum gap height to ridge width ratios, the ridge gap structure becomes dispersive. This dispersive nature of the ridge gap waveguide limits our stripline model approximation.

4.1.2 Resemblance Between Gap Waveguides and Ridge/Hollow Rectangular Waveguides

The waveguide ports in the available EM microwave solvers like CST work well for conventional ridge/rectangular waveguides. However there is a challenge in defining waveguide ports for simulation of gap waveguide structures. Therefore proper waveguide port dimensions and configuration are needed for simulation of gap waveguide structures.

The end views of ridge/groove gap waveguide and ridged/rectangular waveguides are shown in Fig. 4.3. If two vertical PEC plates of height $d + h$ are placed at a distance p on the either side of ridge edges, a ridged rectangular waveguide is reproduced. Also if two vertical PEC plates of height $d + h$ are placed at the first pin rows on either side of the groove, hollow rectangular waveguide is reproduced. The reproduced ridged rectangular waveguide and hollow rectangular waveguides end views show some geometrical resemblance between the two types of waveguides as shown in Figs. 4.3 (a) and (b).

The dispersion graphs of the ridge gap waveguide [25] and its corresponding ridged rectangular waveguide were calculated using the eigenmode solver in CST and plotted in Figs. 4.4, 4.5, 4.6 and 4.7. The four plots were done for 4 different vacuum gap heights h between the ridge upper surface and the PEC plate above it. The simulated values of vacuum gap heights h are 0.5 mm, 1 mm, 2 mm and 3 mm. The dimensions of the two types of waveguides used in the calculation and plot of the dispersion diagrams are shown in Fig. 4.3 (a).

From the plots, the propagation constant graphs of the ridge gap waveguide and that of the corresponding ridged rectangular waveguide were similar in the stopband region. The dispersion graphs of the two waveguides closely followed that of free space (light line) in the stopband. The dispersion plots showed the equivalence of the two waveguides in the stopband.

As the gap height values of h were increased from 0.5 to 3 mm, the plots of Figs. 4.4 - 4.7 show that the dispersion graphs of the two waveguide move

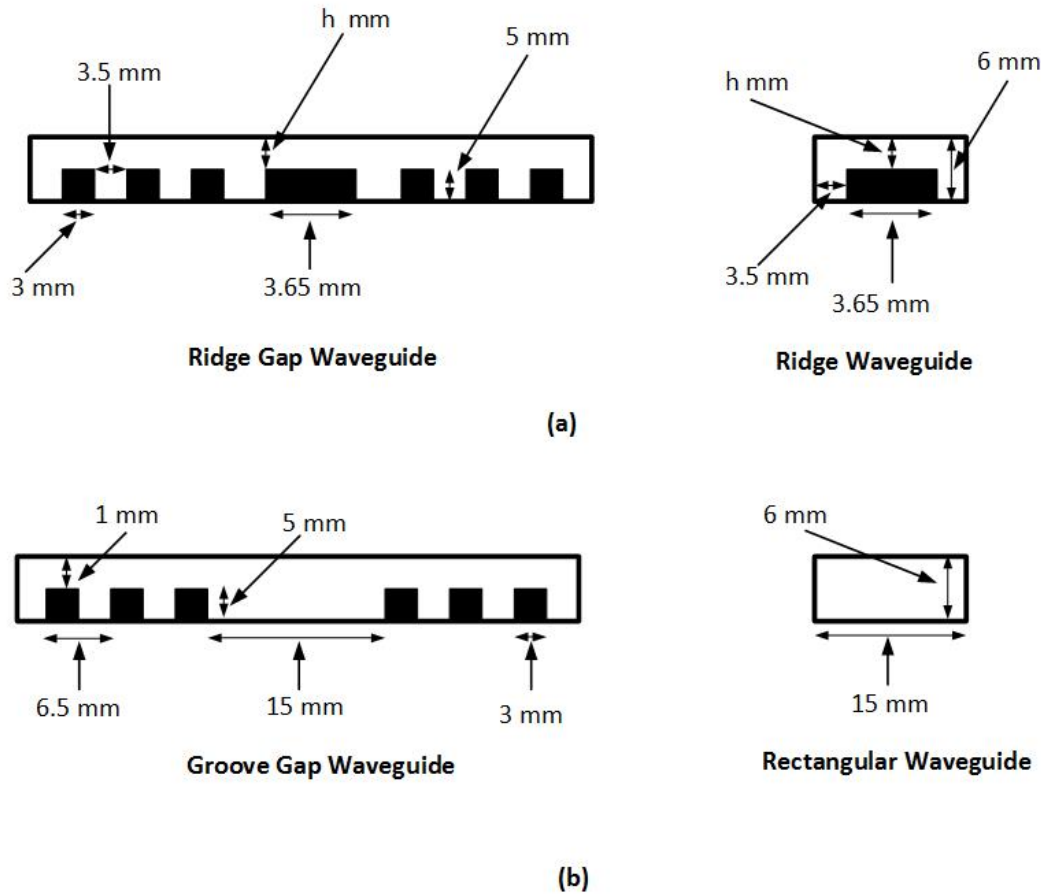


Figure 4.3: Gap waveguides and their equivalent rectangular waveguides

away from that of free space (light line). This shows the dispersive nature of the ridge gap waveguide structures for large vacuum gap height to width ratio which puts a limitation on the use of vacuum TEM stripline to model ridge gap waveguide.

The dispersion plots were also done for the groove gap waveguide and its corresponding hollow rectangular waveguide. The dimensions used in the plots are shown in Fig. 4.3 (b). The dispersion graph plots of the two waveguides are shown in Fig. 4.8. The dispersion curves were also similar for both waveguides in the stopband. This also shows the equivalence of the groove gap waveguide and hollow rectangular waveguide in the stopband.

Simulations were done [25] using the circuit arrangement of Fig. 4.9 (a) and Fig. 4.9 (b) for groove and ridge gap waveguides best waveguide port location, dimensions and configuration. The waveguide port location, dimensions and configuration for optimum waveguide ports for the groove and ridge gap waveguides were arrived at after varying the parameters in

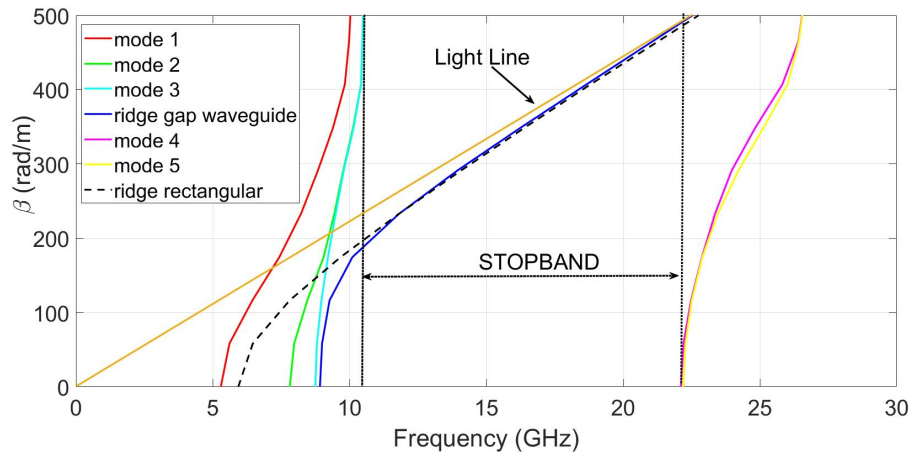


Figure 4.4: Ridge gap/ridged rectangular waveguides dispersion graphs for $h = 0.5$

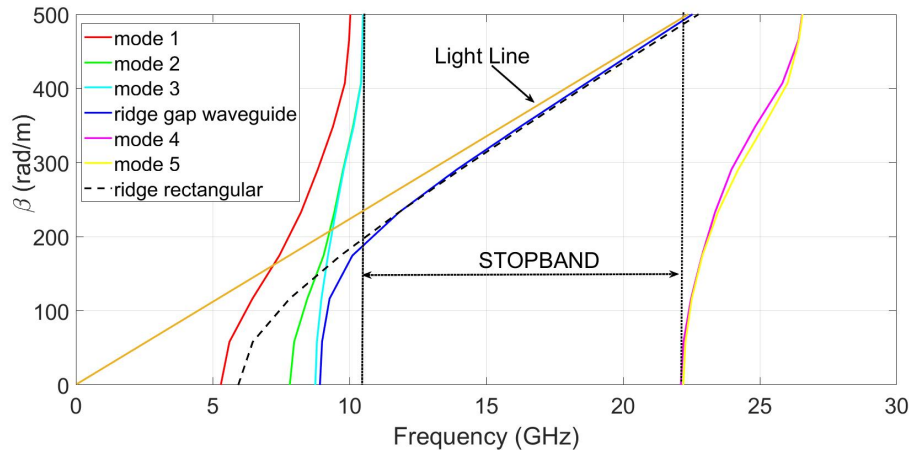


Figure 4.5: Ridge gap/ridged rectangular waveguides dispersion graphs for $h = 1$

Fig. 4.10 for minimum reflection coefficient S_{11} and maximum transmission coefficient S_{21} .

The parameter p is the inter pin distance, k_2 is distance from ridge wall to the first pin wall or waveguide port edge which is equal to p in this case, k_1 is the distance from the last pin edge end to bottom or upper plate ends as shown in the Fig. 4.10 and it was found to be $\frac{p}{2}$. This waveguide port location, configuration and dimensions was found to give best results for both groove and ridge gap waveguides.

In summary, the equivalence between ridge/groove gap waveguides and ridge/rectangular waveguides was established through plots of dispersion graphs. The study of waveguide ports dimensions and configuration [25] has

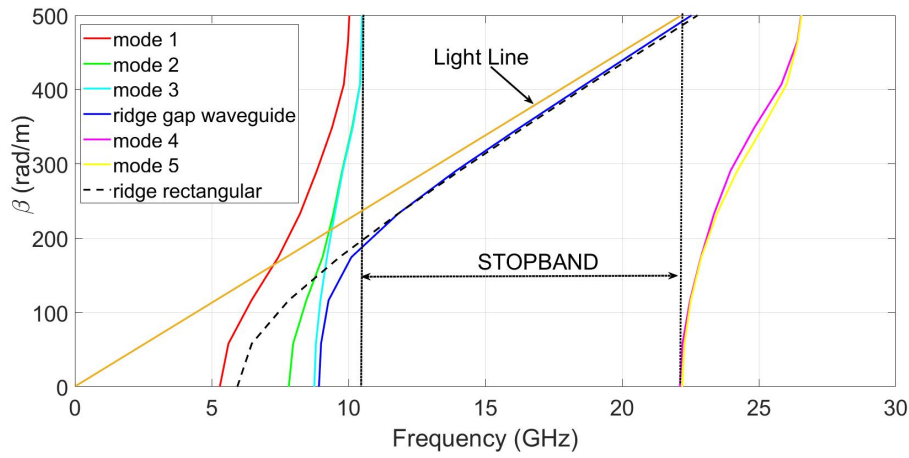


Figure 4.6: Ridge gap/ridged rectangular waveguides dispersion graphs for $h = 2$

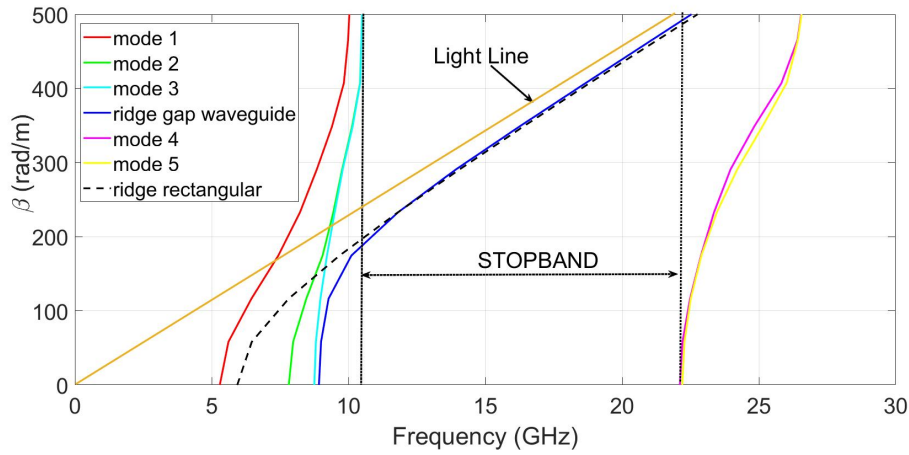


Figure 4.7: Ridge gap/ridged rectangular waveguides dispersion graphs for $h = 3$

shown the best waveguide ports dimensions and configuration for simulation of gap waveguide structures. Using their geometrical resemblance, the ridged and hollow rectangular waveguide geometry can be used as a starting geometry in the design of ridge and groove gap waveguide components respectively. The already known ridged rectangular waveguide formulas can be used to calculate the corresponding parameters of the ridge gap waveguide because of their equivalence.

The dispersion plots of the ridge gap waveguide also showed the limitation of using the stripline model for large vacuum gap height to ridge width ratios in the ridge gap waveguide. The propagation constant of the ridge gap waveguide TEM mode decreased as the ratio increased. This meant that the wavelength of the ridge gap waveguide TEM mode increased. However, we choose and use

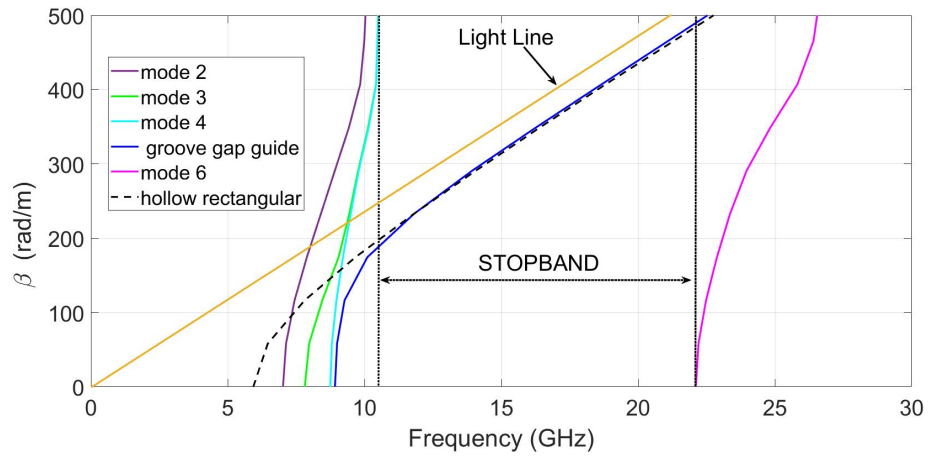


Figure 4.8: Groove/hollow waveguide dispersion graphs

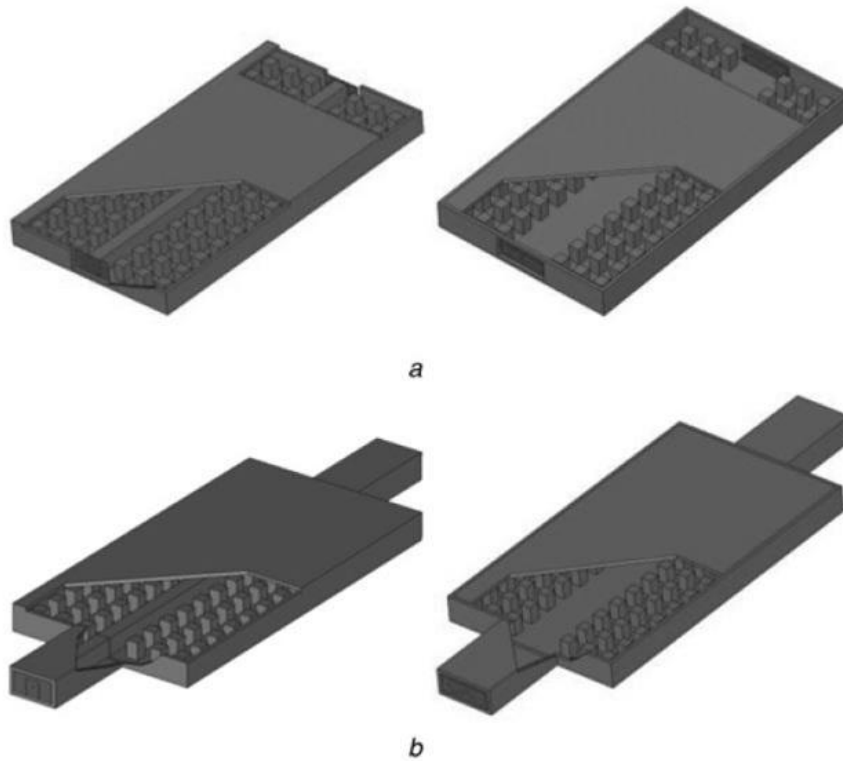
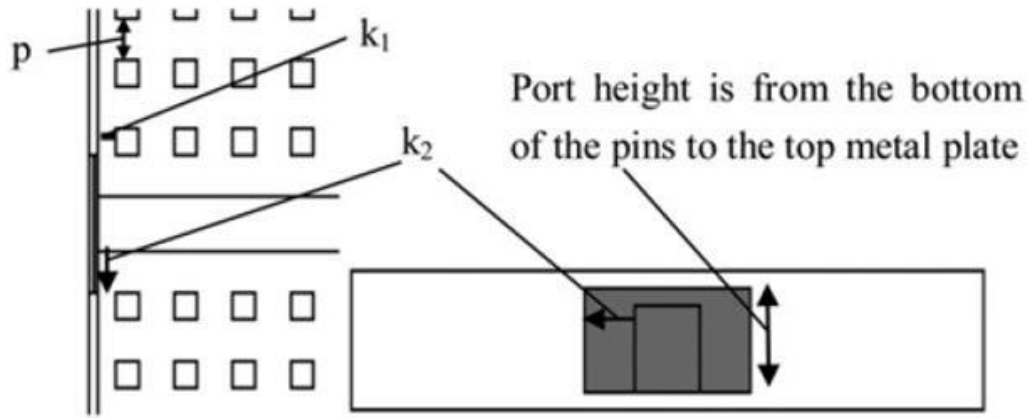


Figure 4.9: (a) Groove waveguide port arrangement and (b) ridge waveguide port arrangement

[18]

the shorter wavelength vacuum TEM stripline to model a ridge gap waveguide TEM line which has a longer wavelength. We correct or reduce the error

**Figure 4.10:** Best waveguide port configuration and dimensions

[18]

between the two lines by tuning the length of the stripline model.

4.2 T-Junction Power Divider

A T-junction power divider is a component used for dividing power of a given signal. This three port device has one input and two outputs. The power division between the two outputs is determined by the ratios of the output line impedances. These output line impedances can be selected to achieve a wide range of desired power division ratios. For a 3-dB power division the two output line impedances should have a ratio of 1:1. This three port component can be implemented by almost all the transmission lines. This three port component can be generally characterised by 3 by 3 matrix with nine elements as shown in equation below:

$$[S] = \begin{bmatrix} S_{11} & S_{12} & S_{13} \\ S_{21} & S_{22} & S_{23} \\ S_{31} & S_{32} & S_{33} \end{bmatrix}. \quad (4.6)$$

If the ports are matched, and the structure is reciprocal, the above matrix reduces to:

$$[S] = \begin{bmatrix} 0 & S_{12} & S_{13} \\ S_{12} & 0 & S_{23} \\ S_{13} & S_{23} & 0 \end{bmatrix}. \quad (4.7)$$

The ridge 3-dB power divider used in this section is assumed to be lossless. The T-junction is a point of discontinuity and as such there will be

fringing fields and higher order modes [24] in the junction. This results in stored energy in the junction which is modelled by susceptance jB in Fig. 4.11.

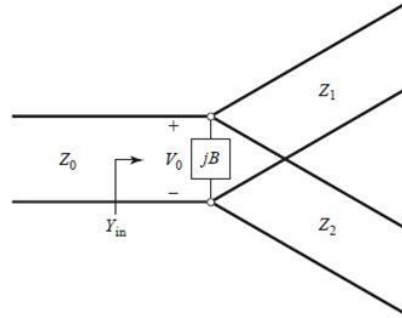


Figure 4.11: Transmission line model of a power divider
[24]

From Fig. 4.11 any of the three T-junction power divider impedance lines Z_0 , Z_1 and Z_2 can be used as an input port with output power being divided between the remaining two output ports. The effective load impedance of the feed port seen at the junction is the parallel impedance combination of the other two ports, if there are terminated in their characteristic impedances.

4.3 Optimisation of 3-dB Ridge Gap Waveguide T-Junction Power Divider Using Input Space Mapping

A waveguide power divider with a characteristic impedance of 50Ω in [4] was designed and optimised using space mapping. A 50Ω stripline was used to coarse model the ridge gap waveguide power divider. The stripline equations were used to calculate the ridge width of the ridge gap waveguide. The characteristic impedance formula of the ridged waveguide was used to calculate the vacuum gap height h of the ridge gap waveguide fine model.

As already stated in the previous section for a 50Ω power divider, any chosen input port in the T-power divider will be loaded by an effective load of two parallel 50Ω impedances of the other two ports. The effective load at the T-junction seen by the feed port will be thus be 25Ω . This implies that there will be a mismatch between 50Ω input port and the 25Ω effective load impedance seen at the junction. For this reason a quarter wave transformer

needs to be inserted between the $50\ \Omega$ input port and the $25\ \Omega$ T-junction load for matching. The characteristic impedance of the matching quarter wave transformer was calculated as follows:

$$Z_{\text{quarter wave}} = \sqrt{(50 * 25)} = 35.4\ \Omega. \quad (4.8)$$

The width of quarter wavelength line w_2 was calculated using (4.4) and (4.5) for a pre-selected stripline height of 2 mm and its value is 7.12 mm.

The width of the stripline coarse model w_1 was calculated using (4.4) and (4.5) for a pre-selected stripline height of 2 mm and a $50\ \Omega$ impedance. The calculated width value is 2.87 mm. The calculated strip width of the stripline coarse model was also used as the width of the ridge gap waveguide fine model. There were two options for the coarse model. The first option was to use the same width and height for both coarse and fine models and a $25\ \Omega$ impedance from (4.1). The second option was to use similar widths and impedances of $50\ \Omega$ for both coarse and fine models and have the height of the stripline as a variable for the correct impedance. Both options were tried. The first option did not work, it gave a totally wrong coarse model response. The second option worked well giving the expected response.

In the example [4], it was not clearly stated by the author which of the two options stated above works when using a stripline to model a ridge gap waveguide. Generally, in using the stripline to model a ridge gap waveguide, the widths and impedances of the two models should be the same and the height should be the variable to get the right impedance.

The schematic diagram of the stripline model is shown in Fig. 4.12 with the matching transformer length shown as L_2 and its width as w_2 . The length of the stripline is L_1 and its width is w_1 . The length of the transformer L_2 and L_1 were chosen as design parameters because of reasons stated in subsection 4.1.2. The power divider was designed for a centre frequency of 15 GHz. The calculated quarter wavelength at this frequency is 5 mm. This length of the lines was scaled to $\frac{3\lambda}{4}$ which is 15 mm to accommodate two rows of pins in the fine model. The coarse model was simulated using MWO. The optimum coarse model response is shown in Fig. 4.13.

The 3-D fine model of the power divider is shown in Fig. 4.14. The calculated stripline width of the coarse model was used as the ridge width as well in the fine model. From the equivalence of ridged rectangular waveguide and ridge gap waveguide discussed in the above subsection 4.1.2, the characteristic impedance formula of the former was used to approximate the ridge gap waveguide vacuum height gap h for a characteristic impedance of

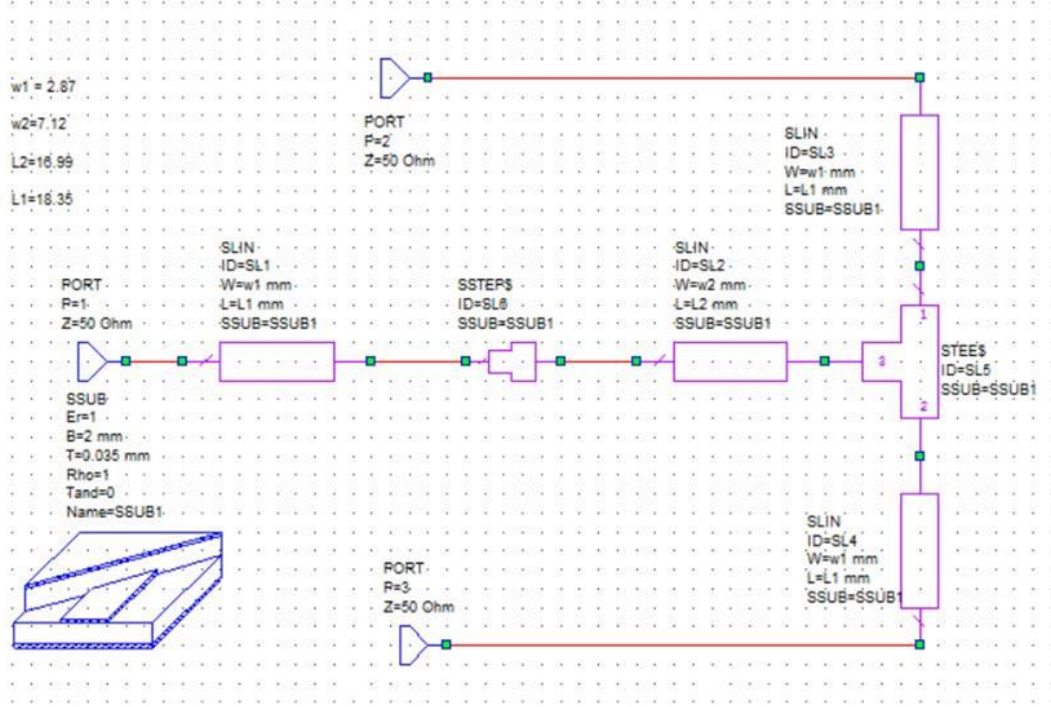


Figure 4.12: MWO stripline coarse model schematic

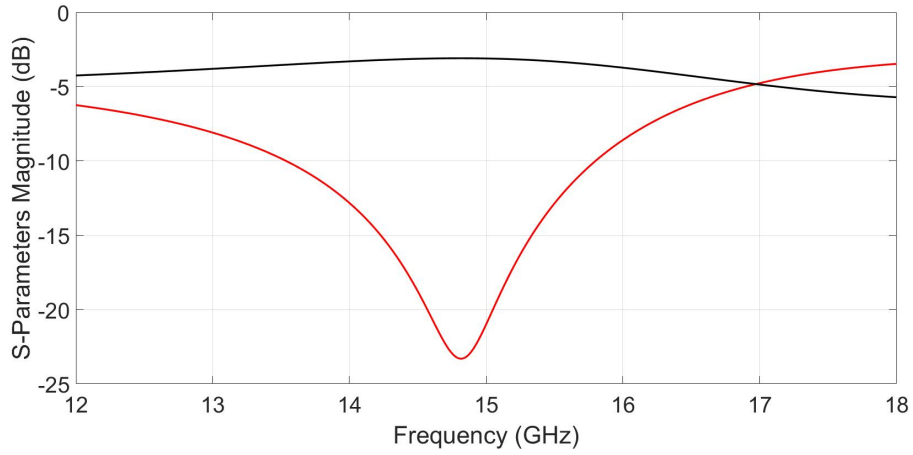
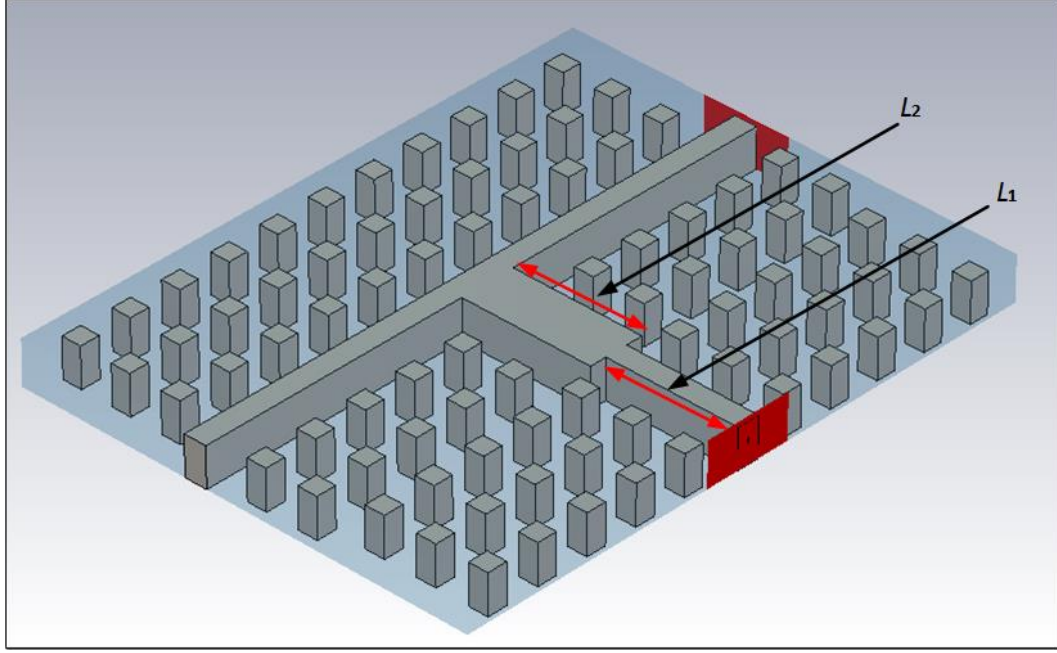


Figure 4.13: MWO stripline coarse model response

50 Ω [26]. The characteristic impedance formula is:

$$Z_0 = Z_{0\infty} [1 - (\lambda/\lambda_{cr})^2]^{-1/2} \quad (4.9)$$

where $Z_{0\infty}$ is the characteristic impedance for infinity frequency and is given by:

**Figure 4.14:** CST 3-D fine model diagram

$$Z_{0\infty} = \frac{120\pi^2 (b/\lambda_{cr})}{\frac{b}{d} \sin \pi \frac{s}{b} \frac{b}{\lambda_{cr}} + \left[\frac{B_0}{Y_0} + \tan \frac{\pi}{2} \frac{b}{\lambda_{cr}} \left(\frac{a-s}{b} \right) \right] \cos \pi \frac{s}{b} \frac{b}{\lambda_{cr}}} \quad (4.10)$$

and λ_{cr} is given by:

$$\begin{aligned} \frac{b}{\lambda_{cr}} = & \frac{b}{2(a-s)} \left[1 + \frac{4}{\pi} \left(1 + 0.2 \sqrt{\frac{b}{a-s}} \right) \frac{b}{a-s} \ln \csc \frac{\pi}{2} \frac{d}{b} \right. \\ & \left. + \left(2.45 + 0.2 \frac{s}{a} \right) \frac{sb}{d(a-s)} \right]^{-1/2} \end{aligned} \quad (4.11)$$

where λ_{cr} is the waveguide cut-off wavelength. The cross sectional dimensions and parameters a , b , d and s of both double and single ridge waveguides are shown in Figs. 4.15 (a) and (b). It should be noted that (4.10) and (4.11) were derived using double ridged waveguide with b and d values being twice those of a single ridged waveguide. In this example a single ridged waveguide was used for the power divider. Hence to get the correct characteristic impedance formulas, the double ridged waveguide formulas (4.10) and (4.11) were divided by 2.

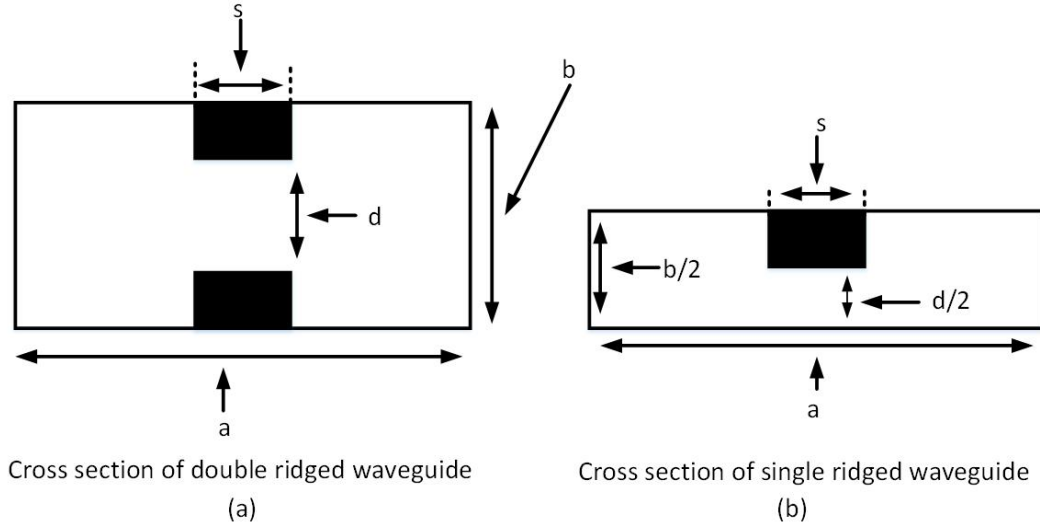


Figure 4.15: Cross sectional dimensions of double and single ridged waveguides

The above equations were implemented in MATLAB to calculate the ridge gap height h for an impedance of 50Ω . The calculated value of h was 0.66 mm . This vacuum gap height value was used in the ridge gap waveguide fine model. The 3-dB ridge gap waveguide power divider was optimised using an in-house input space mapping code. The design goal type of the code is $|S_{11}|$ and the design specification is given as a $[14 - 15] \text{ GHz}$ frequency range for a level of -15 dB . The results of the first iteration in which the fine model was evaluated using the calculated parameter values did not meet the design specifications and is shown in Fig. 4.16.

Using the design parameters, the stripline coarse model response was mapped and aligned to the fine model response which resulted in an aligned surrogate model. The aligned surrogate model was optimised to get new design parameter values in the second iteration for evaluation of the fine model. The evaluated fine model response in the second iteration using the new design parameter values is shown in Fig. 4.17. The fine model response for the second iteration was within the acceptable design specification accuracy range. The design specification was thus met in just two space mapping iterations of evaluating the fine model.

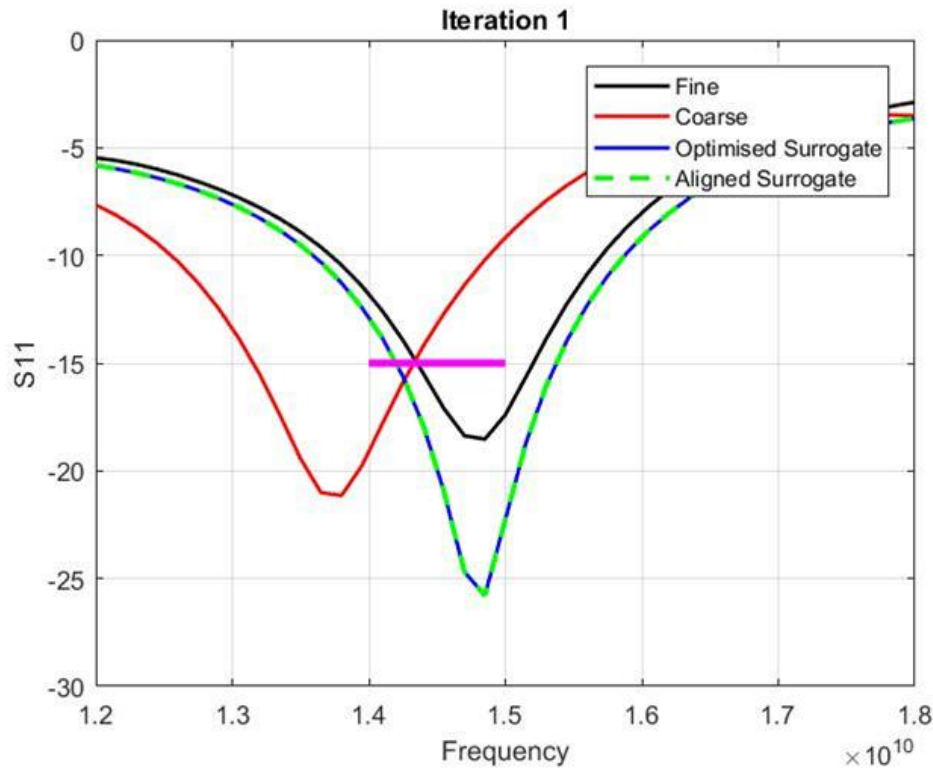


Figure 4.16: CST fine model first iteration

4.4 Design and Optimisation of a 3-dB Ridge Gap Waveguide Hybrid Coupler Using Input Space Mapping

A 3-dB ridge gap waveguide hybrid coupler was designed and optimised using input space mapping. The input space mapping procedure and steps have already been discussed in Chapter 3. In this design example the space mapping steps were manually done as the in-house input space mapping code did not yet have the ability to simultaneously handle multiple design responses of interest.

A 3-dB quadrature hybrid coupler is a four port network with output power being equally divided between through and coupled ports. The port on the same side as the input port is the isolated port and ideally it has no power coupled to it. The coupled and through ports are on the opposite side of the input port. The output of the through and coupled ports have a phase difference of 90° . The schematic diagram of a hybrid coupler with typical port configuration is shown in Fig. 4.18. Two sets of quarter wavelength lines are used in the coupler and these are shown in the schematic as series and parallel. The characteristic impedance of the series quarter wavelength

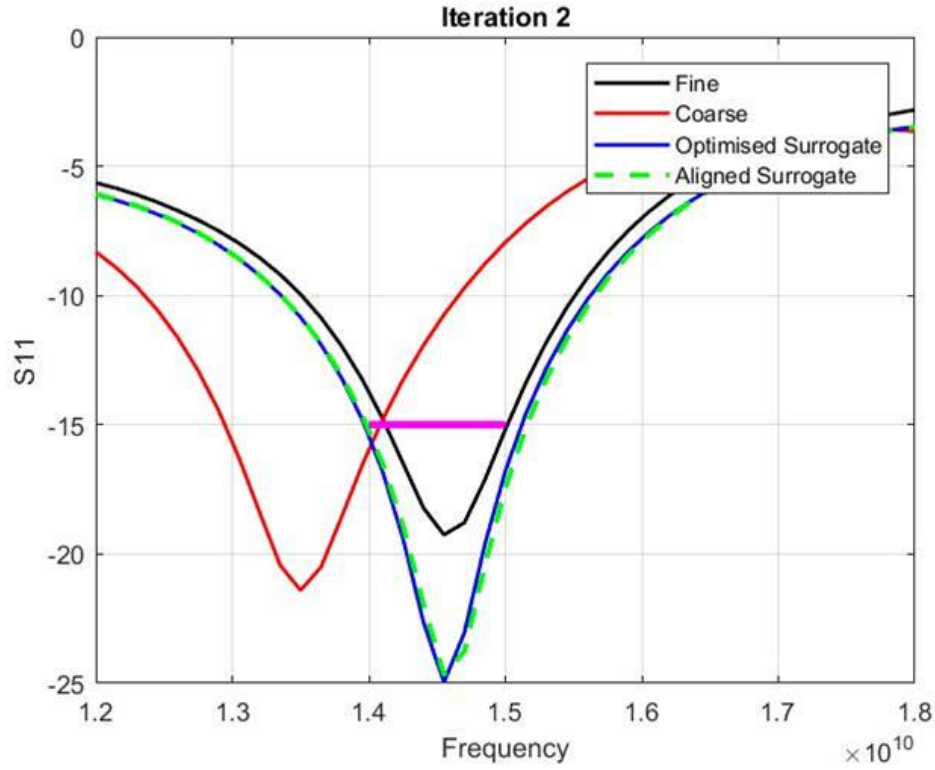


Figure 4.17: CST fine model second iteration

lines is $Z_o/\sqrt{2}$ where Z_o is the characteristic impedance of the coupler. The characteristic impedance of the parallel quarter wavelength lines is Z_o . It should be noted that the hybrid coupler is symmetric and as such any port can be used as an input port.

The operation of the hybrid can be analysed using even-odd mode configuration analysis. The hybrid is fully characterised by a 4 by 4 symmetrical matrix [24] given by:

$$[S] = \frac{-1}{\sqrt{2}} \begin{bmatrix} 0 & j & 1 & 0 \\ j & 0 & 0 & 1 \\ 1 & 0 & 0 & j \\ 0 & 1 & j & 0 \end{bmatrix}. \quad (4.12)$$

The above matrix show all the possible output lines power ratios for any of the 4 ports used as input. Each column in the matrix corresponds to the 4 possible input ports. For example column 3 of the matrix is a summary of output power ratios when port 3 is used as an input port. With matched

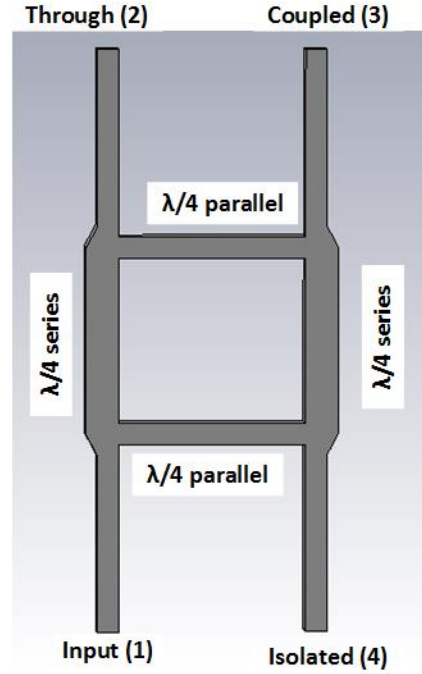


Figure 4.18: Hybrid coupler schematic diagram

port 3 as the input port, the power coupled to port 2 is zero, half power is coupled to port 1 with a phase shift of -180° from port 3 to 1 and half power is coupled to port 4 with a phase shift of -90° from port 3 to 4. The power phase difference between the through and coupled ports is 90° . A 3-dB hybrid coupler was designed using input space mapping for centre frequency of 15 GHz with a characteristic impedance of $50\ \Omega$.

The stripline coarse model was used in this example. The stripline coarse model dimensions used are similar to those used in the previous example. Like in the previous example, the initial length of quarter wavelength lines is 5 mm and this was scaled up to $\frac{3\lambda}{4}$ so as to accommodate enough pin rows in the central region of coupler fine model. MWO was used to simulate the stripline model. The schematic diagram of the stripline coarse model is shown in Fig. 4.19.

The design parameters are shown in Fig. 4.19. There are series $35.4\ \Omega$ quarter wavelength transformers line lengths shown as L_2 , a $50\ \Omega$ quarter wavelength parallel line lengths shown as L_1 and their width shown as w_1 . The four terminal lines had their width and lengths fixed for matching with $50\ \Omega$ feed ports. The widths of the quarter wavelength transformers were calculated using (4.4) and (4.5). The calculated width of the $35.4\ \Omega$ line which is 4.42 mm, could not be used as a design variable because of the limited

| Design Variables | Surrogate (R_s) | Coarse (R_c) | Parameter C |
|------------------|---------------------|------------------|---------------|
| W_1 | 0.39 | 2.87 | -2.48 |
| L_1 | 13.24 | 15 | -2.76 |
| L_2 | 14.11 | 15 | -0.89 |

Table 4.1: Alignment step

middle region pin space in the fine model. Hence this width was fixed. The three design variables are L_1 , L_2 and w_1 .

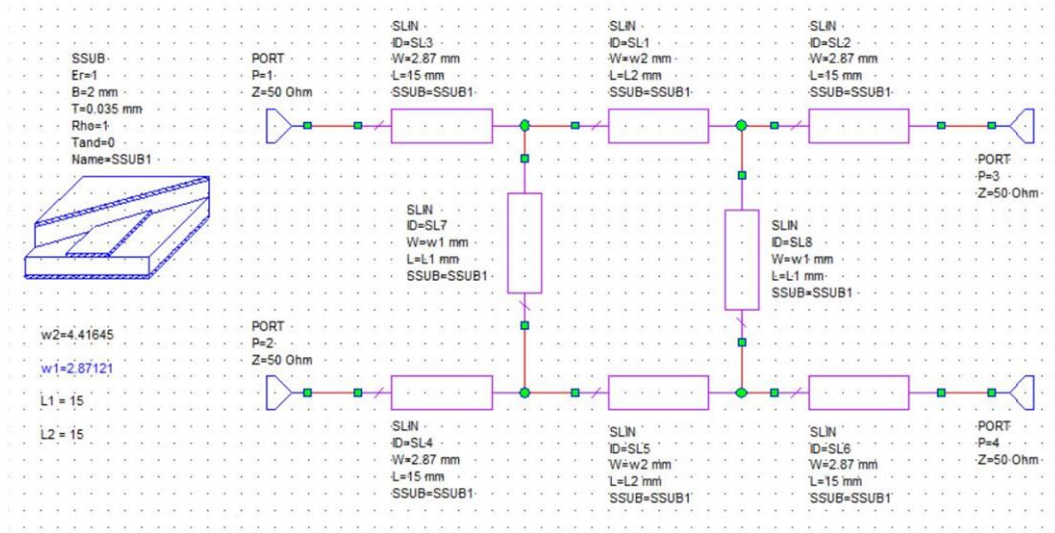


Figure 4.19: MWO coupler coarse model schematic diagram

The stripline coarse model was evaluated using the initial calculated parameter values and its optimum S-parameter response is shown Fig. 4.20. The fine model was simulated in CST. The CST 3-D fine model and the design parameters are shown in Fig. 4.21. The dimensions of the fine model are pin height d of 5 mm, vacuum gap height h of 0.66 mm, pin width a of 2.5 mm and the distance between the pins p of 4 mm. The hybrid coupler fine model was evaluated using the initial calculated parameter values and its initial S-parameter response is shown in Fig. 4.22.

The fine model response is off the design specification as seen in Fig. 4.22. The next step was to align the coarse and fine models. The three design parameters were used to align the coarse and fine models. This alignment step is summarised in Table 4.1. The coarse model, fine model and the aligned surrogate model are shown in Fig. 4.23.

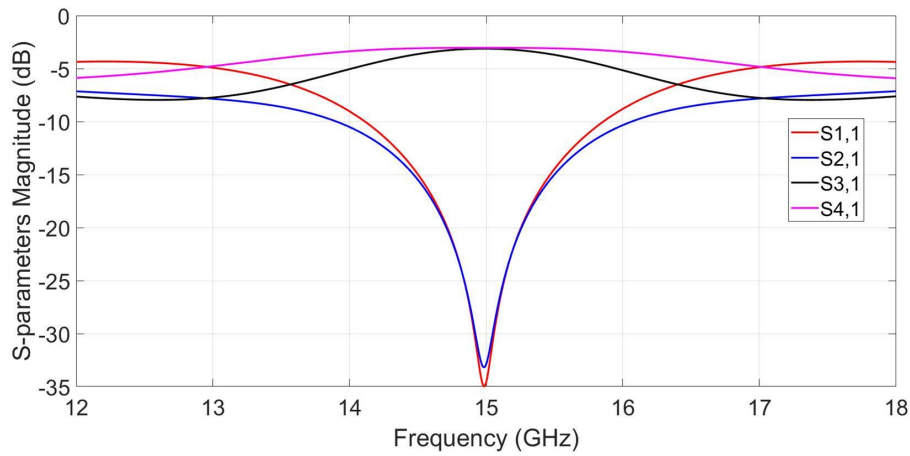


Figure 4.20: MWO coupler coarse model S-parameters

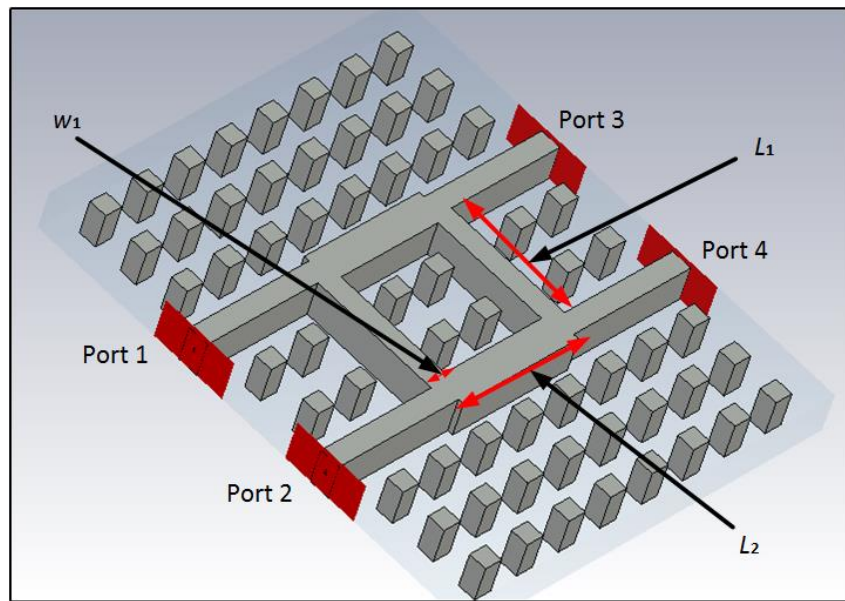


Figure 4.21: CST coupler 3-D fine model

The resultant aligned surrogate model was optimised for new coarse model design values. This optimisation step was redundant in this example because by design the coarse model was optimum. The new design values from (3.6) are shown in Table 4.2. These were used to evaluate the hybrid coupler fine model. The response of the fine model is shown in Fig. 4.24. With one manual iteration of input space mapping involving evaluation of fine model 2 times, a nearly optimum hybrid coupler was designed for 15 GHz centre frequency.

The results of the 3-dB ridge gap waveguide power divider and hybrid

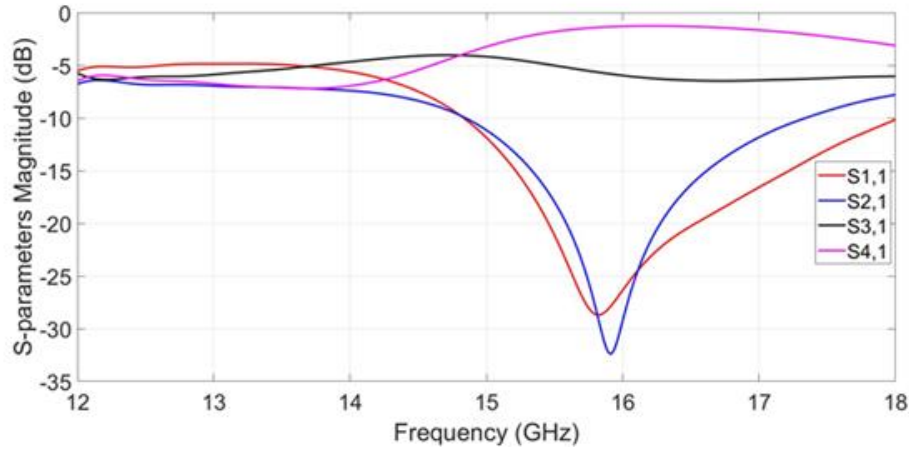


Figure 4.22: CST coupler fine model initial S-parameters

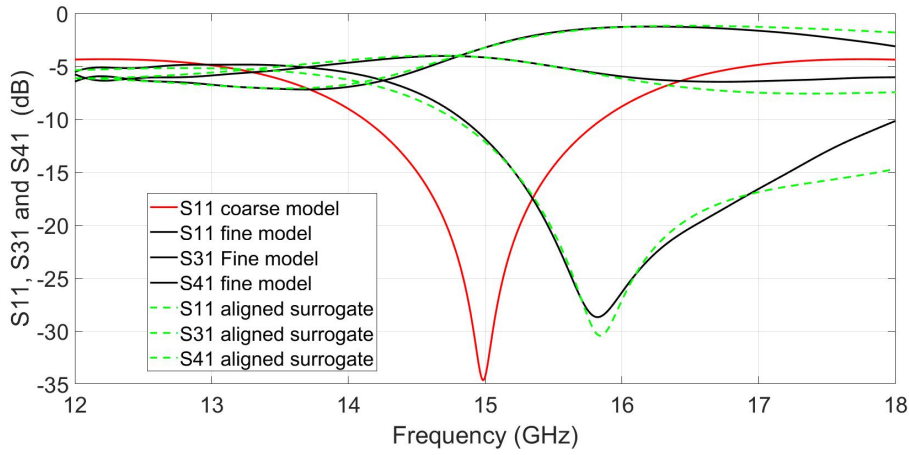


Figure 4.23: Alignment step and the aligned models

| Design Variables | Surrogate (R_s) | New values (R_c) | Parameters C |
|------------------|---------------------|----------------------|----------------|
| W_2 | 2.87 | 5.35 | -2.48 |
| L_1 | 15 | 17.76 | -2.76 |
| L_2 | 15 | 15.89 | -0.89 |

Table 4.2: New coarse model design values

coupler generally show that using the calculated design parameter values in design, in most cases do not give an optimum design. The design parameters need to be tuned or optimised to meet the design specifications. The examples also showed the efficiency of the space mapping optimisation technique.

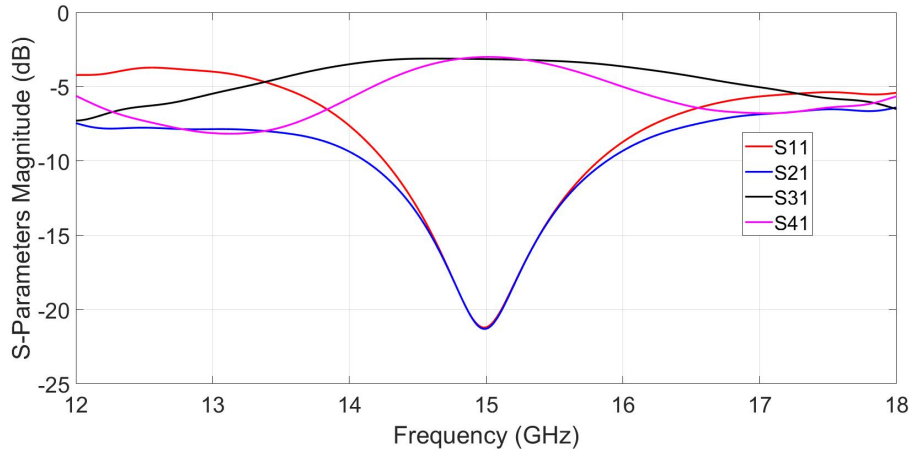


Figure 4.24: Second iteration and the fine model S-parameters response

From equivalence established between ridged rectangular waveguide and ridge gap waveguide in the stopband in subsection 4.1.2, the already known ridged rectangular waveguide characteristic impedance formula was used to calculate the vacuum gap height of the ridge gap waveguide. Generally, the geometry of the ridged/rectangular waveguides can be used as starting geometry of ridge/groove gap waveguides components because of their resemblance. The relevant stripline formulas can be used to approximate the characteristic impedance and width of the ridge gap waveguide.

The dispersion plots of the ridge gap waveguide in subsection 4.1.2, showed the limitation of using the stripline model for large vacuum gap height to ridge width ratios in the ridge gap waveguide. From the plots, the propagation constant of the ridge gap waveguide TEM mode decreased as the ratio increased. This implied that the wavelength of the ridge gap waveguide TEM mode increased. However, we choose and use the shorter wavelength vacuum TEM stripline to model a ridge gap waveguide TEM line which has a longer wavelength. We correct or reduce the error between the two lines by tuning the length of the stripline model. Though the stripline model in two examples converged, the results were not very accurate. The next Chapter will explore the use of a simple transmission line to model narrow band ridge and groove gap waveguides coupled resonator bandpass filters.

Chapter 5

Optimisation of Microwave Gap Waveguide Bandpass Filters Using Space Mapping

5.1 Bandpass Filter Basics

A bandpass filter is a two port electronic circuit that allows transmission of a given band of frequencies but rejects the frequencies outside the passband. Bandpass filters are mostly fabricated using lumped elements (resistor, inductor and capacitor), distributed elements (transmission lines) and waveguides. The flatness of the transmission function response in the passband and the sharpness of its transition from passband frequency edge to stopband frequency edge, called selectivity factor, is one of the filter design considerations. Generally transmission ripples are not desirable in the passband, but lower values of less than 1 dB are acceptable in most bandpass filter applications. In some applications, the sharpness of the transition cut-off response from passband frequency edge to stopband frequency edge is more important than its flatness in the passband and this depends on the selectivity factor of the filter.

The selectivity factor is the ratio of stopband edge frequency (ω_s) to passband edge frequency (ω_p) which is a measure of sharpness, steepness or roll-off between the two frequencies. The two frequency edges of a bandpass filter ω_p and ω_s and the transition band are shown in Fig. 5.1(a). Ideally there should be zero transition band between the two cut-off frequency edges or selectivity factor of 1. Increasing selectivity factor or improving the sharpness of the cut-off response results in ripples in the transmission function response in the passband. Filters whose transmission function have equal ripples in the passband and monotonically decreasing in the stopband are called Chebyshev filters. The bandpass filter designs in this chapter are based on Chebyshev

type I (first kind) filter whose transmission function has ripples only in the passband but none in the stopband. Typical Chebyshev bandpass filter transmission function responses for an even ($N = 4$) and odd ($N = 5$) order Chebyshev type I filter are shown in Fig. 5.1.

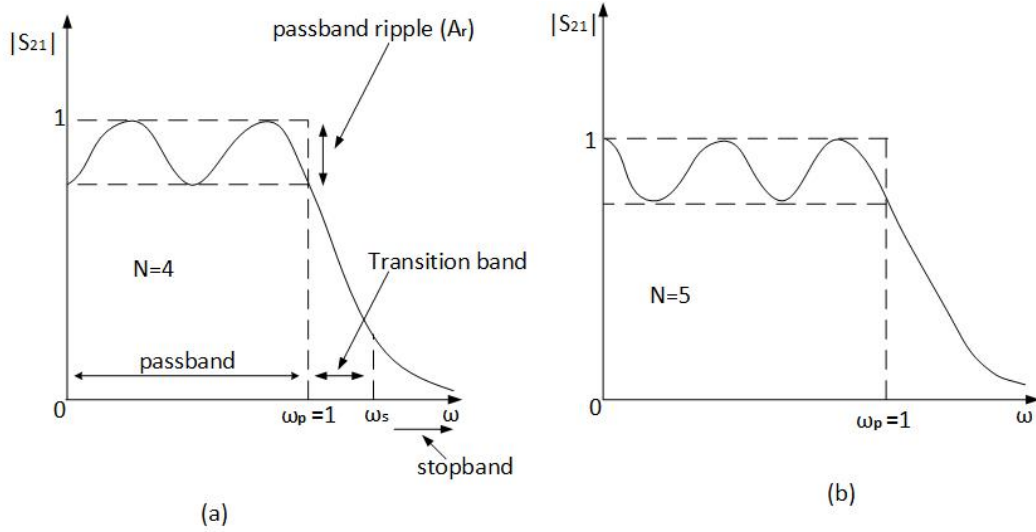


Figure 5.1: Chebyshev transmission function response

5.1.1 Chebyshev Bandpass Filter Transfer Function

As already stated, a Chebyshev type I bandpass filter is characterized by a transmission function with equal ripples in the passband and monotonically decreasing in the stopband with no ripples in the stopband. The order of the filter (number of poles) is indicated by the number of transmission function maxima and minima (poles) in the passband. For a Chebyshev type I, the transmission zeros are at $\omega = \infty$, hence it is called an all pole filter. The transfer function of an N^{th} order Chebyshev filter with its magnitude squared is:

$$|S_{21}(j\omega)|^2 = \frac{1}{1 + \epsilon^2 T_N^2(\omega)} \quad (5.1)$$

where $T_N(\omega)$ is the N^{th} Chebyshev polynomial defined in the following ranges as:

$$T_N(\omega) = \cos(N \cos^{-1} \omega) \text{ for } |\omega| \leq 1$$

$$T_N(\omega) = \cosh(N \cosh^{-1} \omega) \text{ for } |\omega| > 1.$$

The magnitude of the transmission function at passband frequency edge $\omega = \omega_p$ is:

$$|S_{21}(j\omega)| = \frac{1}{\sqrt{1 + \epsilon^2}} \quad (5.2)$$

where ϵ is the ripple constant related to the specified bandpass ripple level (A_r) by:

$$A_r = 10 \log(1 + \epsilon^2). \quad (5.3)$$

Solving for ripple constant (ϵ) gives

$$\epsilon = \sqrt{10^{A_r/10} - 1}. \quad (5.4)$$

The Chebyshev polynomials may be generated recursively using:

$$T_0(\omega) = 1 \quad (5.5)$$

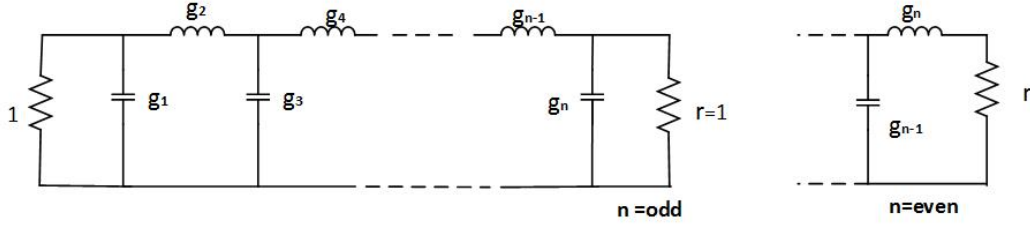
$$T_1(\omega) = \omega \quad (5.6)$$

$$T_{N+1}(\omega) = 2(\omega)T_N(\omega) - T_{N-1}(\omega). \quad (5.7)$$

5.1.2 Chebyshev Lowpass Filter prototype Element Values

Like other types of filters, the design and realisation of actual Chebyshev bandpass filter is based on the normalized lowpass filter prototype element values. The lowpass filter prototype element values are impedance and frequency scaled for realisation of the actual bandpass filter. The Chebyshev lowpass filter prototype element values are calculated from the lumped element lowpass filter prototype circuit shown in Fig. 5.2.

The calculated element values depend on the specified passband ripple level (A_r). The value of the normalized source impedance is given by $g_0 = 1$. The load impedance (r) value depends on the order of the filter N and $r = 1$ for N odd and $r = \coth^2(\frac{\beta}{4})$ for N even. The other element values are given by:

**Figure 5.2:** Lumped element lowpass filter circuit

$$g_1 = \frac{2a_1}{\gamma} \quad (5.8)$$

$$g_k = \frac{4a_{k-1}a_k}{b_{k-1}g_{k-1}} \quad \text{for } k = 2, 3, \dots, N \quad (5.9)$$

where

$$a_k = \sin \left[\frac{(2k-1)\pi}{2N} \right] \quad \text{for } k = 1, 2, \dots, N \quad (5.10)$$

$$b_k = \gamma^2 + \sin^2 \left(\frac{k\pi}{N} \right) \quad \text{for } k = 1, 2, \dots, N \quad (5.11)$$

$$\beta = \ln \left(\coth \frac{A_r}{17.37} \right) \quad \text{where } A_r \text{ is ripple level in dB} \quad (5.12)$$

$$\gamma = \sinh \left(\frac{\beta}{2N} \right). \quad (5.13)$$

5.1.3 Narrow Band Coupled Resonator Bandpass Filters

At microwave frequencies narrow band bandpass filters are often realised from high-quality factor (high- Q) resonant circuits or cavities loosely coupled to each other in cascade. At this frequency range, the resonators are usually realised from transmission lines and rectangular waveguides. The selectivity factor or steepness of cutoff between passband frequency edge and stopband frequency edge increases as the number of resonators are increased [27]. The number of resonators also determine the order of the filter. The coupling between adjacent resonators can either be inductive (impedance inverter) or capacitive (admittance inverter). The external quality factor Q_{ex} of the first and last resonators, in the filter resonator cascade arrangement, is lowered

because of the source and load impedances loading of the respective resonators.

All types of narrow band bandpass coupled resonator filters are basically characterized by three parameters. These are the synchronous tuning frequency of each resonator, main line coupling between adjacent resonators and the external quality factor Q_{ex} of the first and last resonators [28]. An impedance inverter K coupling model will be discussed and used in this chapter. An impedance inverter K model for Chebyshev bandpass filter is shown in Fig. 5.3. There are several lumped element equivalent circuits for the impedance inverter K . A typical T-lumped element equivalent circuit of a impedance inverter K is shown in Fig. 5.4. The value of the coupling factor K between two adjacent resonators can be calculated from the resonant frequencies of each resonator and this will be discussed in detail in the next subsection. The value of main line coupling factor K can also be calculated from the relevant lowpass filter prototype element values using:

$$K_{i,i+1} = \frac{\pi BW}{2\sqrt{g_i \cdot g_{i+1}}} \quad \text{for } i = 1 \text{ to } (N - 1) \quad (5.14)$$

where BW is the filter relative bandwidth and N is the number of resonators [29].

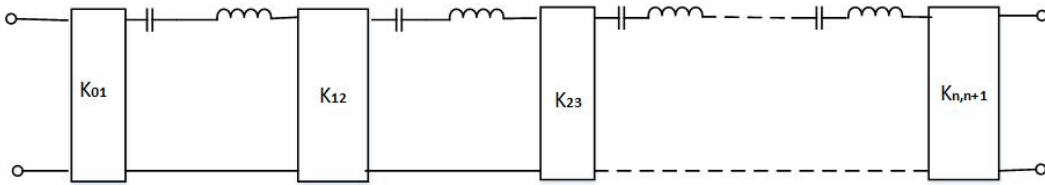


Figure 5.3: Impedance Inverter model for Chebyshev bandpass filter

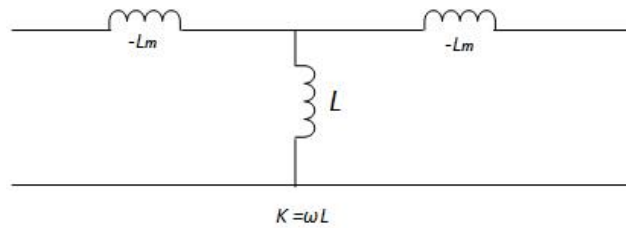


Figure 5.4: K-Inverter equivalent lumped elements circuit

The external quality factor value Q_{ex} of the first and last resonators can also be calculated from lowpass filter prototype element values using (5.15)

and (5.16). The external quality factor Q_{ex} can also be expressed in terms of coupling between the feed port and the first resonator using (5.17).

$$Q_{ex1} = \frac{2g_0g_1}{\pi BW} \quad \text{for first resonator} \quad (5.15)$$

$$Q_{exN} = \frac{2g_N \cdot g_{N+1}}{\pi BW} \quad \text{for last resonator} \quad (5.16)$$

$$\frac{K_{01}}{Z_o} = \sqrt{\frac{\pi}{2Q_{ex}}} \quad (5.17)$$

5.1.4 Calculation of Coupling Factor K Using Electric Wall Magnetic and Wall Symmetry

The coupling factor K between two adjacent resonators can be calculated from their respective resonant frequencies. The circuit model of two adjacent coupled resonators is shown in Fig. 5.5 (a).

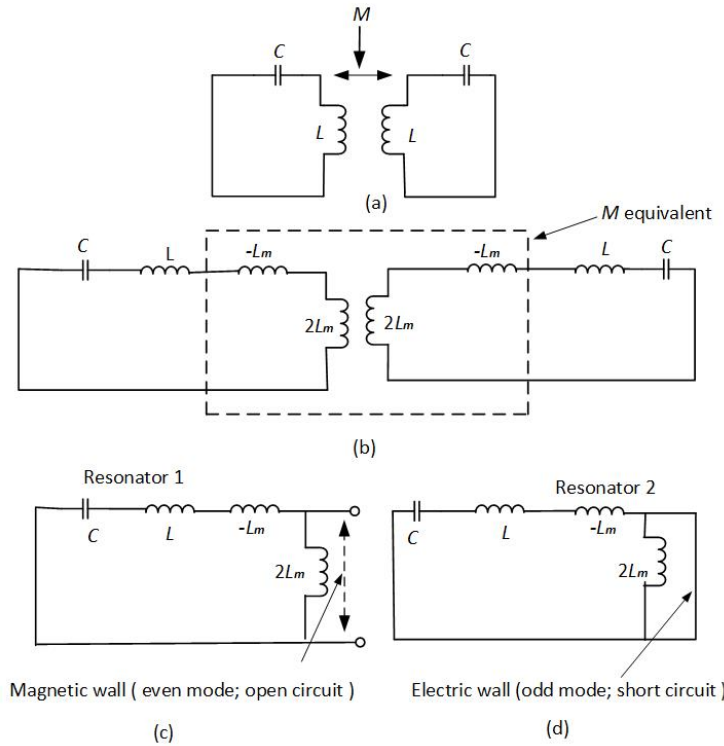


Figure 5.5: Electric wall and magnetic wall symmetry method

Using the electric wall and magnetic wall symmetry method (even and mode analysis), the two resonators in the circuit model can be divided into single resonators with an electric and magnetic wall terminations. The symmetrical mutual inductive coupling M between the two resonators shown in Fig. 5.5 (a), can be broken down into an equivalent circuit shown in Fig. 5.5 (b). The mutual coupling equivalent circuit of Fig. 5.5 (b) is a T-impedance inverter K with two series inductors $-L_m$ and a shunt inductor L_m and is similar to the one shown in Fig. 5.4. The circuit of Fig. 5.5 (b) can be further broken down into two separate resonators of even and odd modes. The even mode resonator 1 is terminated with a magnetic wall, which is an open circuit termination as shown in Fig. 5.5(c). The odd mode resonator 2 is terminated with an electric wall, which is a short circuit termination as shown in Fig. 5.5(d). The odd and even mode resonant frequencies of the two individual resonator circuits are calculated using (5.18) and (5.19). The inductive coupling factor K_M between the two resonators is solved from (5.18) and (5.19) and is given by (5.20):

$$f_m = \frac{1}{2\pi\sqrt{(L + L_m)C}} \quad (5.18)$$

$$f_e = \frac{1}{2\pi\sqrt{(L - L_m)C}} \quad (5.19)$$

$$K_M = \frac{L_m}{L} = \frac{f_e^2 - f_m^2}{f_e^2 + f_m^2}. \quad (5.20)$$

Equation (5.20) will be used in the practical analysis and calculation of coupling factor K and the related distance s between two groove gap waveguide resonators in the following sections.

The calculated values of coupling factor K and the the external quality factor Q_{ex} are electrical parameters. The two parameters need to be translated into physical dimensions for the realisation of actual bandpass filters. The value of K needs to be translated into some physical dimension relating to the two adjacent resonators. The value of Q_{ex} needs to be translated into some physical dimension relating the source and first resonator and as already stated this will also apply to the last resonator and its load in all the filter examples discussed in this chapter.

The next section will look at narrow band microwave groove gap waveguide coupled resonator bandpass filters. The main line coupling factor K and the external quality external factor Q_{ex} which are electrical parameters, will be translated into physical dimensions. The methods for calculation and practical realization of K and Q_{ex} values will be discussed. It should be noted

that although the groove gap waveguide resonators were used for calculation and analysis of the two parameters, the methods and procedure generally apply to other types of coupled resonator bandpass filters as well.

5.2 Narrow Band Microwave Groove Gap Waveguide Coupled Resonator Bandpass Filters

Third and fifth order narrow band microwave groove gap waveguide bandpass filter examples [5] using high Q groove gap waveguide resonators were done. The groove gap waveguide resonators and filter dimensions from [5] were used. The filters were realised from cascaded groove gap waveguide resonators which were loosely coupled. The coupling factor K and the physical distance s between two adjacent groove gap waveguide resonators was analysed and calculated using the S-parameter and eigenmode solver methods. The external quality factor Q_{ex} of the typical first groove gap waveguide resonator and the source SMA port position x was calculated and analysed using the group delay method.

5.2.1 Practical Realisation of Coupling Factor K Using S-Parameter Method

The S-parameters S_{11} and S_{21} of two adjacent resonators were used in the analysis of coupling factor K between the two adjacent groove gap waveguide resonators separated by distance s . The two resonator arrangement with symmetrical ports separated by a distance $s = 1.5$ mm is shown in Fig. 5.6. The initial value of s was arbitrary as any other reasonable value could have been used. Standard Ku band dimensions of the conventional hollow rectangular waveguide [5] with a width of 15 mm and a length of 15.6 mm were used for the resonators. The other dimensions of the groove gap waveguide resonators were pins of width $a = 1$ mm, pin height $d = 6.25$ mm, distance between pins period $p = 3$ mm, vacuum gap height $h = 1$ mm. The dimensions were for the intended 10 - 20 GHz stopband of the groove gap waveguide bandpass filters.

The resonator arrangement was simulated as a two port network for S_{11} and S_{21} using CST. For the S-parameter method to work, the two resonators were weakly coupled to their respective ports [29]. The two resonators were weakly coupled to their ports by reducing the SMA port inner probe length into the resonators. The SMA ports were placed on the upper PEC plate

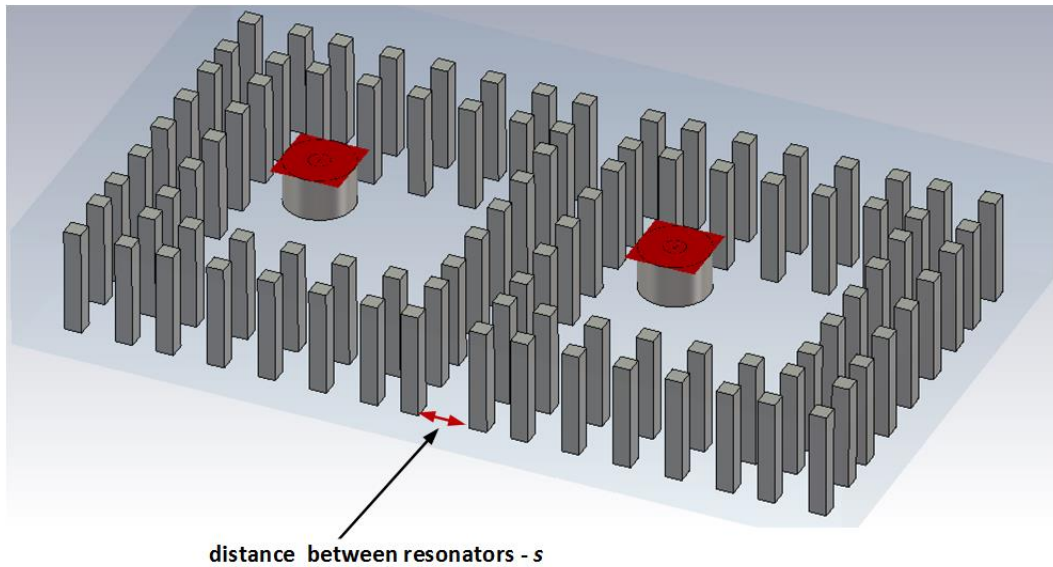


Figure 5.6: Two resonator arrangement for the S-parameter method

which is 1 mm above the resonator pins with inner probes of the ports extending into the resonator cavities. The upper PEC plate is not shown in Fig. 5.6 for clarity. Two troughs for the simulated S_{11} and S_{21} parameters were observed. The two troughs correspond to the resonant frequency of each resonator. The distance between the two resonators s was varied and the troughs were observed to be shifting in line with s variation. The resonance troughs and their corresponding resonant frequencies are shown in Fig. 5.7.

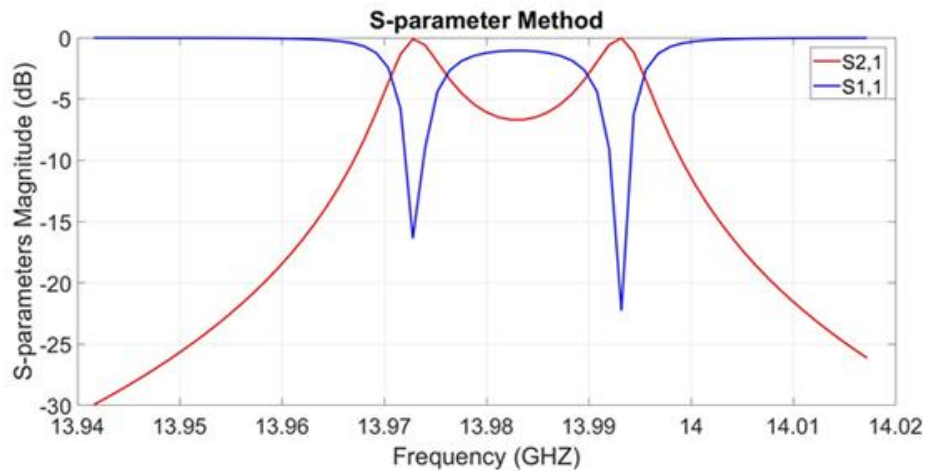


Figure 5.7: Main-line coupling S-parameters

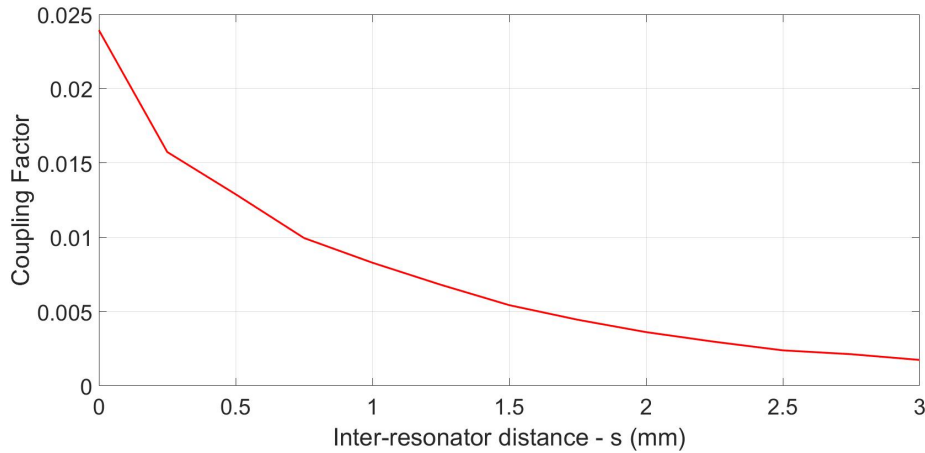
The two S_{11} resonance trough frequencies were used to calculate the

| | | | | | | | | |
|-----|--------|-------|-------|--------|-------|--------|--------|-------|
| s | 0 | 0.5 | 1 | 1.5 | 2 | 2.5 | 2.75 | 3 |
| K | 0.0024 | 0.014 | 0.009 | 0.0058 | 0.004 | 0.0037 | 0.0034 | 0.003 |

Table 5.1: Coupling K and corresponding inter-resonator distance s

coupling K between the two resonators using (5.20) for inter-resonator distance $s = 1.5$ mm. The calculated value was $K = 0.0057$. This then was the coupling factor K value between the two resonators for the particular inter-resonator separation distance of $s = 1.5$ mm. Evenly spaced sample values of s in the range $[0 - 3]$ mm were used for S_{11} simulation and the resultant resonant frequencies values were used to calculate the corresponding values of K using (5.20). The calculated values of K and the corresponding distances s values were tabulated and are shown in Table 5.1.

Using the results of Table 5.1, an approximated graph of main-line coupling factor K and the corresponding inter-resonator separation distance s was plotted and is shown in Fig. 5.8. The graph shows the physical relationship between the electrical parameter K and the corresponding physical inter-resonator-distances s .

**Figure 5.8:** Approximated graph of K and inter-resonator distance s (mm)

5.2.2 Practical Realisation of Coupling Factor K Using Eigenmode Method

The second eigenmode solver method was used to calculate and analyse the coupling factor K between two groove gap waveguide resonators which were

placed next to each other separated by distance s . The analysis was done using the CST eigenmode solver option. The dimensions of the groove gap waveguide resonators used in the analysis were similar to those used in the S-parameter method. The two adjacent resonators were separated by distance $s = 1.5$ mm. The initial value of s was arbitrary as any other reasonable value could have been used. The two resonator arrangement is shown in Fig. 5.9.

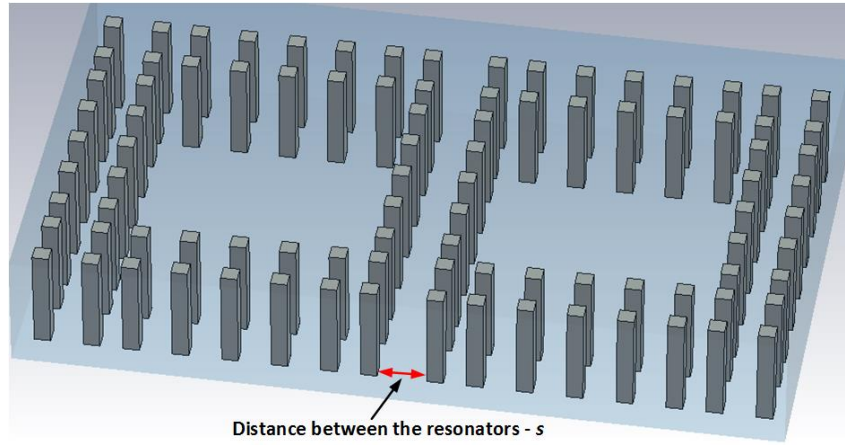
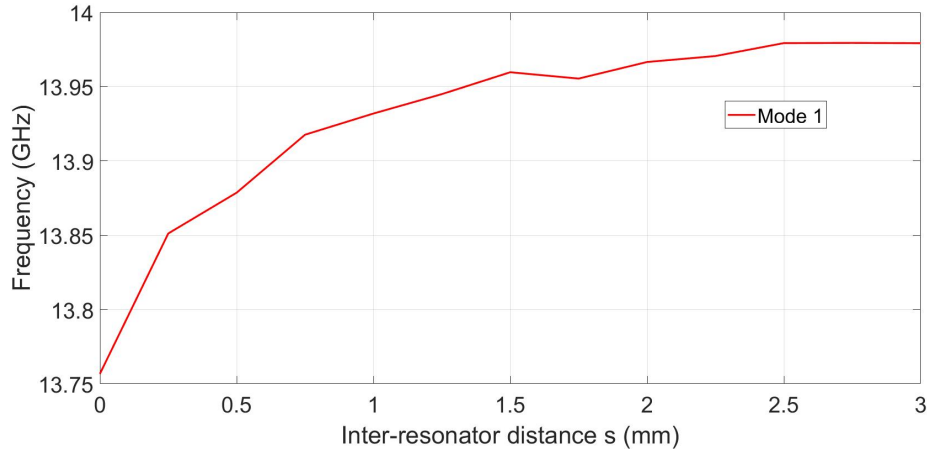
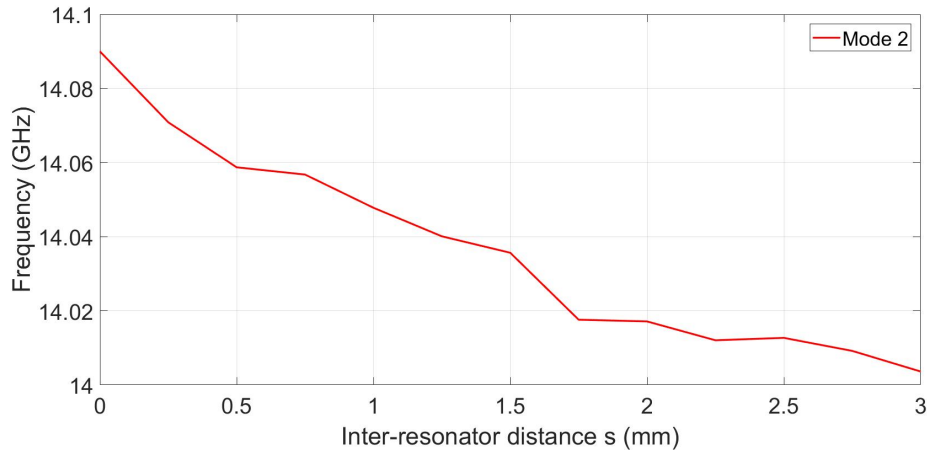


Figure 5.9: Eigenmode solver method

The resonator arrangement was simulated using CST eigenmode solver for two modes. Two resultant resonant frequencies for each mode were observed. These were the resonant frequencies of each resonator in the simulated arrangement. The two frequencies were post processed using the CST post processing results template. The post processing of the two frequencies was based on (5.20). For the inter-resonator separation distance $s = 1.5$ mm, the template calculated a value of $K = 0.0055$. This then was the coupling factor K value between the two groove gap waveguide resonators for the particular separation distance $s = 1.5$ mm. A parameter sweep of distance s was done in the $[0 - 3]$ mm range to for calculation and plotting of values of K and the corresponding s values in CST. The resultant graphs of K as a function of s and all the post processed results are shown in Figs. 5.10 - 12.

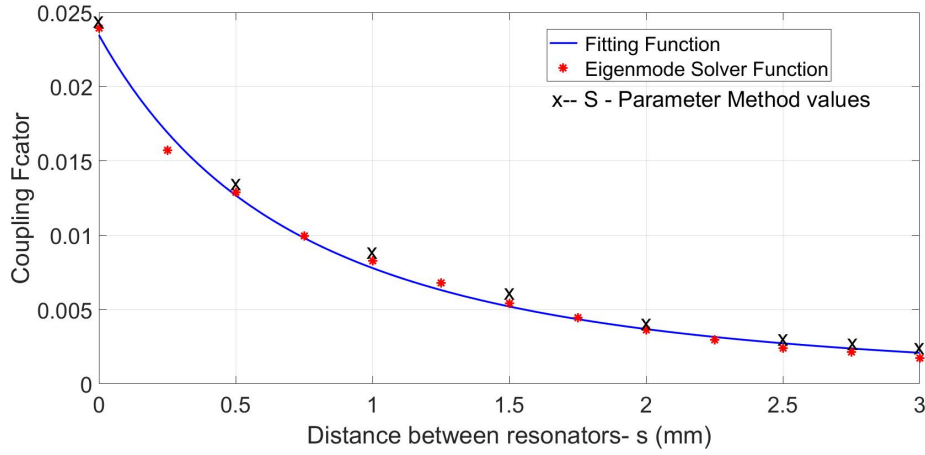
The graph of Fig. 5.12 shows the general relationship between coupling factor K and the corresponding variation of distance s between two resonators. A MATLAB code was written to approximate the best fit function for the eigenmode solver resultant function of Fig. 5.12. The non-smooth and non-linear behaviour of K as a function s graph was approximated by the best fit function to get a closed form functional relationship between the distance s and the coupling factor K . The fitting function is monotonic and

**Figure 5.10:** Mode 1**Figure 5.11:** Mode 2

it mathematically entails the simple, but non-linear relationship between s and coupling factor K which is good for the space mapping. We can therefore encode the complex non-linear behaviour of K as a function of s into our coarse model. The best fit function is also shown in Fig. 5.12. The S-parameter method sample values were also plotted in Fig. 5.12 for comparison. The two methods gave similar results. The approximated best fit function is:

$$K_s = \frac{a_s}{100}(s + c_s)^{-b_s} \quad (5.21)$$

where a , b and c are the fitting constants.

Figure 5.12: Eigenmode solver method for K and s

5.2.3 Calculation and Realisation of The External Quality Factor Q_{ex} Using Group Delay Method

The group delay method was used to analyse the relationship between external quality factor Q_{ex} of a typical first groove gap waveguide resonator and the SMA port feed point x . The 3-D model of the groove gap waveguide resonator and SMA port feed position x used in the analysis is shown in Fig. 5.13. The dimensions of the groove gap waveguide resonator are similar to those used in the S-parameter and eigenmode solver methods. The SMA port inner probe depth into the resonator was kept constant at 2 mm. The simulation set-up is fully discussed later in the section.

The group delay method is based on the group delay of the reflection coefficient S_{11} phase in a typical source and first resonator arrangement. The circuit model of the typical first resonator and source arrangement is shown in Fig. 5.14. Without the source, the resonator in the circuit model has infinite quality factor Q - that is there is only stored energy and no dissipated energy. The source port in the circuit model of Fig. 5.14 loads the resonator with a lossy component (the port impedance). The external quality factor Q_{ex} of the loaded resonator goes down since $Q = (\text{stored energy}) / (\text{dissipated energy})$.

The reflection coefficient S_{11} of the circuit model feed line of input admittance G loaded by the resonator ($L-C$) as shown in Fig. 5.14 is:

$$S_{11} = \frac{G - Y_{in}}{G + Y_{in}} = \frac{1 - \frac{Y_{in}}{G}}{1 + \frac{Y_{in}}{G}} \quad (5.22)$$

with impedance seen into the resonator as :

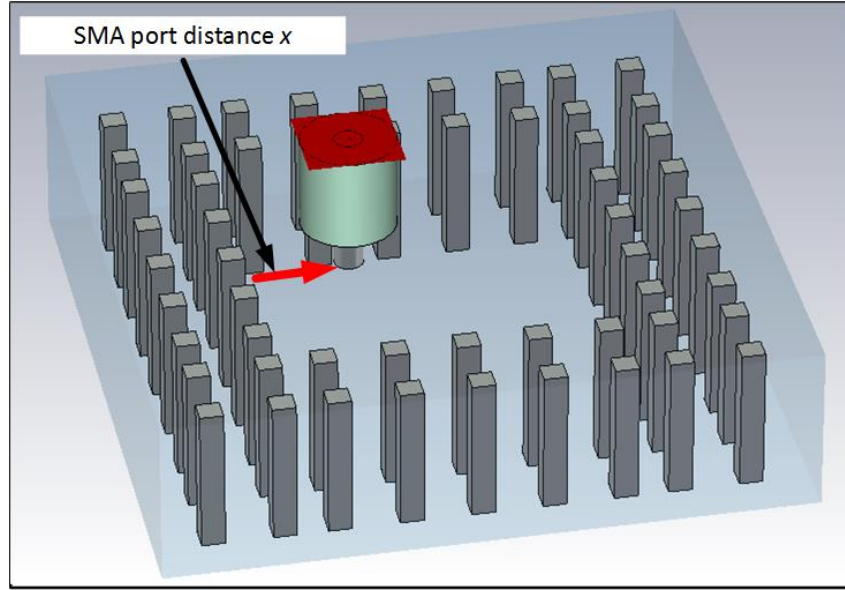


Figure 5.13: Group delay method with resonator and SMA port distance x

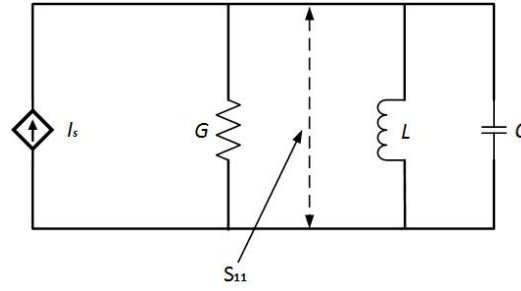


Figure 5.14: Typical circuit model of source and first resonator

$$Y_{in} = j\omega C + \frac{1}{j\omega L} = j\omega_0 \left(\frac{\omega}{\omega_0} - \frac{\omega_0}{\omega} \right) \quad (5.23)$$

where resonance frequency $\omega_0 = \frac{1}{\sqrt{LC}}$. For frequencies near resonance, $\omega = \omega_0 + \Delta\omega$, where $\Delta\omega \ll \omega_0$ and (5.23) can be approximated by:

$$Y_{in} \approx j\omega_0 C \frac{2\Delta\omega}{\omega_0} \quad (5.24)$$

where $\Delta\omega$ is the small frequency deviation from resonant frequency. Substituting (5.24) into (5.22), the reflection coefficient S_{11} can be re-written as:

$$S_{11} = \frac{1 - jQ_{ex} (2\Delta\omega/\omega_0)}{1 + jQ_{ex} (2\Delta\omega/\omega_0)} \quad (5.25)$$

where the external quality factor $Q_{ex} = (\omega_0 C/G)$. Equation(5.25) can be re-written in polar form as :

$$S_{11} = \left| \frac{1 - jQ_{ex}(2\Delta\omega/\omega_0)}{1 + jQ_{ex}(2\Delta\omega/\omega_0)} \right| \angle \varphi \quad (5.26)$$

where the reflection phase angle φ is given by:

$$\varphi = -2 \arctan \left(2Q_{ex} \left(2 \frac{(\omega - \omega_0)}{\omega_0} \right) \right). \quad (5.27)$$

The group delay (τ) is the derivative of the reflection coefficient S_{11} phase angle φ with respect to the angular frequency. Generally, it is a measure of the distortion in the signal introduced by phase differences for different frequencies. The group delay is the slope of the graph of S_{11} (phase) as a function of frequency and is given by:

$$\tau = -\frac{\delta\varphi}{\delta\omega} \quad (5.28)$$

$$\tau = \frac{4Q_{ex}}{\omega_0} \frac{1}{1 + (2Q_{ex}(\omega - \omega_0/\omega_0))^2}. \quad (5.29)$$

Equation (5.29) gives the general group delay as a function of frequency. For convenience and simplicity we select the resonant frequency because it simplifies (5.29) and is easy to identify the resulting graph of the group delay. The group delay τ_{max} is maximum at resonance where $\omega = \omega_0$, and the external quality factor Q_{ex} at resonance from (5.29) is:

$$Q_{ex} = \frac{2\pi f_0 \tau_{max}}{4} = \frac{\pi f_0 \tau_{max}}{2}. \quad (5.30)$$

For the analysis of the relationship between the external quality factor Q_{ex} of the groove gap waveguide resonator and the SMA port feed position x , the value of x was set to 3 mm in the arrangement of Fig. 5.13. Again the value of x was arbitrary as any other reasonable value could have been used. The SMA port feed point x is referenced from inner pin row to the centre of SMA port inner probe as shown the diagram. The SMA port inner probe depth into the resonator was kept constant at 2 mm. The groove gap waveguide resonator dimensions are similar to the those used in the S-parameter and eigenmode solver methods. The arrangement of Fig. 5.13 was simulated in

CST for the reflection coefficient S_{11} .

The reflection coefficient S_{11} simulation results were post processed using the CST post processing result template. The filter analysis and group delay options in the results template were selected and used to process the S_{11} results using (5.30). The template calculated value of Q_{ex} was 124. This then was the groove gap waveguide resonator external quality factor Q_{ex} value for the particular SMA port feed position $x = 3$ mm. A parameter sweep of SMA port position x was done in the [2 - 4.5] mm range for calculating and plotting of Q_{ex} values against x range values. The plot results of the post processing results template are shown in Figs. 5.15 - 18. The S_{11} phase group delay results are shown in Fig. 5.15.

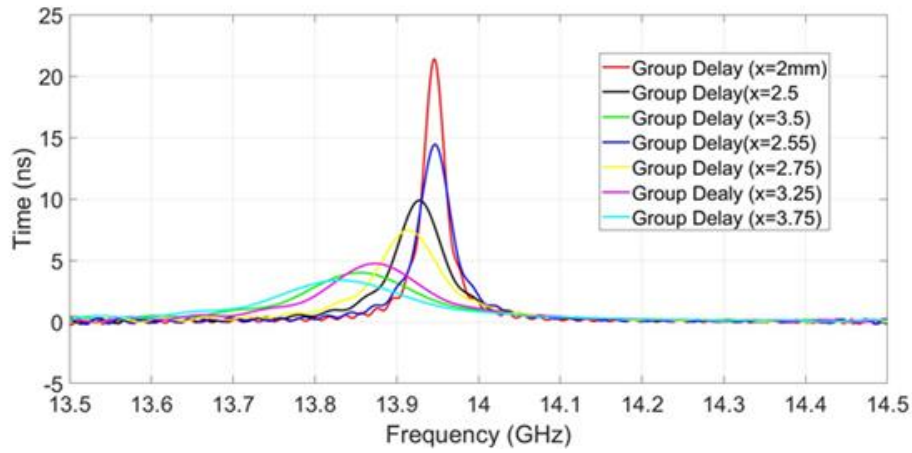
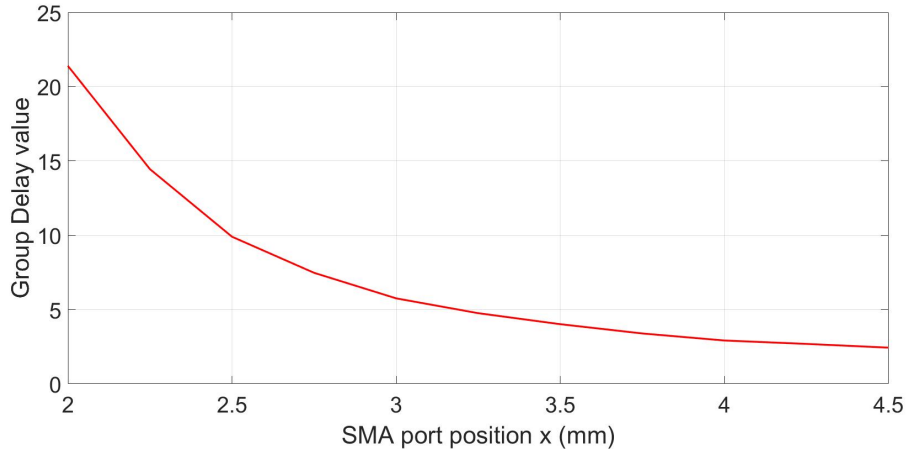
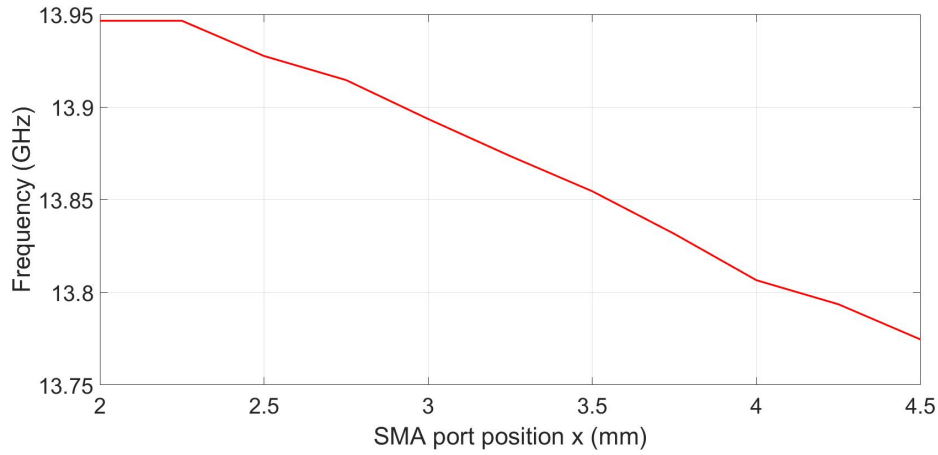


Figure 5.15: Group delay of the S_{11} Phase

Fig. 5.18 graph shows the variation of the external quality factor Q_{ex} of the groove gap waveguide resonator in relation to the physical SMA port feed point x position in the given range. For the same reasons as was stated in subsection 5.2.2, a MATLAB code of the best fit function was done. The best fit function is given by (5.31) and is also plotted in Fig. 5.18.

$$Q_{ex}(x) = \frac{a_x}{1000}(x + c_x)^{-b_x}. \quad (5.31)$$

The coupling factor K and external quality factor Q_{ex} fitted functions of Figs. 5.12 and 5.18 were used in the next subsection for the design and optimisation of a third and fifth order narrow band microwave groove gap

Figure 5.16: Group delay values and distance x Figure 5.17: Group delay frequency and distance x

waveguide bandpass filters. The filters were optimised using space mapping.

5.2.4 Design and Optimisation of a Third Order Narrow Band Microwave Groove Gap Waveguide Coupled Resonator Bandpass Filter

A third order microwave narrow band groove gap waveguide coupled resonator bandpass filter [5] example used. The filter was optimised using space mapping. The groove gap waveguide resonators and filter dimensions are similar to those stated in [5] and are as given in subsection 5.2.2 . The filter specifications were for 0.1 dB transmission equal ripple response with a bandpass return

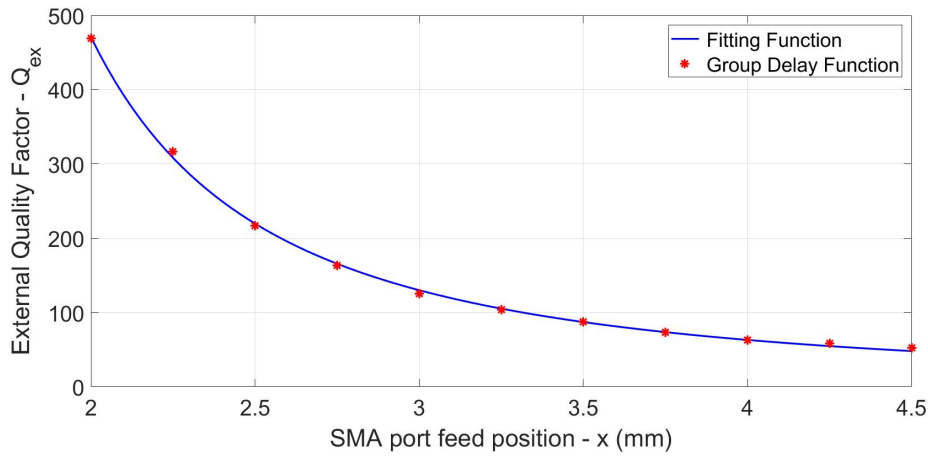


Figure 5.18: External quality factor Q_{ex} and SMA port position x

loss of 16.4 dB, a fractional bandwidth of 1% and a centre frequency of 14 GHz.

The Chebychev low pass prototype table for 0.1 dB transmission equal ripple of [29] was used for the prototype elements values. The element values are $g_o = g_4 = 1$, $g_1 = g_3 = 1.0315$ and $g_2 = 1.1474$. The main-line coupling value for $K_{12} = K_{23}$ was calculated using (5.14) and the external quality factor Q_{ex} was calculated using equation (5.15). The value of $K_{12} = K_{23} = 0.0144$ and the value of $Q_{ex} = 65.67$. The physical inter-resonator separation distance s and SMA probe position x corresponding to the calculated values of K and Q_{ex} were estimated from the fitted functions of Fig. 5.12 and Fig. 5.18. These were used as starting design parameters in the evaluation of the fine model and optimisation of the filter through space mapping to be discussed later.

For space mapping, the groove gap waveguide resonators of the filter were coarse modelled by a 50 Ω half wavelength transmission line. A hollow rectangular waveguide model could have been equally used, but the transmission line was chosen because it is simple to analyse in a circuit model environment. We expect the results of the transmission line model to be good because of the very narrow bandwidth concerned, and that the dispersion effects should play a very small role. We account for the different wavelengths in the coarse and fine models by applying a constant offset between the length of the transmission line and the length of the resonator to get the initial design value. The remaining small differences are handled by space mapping. For the filter centre frequency of 14 GHz, a half wavelength transmission line of length of 10.71 mm was calculated and used for the coarse model.

The transmission line coarse model schematic diagram is shown in Fig. 5.19. The initial calculated normalized values of K and Q_{ex} were scaled to

the line characteristic impedance value of 50Ω in the coarse model. The calculated $\frac{\lambda}{2}$ length of 10.71 mm was used for both the outer transmission line resonator pair L_1 and middle resonator length L_2 . The coarse model was simulated in MWO and the optimum response of the coarse model is shown in Fig. 5.20.

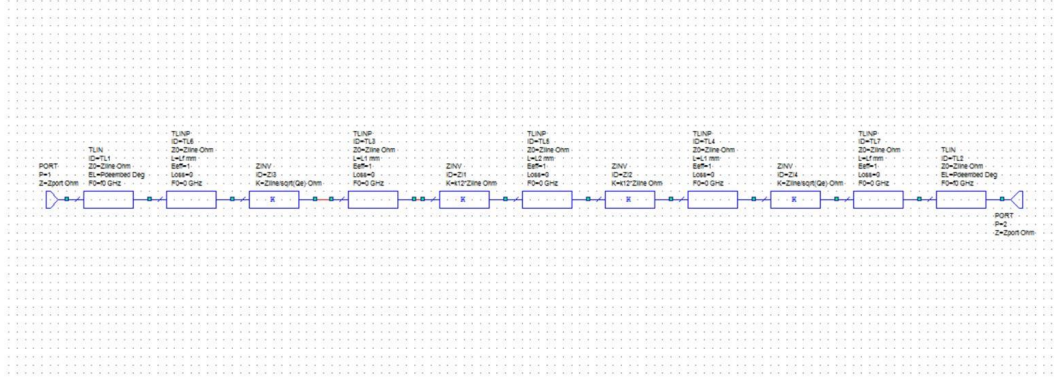


Figure 5.19: Third order bandpass filter coarse model

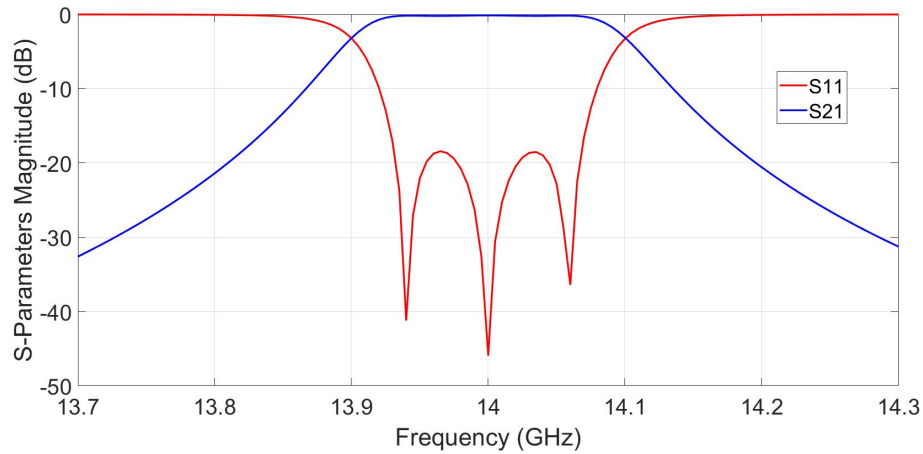


Figure 5.20: Third order bandpass filter coarse model S-parameters

As was discussed in Chapter 4, the geometry of the hollow rectangular waveguide was used as a starting geometry of the groove gap waveguide bandpass filter fine model because of their resemblance. The groove waveguide resonators dimensions used were those of a standard Ku band hollow rectangular waveguide, of width of 15.8 mm. The lengths of all the three resonators were approximated to 15.6 mm. The widths of all the three resonators were kept constant at 15.8 mm and the lengths of the outer pair resonators L_1

and that of the middle resonator L_2 were chosen as the design parameters all with starting value of 15.6 mm. The other design parameter was the coupling distance s between the resonators as shown in Fig. 5.21 with its starting design value approximated from fitted function of Fig. 5.12. The last design parameter was the input SMA port feed point x in the first resonator. The value of x also applied to the load SMA port load point and the last resonator. The starting design value of x was approximated from fitted function of Fig. 5.18. There were four (L_1 , L_2 , s and x) design parameters. The filter fine model and the design parameters are shown in Fig. 5.21.

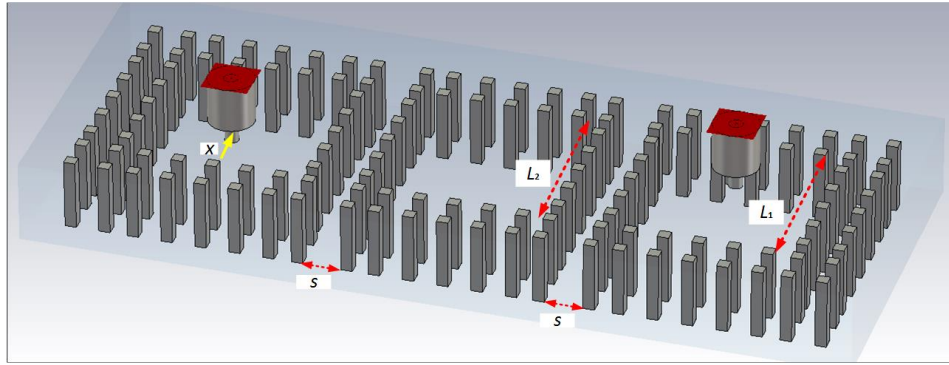


Figure 5.21: Fine model and design parameters

The fine model was simulated using CST and an in-house space mapping code was used in optimising the filter design. The reflection coefficient $|S_{11}|$ was used as the design goal type in the space mapping code. The space mapping code was formatted for input space mapping and the input space mapping steps are as explained in Chapter 3. In the first iteration of the space mapping code, the fine model is evaluated using the initial design parameter values. The first iteration S-parameter response is shown in Fig. 5.22. From the first iteration results, the filter did not meet the design specifications. Using the design parameters, the coarse model response was mapped and aligned to the fine model response which resulted in an aligned surrogate model. The aligned surrogate model was optimised to get new design parameter values for the second iteration evaluation of the fine model.

The alignment and optimisation steps were repeated recursively until the fine model evaluation met the design specifications. It took 12 iterations of the fine model evaluation to meet the design specifications. The last iteration result is shown in Fig. 5.23. The optimum fine model S-parameter response is shown in Fig. 5.24.

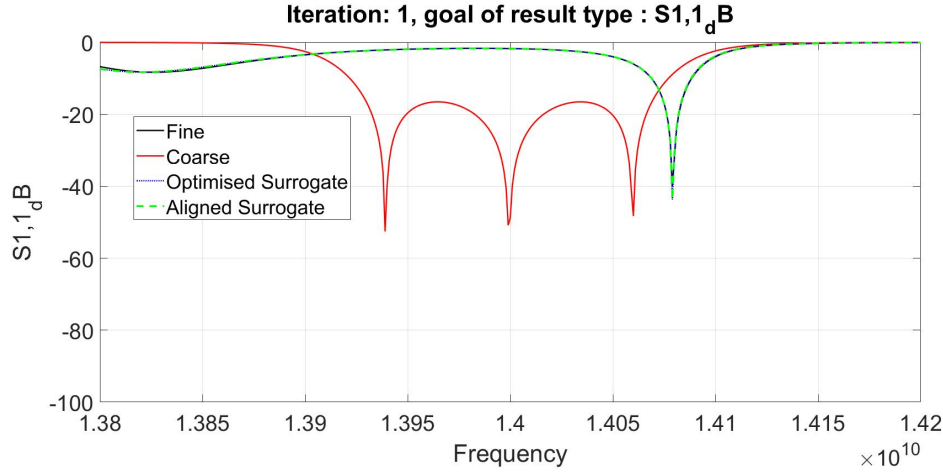


Figure 5.22: Third order first iteration

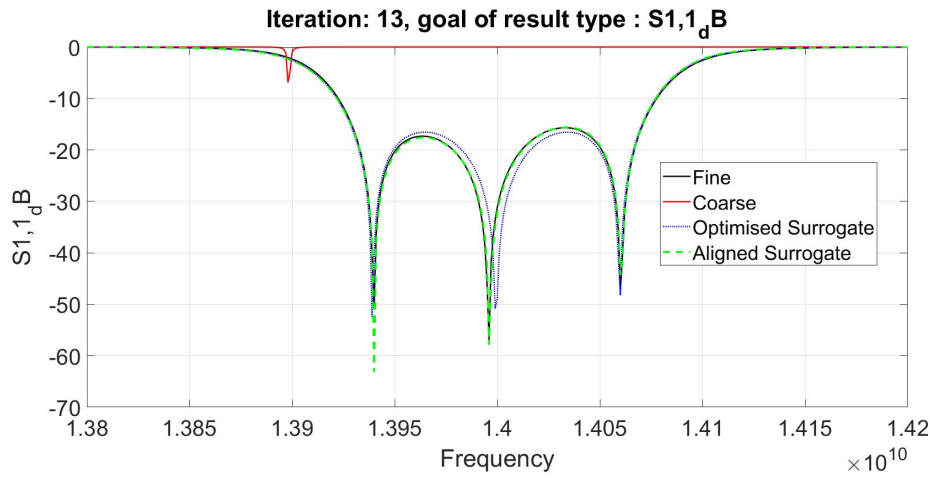


Figure 5.23: Third order last iteration

The results of the initial and optimum design parameter values were tabulated and analysed and are shown in Table 5.2. From Table 5.2 there were changes in all the four design parameters between the initial and optimum values. The results generally show that using the calculated design parameter values for filter design, in most cases does not give an optimum design. The design parameters need to be tuned or optimised to meet the design specifications.

For comparison, the same filter was directly optimised using CST optimiser. The S-parameters response of direct optimisation are shown in Fig. 5.24 after 47 iterations of evaluating the fine model. The direct optimisation results show that filter optimisation did not converge whereas it took only 12 iterations of evaluating the fine model to optimise the filter using space

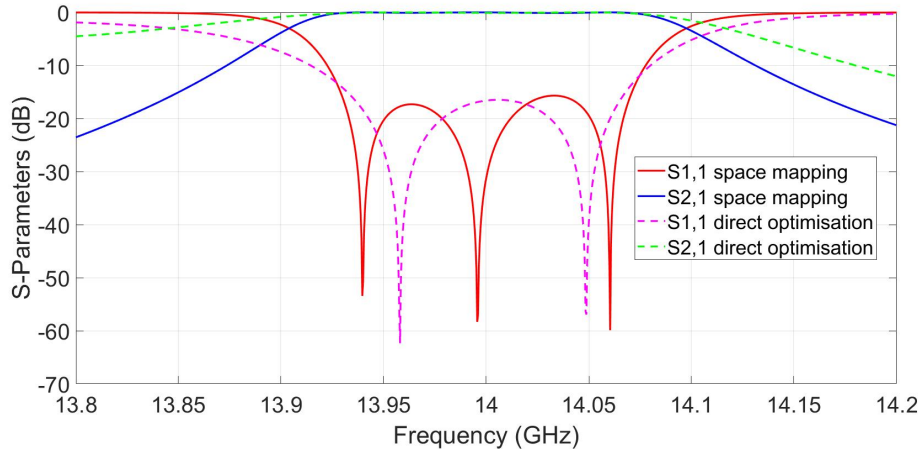


Figure 5.24: Space mapping and Direct optimisation Fine model S-parameters

| Design Variables | Initial value | optimum value | |
|------------------|---------------|---------------|--|
| L_1 | 15.6 | 15.4698 | |
| L_2 | 15.6 | 15.6763 | |
| s | 0.3863 | 0.9309 | |
| x | 3.9325 | 3.3971 | |

Table 5.2: Filter initial and optimum design parameter values

mapping. This shows the relative efficiency of space mapping when compared to other direct optimisation methods.

5.2.5 Design and Optimisation of a Fifth Order Narrow Band Microwave Groove Gap Waveguide Coupled Resonators Bandpass Filter

A fifth order version of the same filter described in the previous subsection was done and optimised using space mapping. The filter specifications were similar to those of the third order.

The Chebyshev low pass prototype table for 0.1 dB ripple was used for the elements values of the fifth order filter. The element values are $g_o = g_6 = 1$, $g_1 = g_5 = 1.1468$, $g_2 = g_4 = 1.3712$ and $g_3 = 1.9750$. The main-line coupling values for $K_{12} = K_{45}$ and $K_{23} = K_{34}$ were calculated using equation (5.14) and the external quality factor Q_{ex} was calculated using equation (5.15). The calculated values of $K_{12} = K_{45} = 0.013$, $K_{23} = K_{34} = 0.0095$ and the value of $Q_{ex} = 73$. The corresponding values of s_{12} , s_{23} and x were estimated from

graphs of Fig. 5.12 and Fig. 5.18. These were used as initial design values for the fine model in the optimisation of the filter using space mapping.

For the same reasons as discussed in the previous third order filter example, the groove gap waveguide resonators of the filter were coarse modelled by a $50\ \Omega$ half wavelength transmission line. The same half wavelength of 10.71 mm was used for all the coarse model line resonators lengths. The coarse model was simulated in MWO with calculated values of K_{12} , K_{23} and Q_{ex} scaled to $50\ \Omega$ line impedance. The schematic diagram of the coarse model is shown in Fig. 5.25 and the optimum coarse model response is shown in Fig. 5.26.

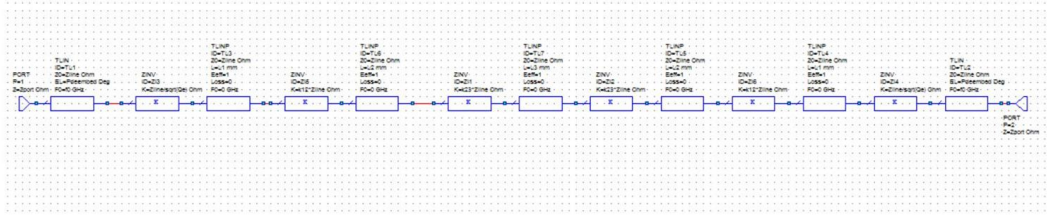


Figure 5.25: Fifth order coarse model schematic

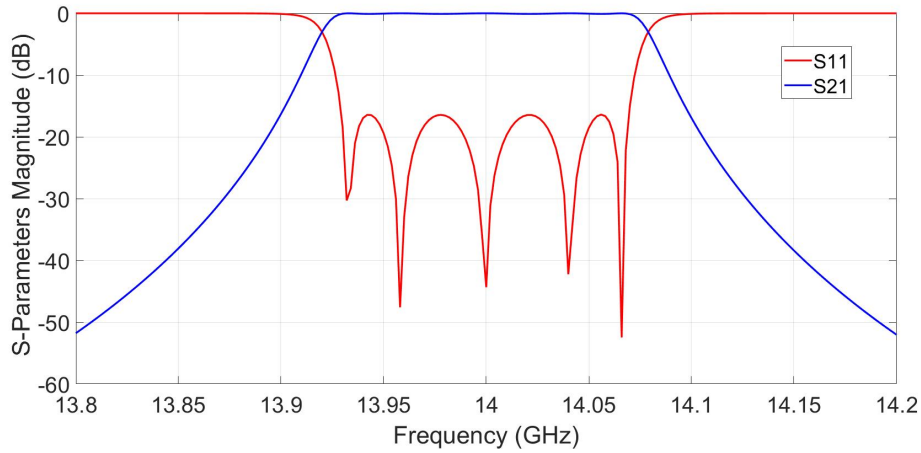


Figure 5.26: Fifth order coarse model S-parameters

As was stated in the third order filter design example, the geometry of a hollow rectangular waveguide was used as a starting geometry in this example as well. The width of all the five resonators was fixed at 15.8 mm. The length of the outer resonators pair L_1 , second inner most L_2 and the middle resonator L_3 initial values were set to 15.6 mm. The three lengths were used as design parameters all with initial value of 15.6 mm.

The other design parameters were the SMA port feed point x , and the two inter-resonator distances s_{12} and s_{23} with their approximated values from Figs. 5.12 and 5.18 graphs used as the initial design values. There were six design parameters (L_1 , L_2 , L_3 , s_{12} , s_{23} and x). The 3-D fine model and the design parameters are shown in Fig. 5.27. The fine model was simulated in CST.

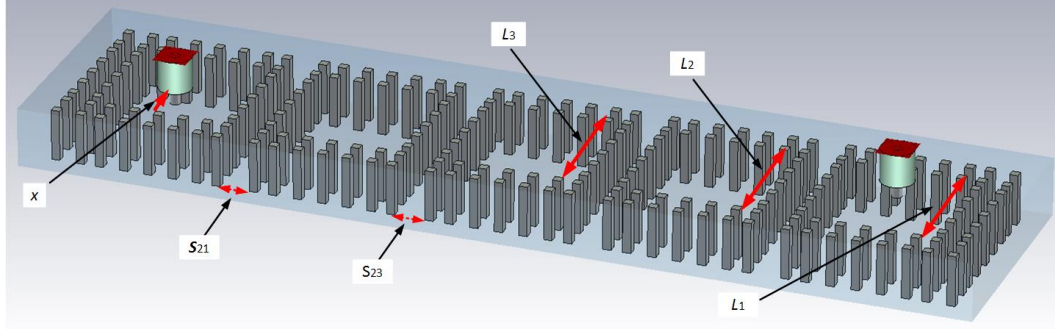


Figure 5.27: Fifth order fine model

An in-house space mapping code was used to optimise the six design parameters. The initial evaluation of the fine model using initial design values did not meet the design specifications as shown by the first iteration S-parameter response of Fig. 5.28. The same input space mapping steps mentioned and discussed in the third order filter example also apply to this example.

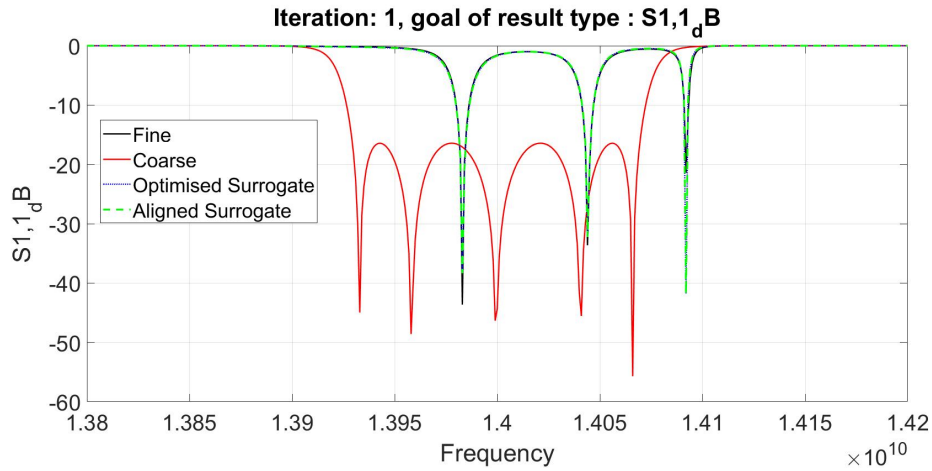


Figure 5.28: First iteration evaluation response of the fine model

The filter was optimised after 16 iterations of evaluating the fine model. The last iteration and the optimum fine model responses are shown in Figs. 5.29 and 5.30. The results of the initial design parameters values and optimum design parameters values were tabulated as before and are shown in Table 5.3.

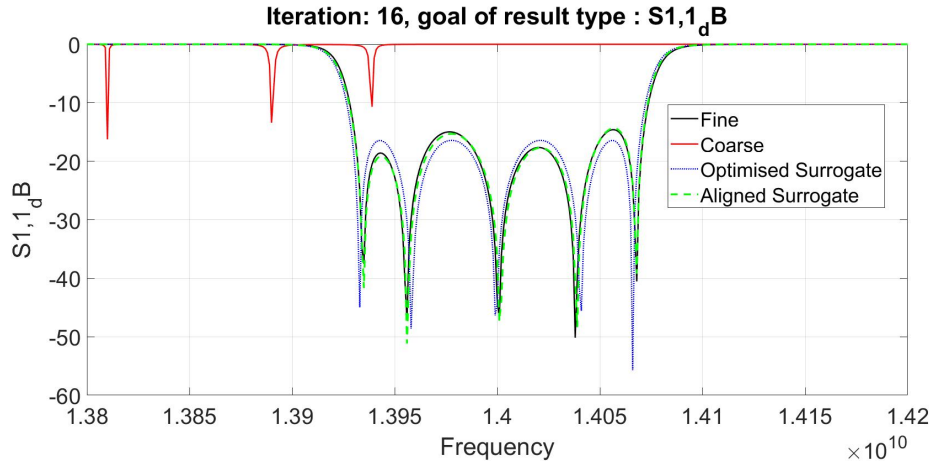


Figure 5.29: Last iteration response of the fine model

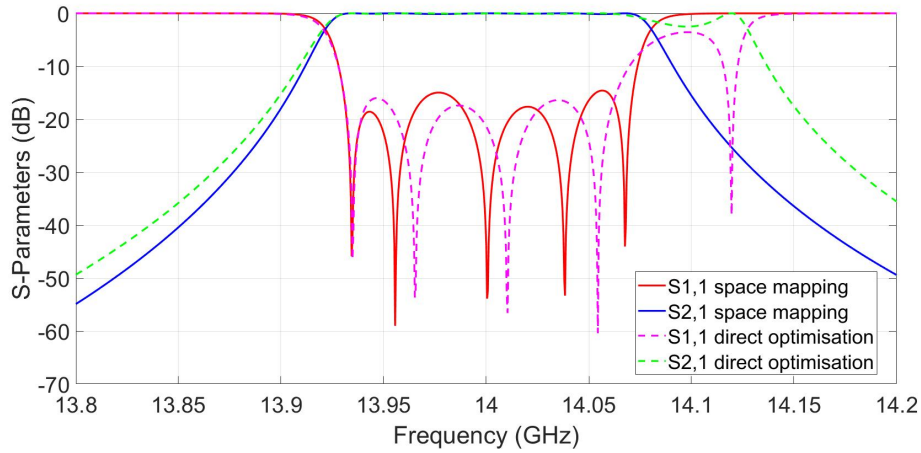


Figure 5.30: Space mapping and Direct optimisation fine model S-parameters

As as in the previous filter example there were changes in all the six design parameters and the results show that using the initial calculated design parameter values for filter design, in most cases does not result in an optimum design. The design parameters need to be tuned or optimised to meet the design specifications.

| Design Variables | Initial value | Optimum value |
|------------------|---------------|---------------|
| L_1 | 15.6 | 15.3429 |
| L_2 | 15.6 | 15.6706 |
| L_3 | 15.6 | 15.7177 |
| s_{12} | 1.1953 | 1.0721 |
| s_{23} | 1.5570 | 1.4526 |
| x | 3.1293 | 3.4993 |

Table 5.3: Filter initial and final design parameter values

For comparison, the same filter was optimised using the CST optimiser. The results of the CST optimiser are shown in Fig. 5.30. After 47 iterations of evaluating the fine model the CST optimiser failed to converge whereas it took only 16 iterations of evaluating the fine model using space mapping code to optimise the filter design. This shows that space mapping is a relatively faster and efficient optimisation method.

5.3 Third Order Narrow Band Microwave Ridge Gap Waveguide Coupled Resonators Bandpass Filter

A third order microwave narrow band ridge gap waveguide coupled resonator bandpass filter was designed and optimised using space mapping. The ridge gap waveguide resonators and filter dimensions were from [30] through personal communication. The dimension are pins width $a = 1.25$ mm, inter-pin spacing $p = 1.25$ mm, pin height $d = 1.9$ mm, ridge height $d_1 = 1.5$ mm, ridge width $a_1 = 1.3$ mm and the vacuum gap height between upper PEC plate and the ridge $h = 0.4$ mm. The ridge gap waveguide structure was slightly different from the one described in Chapter 2 in that there was no vacuum gap between the pins region and the upper PEC plate. The 3-D model structure of the ridge gap waveguide is shown in Fig. 5.31.

The third order bandpass filter was implemented using three ridge gap waveguide resonators which were loosely coupled in cascade as discussed in the earlier sections. The lengths of the resonators were half guided wavelength $\frac{\lambda_g}{2}$ of the ridge rectangular waveguide. The half guided wavelength length was calculated for the filter centre frequency of 28 GHz. Using the equivalence between ridge gap waveguide and ridged rectangular waveguide discussed in Chapter 4, the ridged rectangular waveguide guided wavelength formula was used to calculate the ridge gap waveguide resonator lengths.

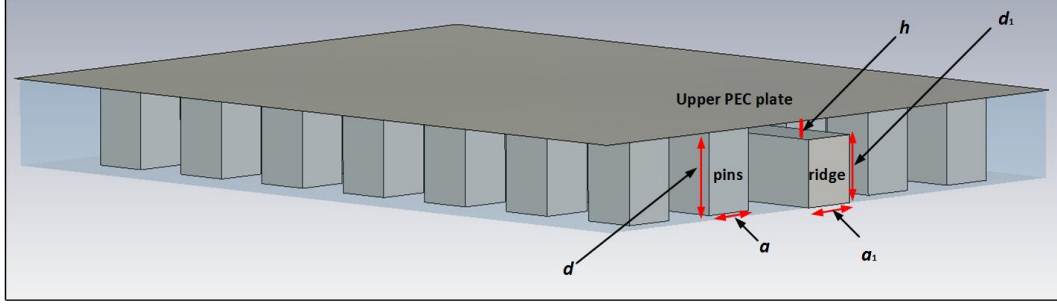


Figure 5.31: Ridge gap waveguide view and dimensions

The formula for the ridged rectangular waveguide guided wavelength λ_g [26] is:

$$\lambda_g = \frac{\lambda_o}{\sqrt{1 - \left(\frac{\lambda_o}{\lambda_{cr}}\right)^2}} \quad (5.32)$$

where λ_o is the free space wavelength and λ_{cr} is the ridged rectangular waveguide cut-off wavelength. The value of λ_{cr} is calculated from (4.11). The calculated value of $\lambda_g = 7.296$ mm.

Just like in the groove gap waveguide filters discussed earlier, the ridge gap waveguide resonators were used in the analysis and calculation of the electrical parameters coupling factor K and external quality factor Q_{ex} and relating them to some physical dimensions. The same methods and the procedure used in the analysis of groove gap waveguide resonators in subsections 5.2.2 and 5.2.3 were also applied in this example. The methods and procedure are briefly repeated in the following subsections with constant reference to the earlier subsections for detailed explanations.

5.3.1 Analysis and Practical Realisation of The Coupling Factor K Using Eigenmode Solver Method

The eigenmode solver method was used for the analysis and calculation of the coupling factor K between two adjacent ridge gap waveguide resonators and the physical separation distance s between them. The method and procedure is as discussed in subsection 5.2.2. The 3-D model diagram of two ridge gap waveguide resonators separated by distance s used in the calculation and analysis is shown in Fig. 5.32. The length of the resonators is 7.296 mm with other ridge gap waveguide resonator structure similar to those given in section 5.3. The two resonator arrangement was simulated using the CST eigenmode

solver for two modes for an initial arbitrary value of $s = 2$ mm. The results of the two simulated mode frequencies were post processed using CST post processing results template. The post processing calculation of value of K for a given value of s was based on (5.20). A parameter sweep of the distance s in the $[0 - 4]$ mm range was done for the plot of K values in that range. The resultant graph of the variation of the coupling factor K and the corresponding inter-resonator distance s in the range is shown in Fig. 5.33. For the same reason as stated in subsection 5.2.2, a best fit function was extracted and is also shown in Fig. 5.33.

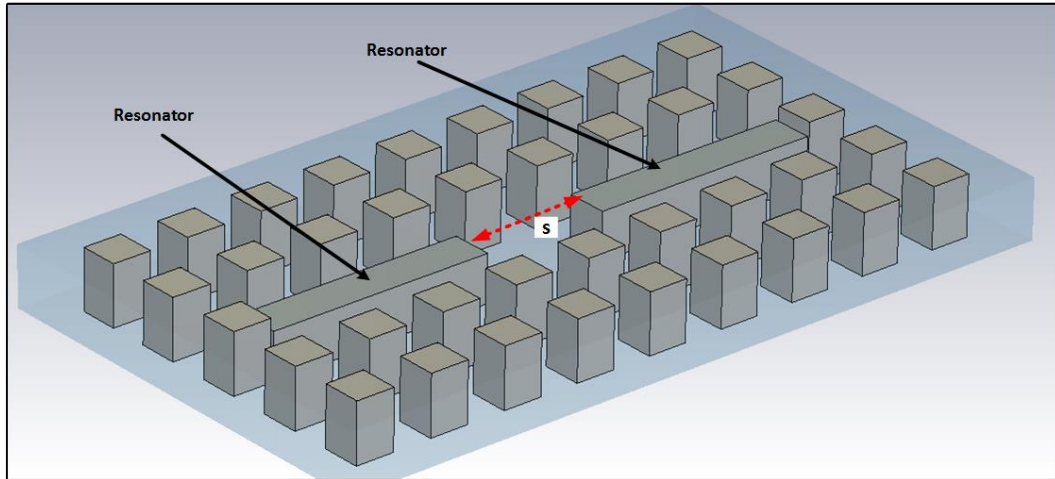


Figure 5.32: Ridge gap waveguide resonators for main-line coupling

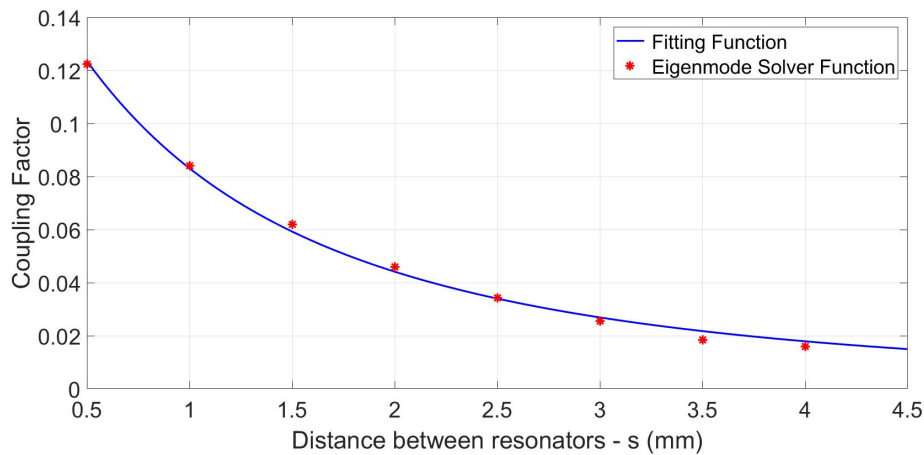


Figure 5.33: Eigenmode solver method for K and s

5.3.2 Analysis and Practical Realisation of The External Quality Factor Q_{ex} Using Group Delay Method

For the analysis of the external quality factor Q_{ex} of the first and last ridge gap waveguide resonators in relation to feed line and load line distance x , a ridge gap waveguide resonator and waveguide port feed line were used. The group delay method was used for the analysis and the calculation. Unlike in the earlier analysis of subsection 5.2.3, a waveguide port feed line was used instead of the SMA port, but the procedure is similar to that of subsection 5.2.3. The ridge gap waveguide resonator and the waveguide port feed line arrangement is shown in Fig. 5.34. The length of the resonator is 7.296 mm with other ridge gap waveguide resonator structure dimensions similar to those given in section 5.3. The initial arbitrary $x = 0.5$ mm value was set and the arrangement was simulated using CST for S_{11} . The simulation results of S_{11} were post processed using the CST post processing result template with filter analysis and group delay options. The processing was based on (5.20). The resultant graph of the external quality factor Q_{ex} after a parameter sweep of $x = [0 - 1]$ mm range is shown in Fig. 5.35. The best fit function was extracted for the same reason as stated in subsection 5.2.3 and is shown in Fig. 5.35 as well.

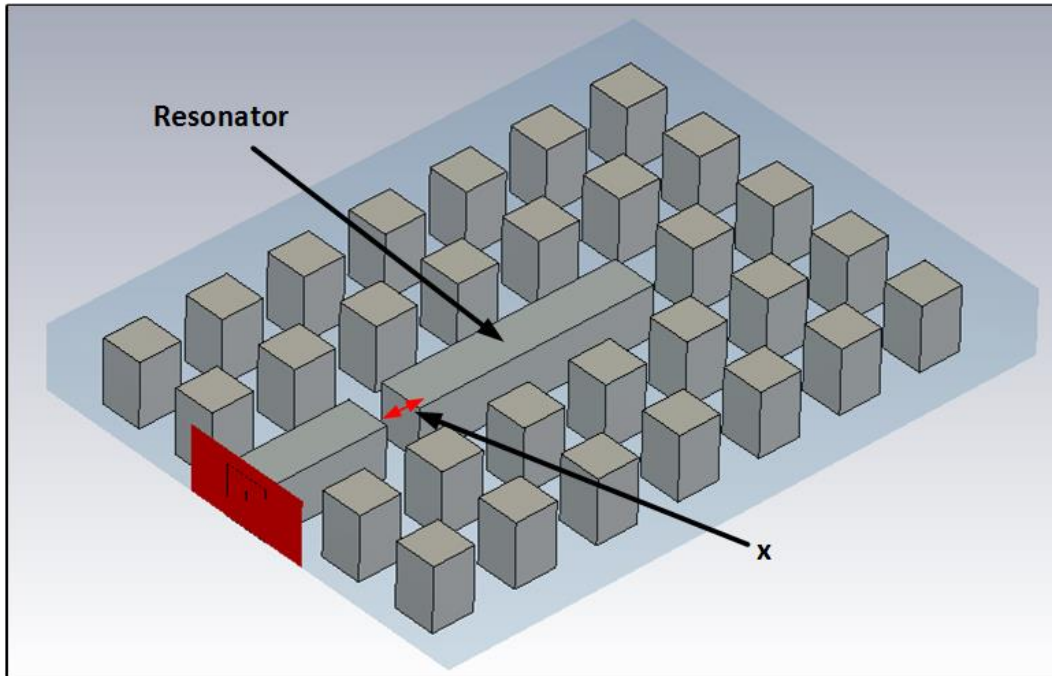


Figure 5.34: Group delay method for Q_{ex} and distance x

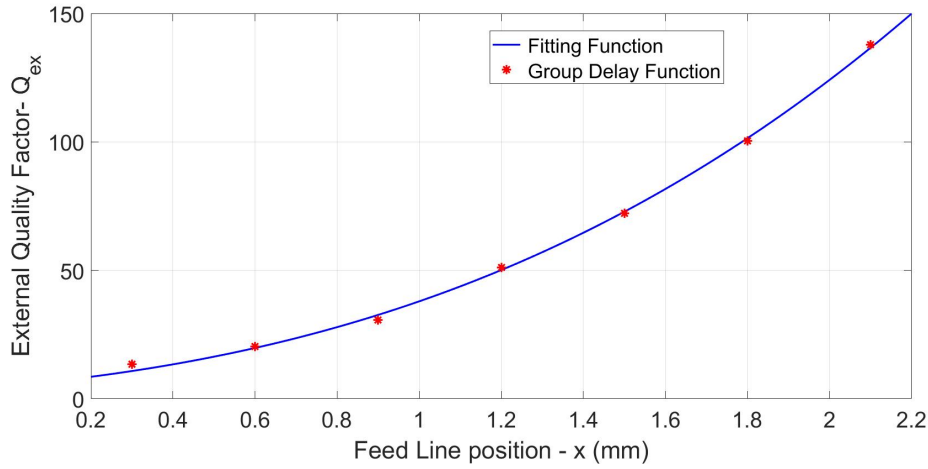


Figure 5.35: External quality factor Q_{ex} and distance x

The fitted functions of coupling factor K in Fig. 5.33 and that of external quality factor Q_{ex} in Fig. 5.35 were used in the design of a third order narrow band ridge gap waveguide bandpass filter. The filter was optimised using space mapping.

5.3.3 Design and Optimisation of The Third Order Narrow Band Microwave Ridge Gap Waveguide Bandpass Filter

A narrow band ridge gap waveguide coupled resonator bandpass filter was designed and optimised using space mapping. The filter design specifications were 0.04 dB passband transmission equal ripple response with a bandpass return loss of 20 dB, a fractional bandwidth of 1.5% and a centre frequency of 28 GHz.

The Chebyshev low pass prototype table for 0.04 dB equal transmission passband ripple prototype elements values was used. The element values are $g_o = g_4 = 1$, $g_1 = g_3 = 0.83768$ and $g_2 = 1.09767$. The main-line coupling value for $K_{12} = K_{23}$ was calculated using equation (5.14) and the external quality factor Q_{ex} was calculated using equation (5.15). The value of $K_{12} = K_{23} = 0.025$ and the value of $Q_{ex} = 35.55$. Using the graphs of Figs. 5.33 and 5.35, the initial values of s and x were approximated. The approximated values were used as initial design values for the fine model optimisation using space mapping. The other design parameters were the lengths of the of the middle resonator L_2 and the length of the outer pair resonators L_1 . There were four design parameters (L_1 , L_2 , s and x).

Just like in the other 2 previous examples, a $50\ \Omega$ half wavelength transmission line was used to coarse model the ridge gap waveguide resonators. The reasons for using the transmission model are as stated in subsection 5.2.2. For the filter centre frequency of 28 GHz, a transmission line of length 5.35 mm was calculated and used for the transmission line coarse model. We do not actually need to model the line impedance here, since this filter is used in a ridge waveguide environment, and by keeping the height and width the same we will have a constant cut-off frequency/wave impedance for the feeding lines as well as resonators. So our coarse model can use any impedance as long as it is the same for all the elements. The calculated values of K and Q_{ex} were scaled to the line impedance of $50\ \Omega$ in the coarse model. The coarse model schematic is shown in Fig. 5.36. The coarse model was simulated using MWO. The optimum S-parameter response of the coarse model is shown in Fig. 5.37.

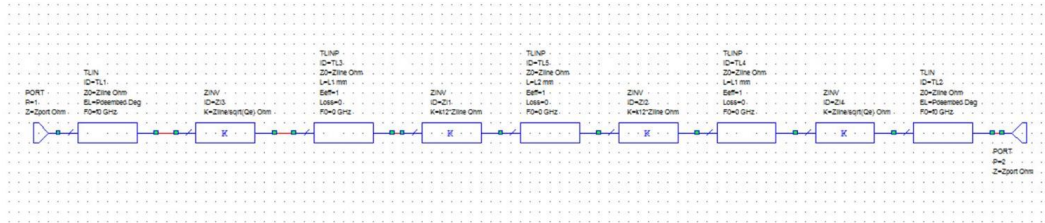


Figure 5.36: Coarse model schematic diagram

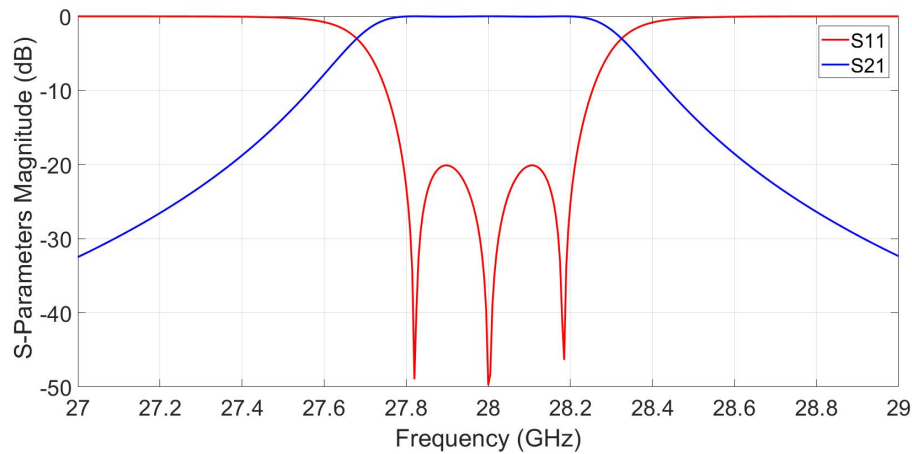
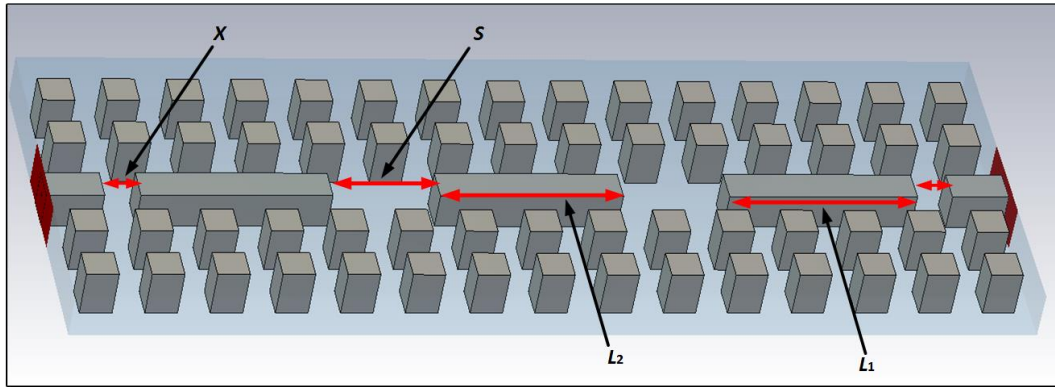


Figure 5.37: Coarse model S-parameters

| Design Variables | Initial value | Optimum value |
|------------------|---------------|---------------|
| L_1 | 7.296 | 7.4019 |
| L_2 | 7.296 | 7.1359 |
| s | 3.2356 | 4.1623 |
| x | 0.9316 | 1.3882 |

Table 5.4: Filter initial and optimum design parameter values

The fine model was implemented using three coupled ridge gap waveguide resonators each of length 7.296 mm. The length of the outer pair resonators L_1 and that of the middle resonator L_2 were chosen as design parameters all with initial values of 7.296 mm. The other design parameters were the inter-resonator distance s with an initial value estimated from Fig. 5.33 fitted function and the last design parameter was the feed line distance x whose initial value was estimated from fitted function of Fig. 5.35. There were four design parameters (L_1 , L_2 , s and x). The 3-D fine model and the design parameters are shown in Fig. 5.38. The fine model was simulated in CST.

**Figure 5.38:** Fine model and design parameters

An in-house space mapping code was used to optimise the four design parameters just like in the previous two examples. The initial evaluation of the fine model using initial design parameter values did not meet the design specifications as shown by the first iteration S-parameter response of Fig. 5.39. The same input space mapping steps mentioned and discussed in the previous examples also apply to this example. The filter was optimised after 11 iterations of evaluating the fine model. The last iteration response and the optimum fine model responses are shown in Figs. 5.40 and 5.41.

The results of the initial design parameter values and the optimum design parameter values are shown in Table 5.4. Just like in the previous filter

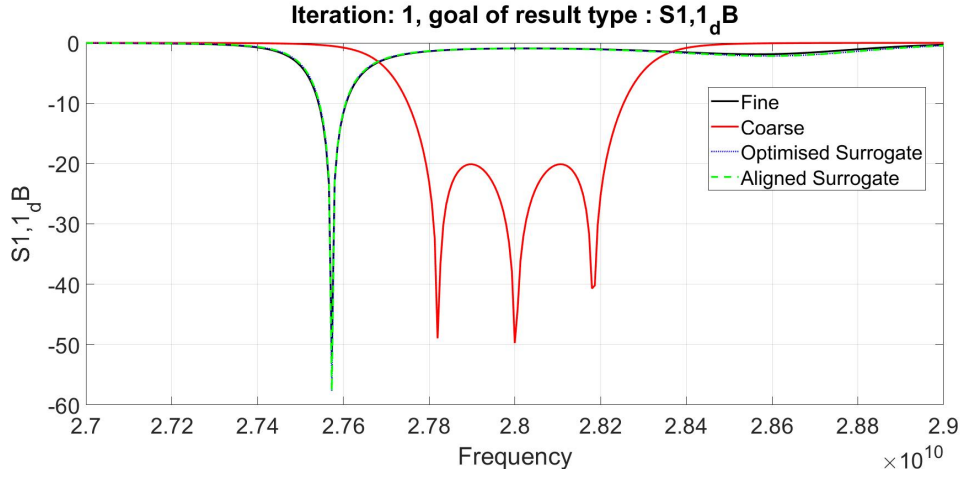


Figure 5.39: S-parameters for the first iteration

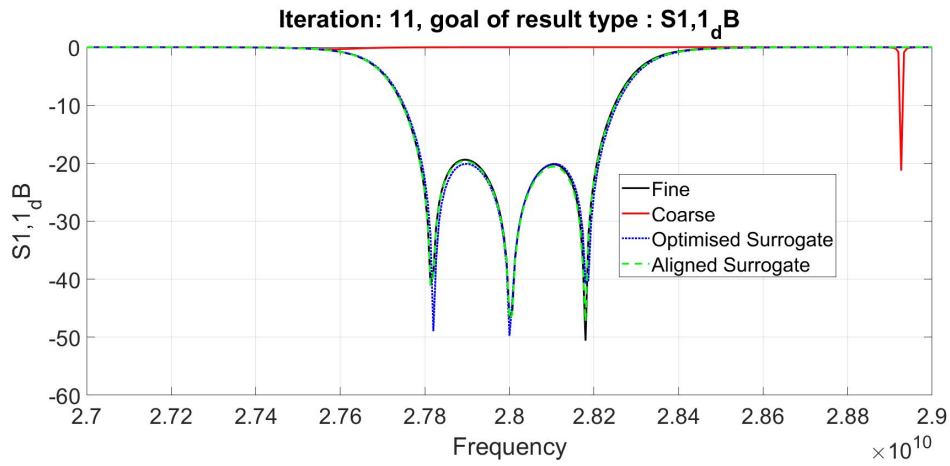


Figure 5.40: S-parameters for the last iteration

examples, there were changes in all the four design parameters and the results generally show that using the calculated design parameter values for filter design, in most cases won't give an optimum design. The design parameters need to be tuned or optimised to meet the design specifications.

For comparison the filter was directly optimised using the CST optimiser. The S-parameter filter response from direct optimisation of the filter is shown in Fig. 5.41. It took the CST optimiser 66 iterations of evaluating the fine model to optimise the filter whereas only 11 iterations were needed to optimise the filter using space mapping code.

All the three filter examples results generally show the simple but yet accurate use of a transmission line to model the narrow band gap waveguide

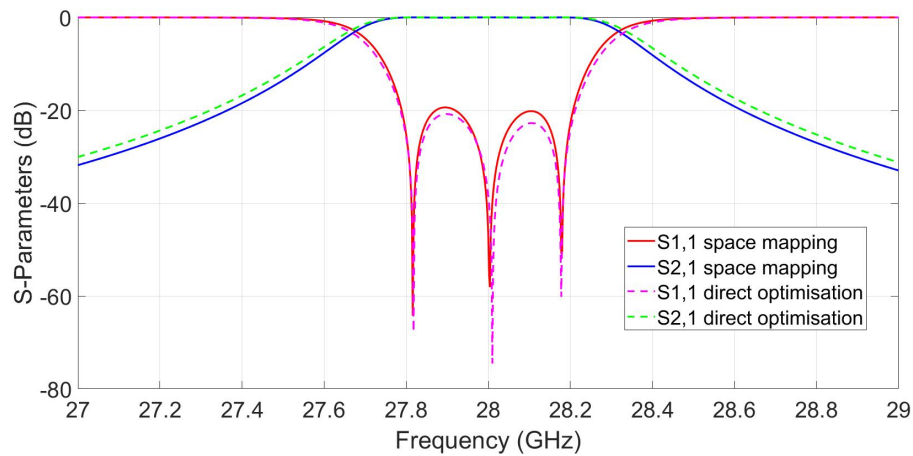


Figure 5.41: Space mapping and Direct optimisation fine model S-parameters

coupled resonator bandpass filters. The results of the filters also show that using the calculated design parameter values for filter design, in most cases won't give an optimum design. The filter design parameters need to be tuned or optimised to meet the design specifications and space mapping is the one of the optimisation techniques that can be used to optimise the gap waveguide filters. The results also show that space mapping is a relatively faster and efficient optimisation technique when compared to other direct optimisation methods.

Chapter 6

Conclusion

This thesis presented the design and optimisation of ridge and groove gap waveguide components using space mapping. The propagation, geometry and the structure of both ridge and groove gap waveguides were discussed as an introduction to gap waveguides. The noted interesting facts about gap waveguides was that they are completely open on the sides and this makes their fabrication simpler at microwave frequencies when compared to rectangular waveguides. Simulations were done to show how the pins stop propagation away the ridge and the groove in both waveguides through the plots of E-field diagrams. The relationship between the stopband and the gap waveguide dimensions was analysed through the plot of a dispersion diagram of a unit cell example.

The space mapping optimisation technique was defined. The coarse and fine models and their roles in space mapping were defined and analysed. Implicit and input space mapping methods were discussed. Input space mapping, which is the most basic and original version of space mapping, was manually applied in the optimisation of a basic bandstop filter which had one design parameter to demonstrate the concept. An in-house input space mapping code was used to optimise a 3-dB ridge gap waveguide power divider which had two design parameters. A 3-dB ridge gap waveguide hybrid coupler which had three design parameters was designed and manually optimised using input space mapping.

The use of a stripline to model the dispersive ridge gap waveguide components was discussed. The application of the readily known stripline characteristic impedance formula to approximate the otherwise difficult to calculate characteristic impedance of a ridge gap waveguide was discussed. This formula was used in the calculation of the widths of the 3-dB ridge gap waveguide power divider and coupler examples. The stripline was used to coarse model both examples and they were optimised through space mapping. Although the optimisation of both examples converged, the stripline model

was not very accurate.

The equivalence between the ridge/groove gap waveguides and ridge/rectangular waveguides in the stopband region was analysed and verified through plots of the dispersion diagrams. The ridged rectangular waveguide characteristic impedance formula was used to calculate vacuum gap height of the 3-dB ridge gap waveguide power divider example. The guided wavelength λ_g formula of the ridged rectangular waveguide was used to calculate the length of the ridge gap waveguide resonators in the design and optimisation of a third order narrow band microwave ridge gap waveguide coupled resonator bandpass filter. It was generally noted that because of their resemblance, the ridge/rectangular waveguide geometry can be used as starting geometry for ridge/groove gap waveguides components.

The Chebyshev bandpass filter was explained in terms of its transfer function and its response in the passband and stopband regions. A general discussion of narrow band coupled resonator bandpass filter and the impedance inverter K model of Chebyshev bandpass filter was done.

The S-parameter and eigenmode solver methods were used in the calculation and analysis of the coupling factor K and the inter-resonator distance s between two adjacent groove gap waveguide resonators and the resultant graph was plotted and estimated by a fitted function. The group delay method was used in the analysis and calculation of the external quality factor Q_{ex} of a groove gap waveguide resonator and its SMA feed point x and its graph was plotted and estimated by a fitted function. The eigenmode solver and group delay methods were also applied to the ridge gap waveguide filter example. The fitted functions were used in the design of the three filter examples. An in-house input space mapping code was used to optimise all the three filter examples.

A $50\ \Omega$ half wavelength transmission line was used to model the gap waveguide resonators in all the three filter examples. The transmission line was chosen because it is simple to analyse in a circuit model environment. The results of the transmission line model were good because of the very narrow bandwidth concerned, and the dispersion effects played a very small role. The differences in the wavelengths of the coarse and fine models were accounted for by applying a constant offset between the length of the transmission line and the length of the resonators to get the initial design value. The remaining small differences were handled by space mapping. There was no need to model the line impedance in the filter examples, since the filters were used in a gap waveguide environment, and by keeping the height and width the same we had a constant cut-off frequency/wave impedance for the feeding lines as well as resonators. So the coarse models could use any impedance as long as

it was the same for all the elements.

All three filter design examples results showed changes in the design parameters between the initial and optimum values. The results generally showed that using the calculated design parameter values in filter design, in most cases do not give an optimum design. The design parameters need to be tuned or optimised to meet the design specifications. Space mapping is one of the optimisation techniques and the whole idea of space mapping is to correct the errors between coarse and fine models for an optimum fine model design. The three filter examples were directly optimised using a built-in CST optimiser. The third order and fifth order groove gap waveguide filters did not converge from direct optimisation. The third order ridge gap waveguide filter did converge after 66 iterations compared to only 11 iterations of space mapping optimisation. The results generally showed that space mapping optimisation is a relatively faster and efficient optimisation technique when compared to other direct optimisation methods.

The transmission line model worked well for the gap waveguide bandpass filter examples because of the very narrow bandwidth involved. However as the bandwidth of the filters is increased, the accuracy of the transmission line model is more likely to diminish. For future work, there is still need to investigate the validity and accuracy of the transmission line model for larger bandwidths in the gap waveguide bandpass filters. There was no attempt to manufacture any of the components, since this was not part of the thesis scope. The only focus was on getting the best optimum 3-D CEM design done as quickly as possible. Also manufacturing of the components at these frequencies is still very challenging, but there are examples in literature of successful components.

List of References

- [1] C. Vicente and H. L. Hartnagel, "Passive-intermodulation analysis between rough rectangular waveguide flanges," *IEEE Transactions on Microwave Theory and Techniques*, vol. 53, no. 8, pp. 2515–2525, 2005.
- [2] P.-S. Kildal, "Three metamaterial-based gap waveguides between parallel metal plates for mm/submm waves," in *Antennas and Propagation, 2009. EuCAP 2009. 3rd European Conference on*, pp. 28–32, IEEE, 2009.
- [3] H. Raza and J. Yang, "Compact UWB power divider packaged by using gap-waveguide technology," in *Antennas and Propagation (EuCAP), 2012 6th European Conference on*, pp. 2938–2942, IEEE, 2012.
- [4] E. Alfonso, M. Baquero, A. Valero-Nogueira, J. Herranz, and P.-S. Kildal, "Power divider in ridge gap waveguide technology," in *Antennas and Propagation (EuCAP), 2010 Proceedings of the Fourth European Conference on*, pp. 1–4, IEEE, 2010.
- [5] A. U. Zaman, P.-S. Kildal, and A. A. Kishk, "Narrow-band microwave filter using high-q groove gap waveguide resonators with manufacturing flexibility and no sidewalls," *IEEE Transactions on Components, Packaging and Manufacturing Technology*, vol. 2, no. 11, pp. 1882–1889, 2012.
- [6] M. Rezaee, A. U. Zaman, and P.-S. Kildal, "V-band groove gap waveguide diplexer," in *Antennas and Propagation (EuCAP), 2015 9th European Conference on*, pp. 1–4, IEEE, 2015.
- [7] A. U. Zaman and P.-S. Kildal, "Wide-band slot antenna arrays with single-layer corporate-feed network in ridge gap waveguide technology," *IEEE Transactions on antennas and Propagation*, vol. 62, no. 6, pp. 2992–3001, 2014.
- [8] H. Kirino and K. Ogawa, "A 76 GHz multi-layered phased array antenna using a non-metal contact metamaterial waveguide," *IEEE Transactions on Antennas and Propagation*, vol. 60, no. 2, pp. 840–853, 2012.
- [9] E. Rajo-Iglesias, A. U. Zaman, and P.-S. Kildal, "Parallel plate cavity mode suppression in microstrip circuit packages using a lid of nails," *IEEE*

- Microwave and Wireless Components Letters*, vol. 20, no. 1, pp. 31–33, 2010.
- [10] A. U. Zaman, J. Yang, and P.-S. Kildal, “Using lid of pins for packaging of microstrip board for descrambling the ports of eleven antenna for radio telescope applications,” in *Antennas and Propagation Society International Symposium (APSURSI), 2010 IEEE*, pp. 1–4, IEEE, 2010.
 - [11] S. J. Leary, A. Bhaskar, and A. J. Keane, “A constraint mapping approach to the structural optimization of an expensive model using surrogates,” *Optimization and Engineering*, vol. 2, no. 4, pp. 385–398, 2001.
 - [12] M. Redhe and L. Nilsson, “Using space mapping and surrogate models to optimize vehicle crashworthiness design,” in *9th AIAA/ISSMO Symposium on Multidisciplinary Analysis and Optimization*, p. 5536, 2002.
 - [13] H.-S. Choi, D.-H. Kim, I.-H. Park, and S.-Y. Hahn, “A new design technique of magnetic systems using space mapping algorithm,” *IEEE Transactions on Magnetics*, vol. 37, no. 5, pp. 3627–3630, 2001.
 - [14] S. Koziel, Q. S. Cheng, and J. W. Bandler, “Space mapping,” *IEEE Microwave Magazine*, vol. 9, no. 6, 2008.
 - [15] J. W. Bandler, Q. S. Cheng, N. K. Nikolova, and M. A. Ismail, “Implicit space mapping optimization exploiting preassigned parameters,” *IEEE Transactions on Microwave Theory and Techniques*, vol. 52, no. 1, pp. 378–385, 2004.
 - [16] J. W. Bandler, Q. Cheng, D. H. Gebre-Mariam, K. Madsen, F. Pedersen, and J. Sondergaard, “EM-based surrogate modeling and design exploiting implicit, frequency and output space mappings,” in *Microwave Symposium Digest, 2003 IEEE MTT-S International*, vol. 2, pp. 1003–1006, IEEE, 2003.
 - [17] P.-S. Kildal, E. Alfonso, A. Valero-Nogueira, and E. Rajo-Iglesias, “Local metamaterial-based waveguides in gaps between parallel metal plates,” *IEEE Antennas and Wireless Propagation Letters*, vol. 8, pp. 84–87, 2009.
 - [18] P.-S. Kildal, A. U. Zaman, E. Rajo-Iglesias, E. Alfonso, and A. Valero-Nogueira, “Design and experimental verification of ridge gap waveguide in bed of nails for parallel-plate mode suppression,” *IET Microwaves, Antennas & Propagation*, vol. 5, no. 3, pp. 262–270, 2011.
 - [19] P.-S. Kildal, “Waveguides and transmission lines in gaps between parallel conducting surfaces,” Aug. 12 2014. US Patent 8,803,638.

- [20] A. U. Zaman, M. Alexanderson, T. Vukusic, and P.-S. Kildal, "Gap waveguide PMC packaging for improved isolation of circuit components in high-frequency microwave modules," *IEEE Transactions on Components, Packaging and Manufacturing Technology*, vol. 4, no. 1, pp. 16–25, 2014.
- [21] J. W. Bandler, R. M. Biernacki, S. H. Chen, P. A. Grobelny, and R. H. Hemmers, "Space mapping technique for electromagnetic optimization," *IEEE Transactions on Microwave Theory and Techniques*, vol. 42, no. 12, pp. 2536–2544, 1994.
- [22] J. W. Bandler, R. M. Biernacki, S. H. Chen, R. H. Hemmers, and K. Madsen, "Electromagnetic optimization exploiting aggressive space mapping," *IEEE Transactions on Microwave Theory and Techniques*, vol. 43, no. 12, pp. 2874–2882, 1995.
- [23] J. W. Bandler, "Optimization methods for computer-aided design," *IEEE Transactions on Microwave Theory and Techniques*, vol. 17, no. 8, pp. 533–552, 1969.
- [24] D. M. Pozar, "Microwave engineering," *Transmission Lines and Waveguides*, pp. 143–149, 2005.
- [25] H. Raza, J. Yang, P.-S. Kildal, and E. Alfonso, "Resemblance between gap waveguides and hollow waveguides," *IET Microwaves, Antennas & Propagation*, vol. 7, no. 15, pp. 1221–1227, 2013.
- [26] W. J. Hoefer and M. N. Burton, "Closed-form expressions for the parameters of finned and ridged waveguides," *IEEE Transactions on Microwave Theory and Techniques*, vol. 30, no. 12, pp. 2190–2194, 1982.
- [27] S. B. Cohn, "Direct-coupled-resonator filters," *Proceedings of the IRE*, vol. 45, no. 2, pp. 187–196, 1957.
- [28] M. Dishal, "Alignment and adjustment of synchronously tuned multiple-resonant-circuit filters," *Proceedings of the IRE*, vol. 39, no. 11, pp. 1448–1455, 1951.
- [29] R. J. Cameron, C. M. Kudsia, and R. R. Mansour, *Microwave filters for communication systems: fundamentals, design, and applications*. Wiley-Interscience, 2007.
- [30] P. communication with Ashraf Uz Zaman :28 GHz Ridge Gap Waveguide Filter.